Master's thesis

NTNU
Norwegian University of Science and Technology
Faculty of Information Technology and Electrical Engineering
Department of Engineering Cybernetics

Andreas Aurlien

Multivariate Modeling and Adaptive Control of Autonomous Ferries

Master's thesis in Cybernetics & Robotics
Supervisor: Bjørn-Olav H. Eriksen
Co-supervisor: Morten Breivik
June 2021

NTNU
Kunnskap for en bedre verden

Andreas Aurlien

Multivariate Modeling and Adaptive Control of Autonomous Ferries

Master's thesis in Cybernetics & Robotics
Supervisor: Bjørn-Olav H. Eriksen
Co-supervisor: Morten Breivik
June 2021

Norwegian University of Science and Technology
Faculty of Information Technology and Electrical Engineering
Department of Engineering Cybernetics

NTNU
Norwegian University of
Science and Technology

Abstract

Precise and energy-efficient motion control are important safety and economic aspects for marine vessels. This master's thesis presents the design and evaluation of a novel multivariate-based adaptive controller for marine surface vessels.

The goal is to create a system that detects and models changes in the vessel dynamics used in a dynamic positioning (DP) controller to improve the motion-control performance. A 3-degree of freedom (DOF) vessel model is generated by analyzing measured actuator force, velocity, and acceleration in a multivariate analysis (MVA). A lack-of-fit residual, defined by the difference between the modeled and observed vessel dynamics, is fitted to update the model with previously unmodeled dynamics.

This thesis covers the implementation of the adaptive controller in a full-scale vessel system and demonstrates the proof-of-concept through experimental tests. The full-scale experiments enlighten the robustness and reliability of the adaptive system. The experiments also prove the system's ability to generate good vessel models improving the performance, even when impacted by unmeasured disturbances from wind gusts of at least 6 m/s. The impact of unmeasured wave disturbances proves to be above the limit of what the adaptive system handles.

This new approach to model-based adaptive controllers can be the foundation of creating more reliable, safer, and precise control systems, approaching the goal of fully autonomous operational ferries for the benefit of better transportation systems. Further investigations towards these goals are suggested.

Sammendrag

Nøyaktig og energieffektiv bevegelsesstyring er viktig for sikker og økonomisk drift av marinefartøyer. Denne masteravhandlingen presenterer design og evaluering av en ny multivariat-basert adaptiv kontroller for marine overflatefartøy.

Målet er å lage et system som oppdager og modellerer endringer i fartøydynamikken som brukes i et dynamisk posisjoneringssystem, for å forbedre ytelsen til bevegelsesstyringen. En 3-DOF fartøymodell genereres ved å analysere målt aktuatorkraft, hastighet og akselerasjon i en multivariat analyse. Et mangel-på-passform residual, definert av differansen mellom den modellerte og observerte fartøy-dynamikken, er modellert for å oppdatere modellen med tidligere umodellert dynamikk.

Denne oppgaven dekker implementeringen av den adaptive kontrolleren i et fullskala fartøysystem og demonstrerer konseptbeviset gjennom eksperimentelle tester. Fullskala eksperimentene belyser robustheten og påliteligheten til det adaptive systemet. Eksperimentene viser også systemets evne til å generere gode fartøymodeller som forbedrer ytelsen, selv ved påvirkning av umålte forstyrrelser fra vindkast på minst $6\ m/s$. Virkningen av umålte bølgeforstyrrelser viser seg å være over grensen for hva det adaptive systemet håndterer.

Denne nye tilnærmingen til modellbaserte adaptive regulatorer kan gi grunnlag for å skape mer pålitelige, sikre og presise kontrollsystemer, og dermed ta oss nærmere målet om fullautonome operative ferger og bedre transportsystemer. Det foreslås ytterligere tiltak og undersøkelser for å kunne nå disse målene.

Preface

My five years of studying Cybernetics and Robotics has culminated in this master thesis. Through my studies, I have been prepared to do my own research, critical thinking, and conquer complex challenges. This project has been the most challenging and exciting work I have ever done. The work has made me grow as an academic, and I am grateful for everything I have learned during this process.

Without support from my supervisors, fellow students, family, and friends, I would never have been able to finish this thesis. I would like to thank Bjørn-Olav H. Eriksen and Morten Breivik for valuable discussions, ideas, guidance, proofreading, and follow-up meetings, helping me complete this thesis. Thanks to my flatmates for keeping up with me in stressful times and for all the fun moments during this past year. Finally, I would especially like to thank my wonderful girlfriend, Line. Your presence, support, and love make life so much more valuable and fun.

Andreas Aurlien
Trondheim, June 12, 2021

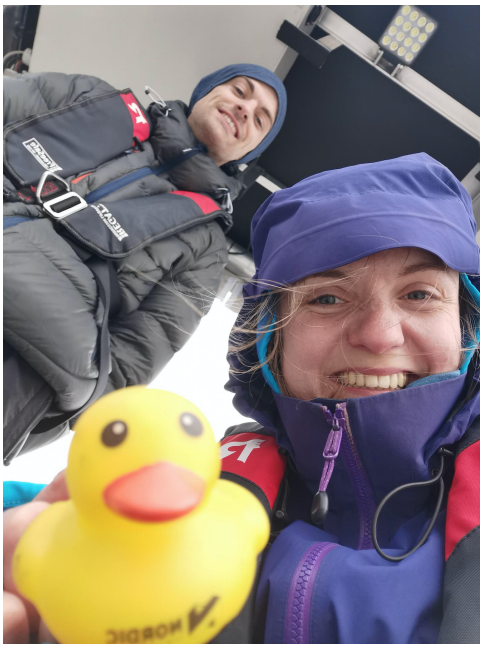

”The milliAmpere crew is having a debugging session.”
The photo is taken during one of the experiments in May.

Table of Contents

List of Figures

List of Tables

Acronyms

BDC	big data cybernetics.
CG	center of gravity.
CO	center of origin.
DOF	degree of freedom.
DP	dynamic positioning.
EC	energy consumption.
ESKF	error state Kalman filter.
FB	feedback.
FF	feed-forward.
GNSS	global navigation satellite system.
HAM	hybrid analysis and modeling.
IAE	integral of the absolute error.
IAEW	integral of the absolute error multiplied by the energy consumption.
ILSVRC	ImageNet Large Scale Visual Recognition Competition.
IMU	inertial measurement unit.
ISE	integral of the square of the error.
KF	Kalman filter.
LHS	left-hand side.
LOS	line-of-sight.

MPC	model predictive control.
MSE	mean squared error.
MVA	multivariate analysis.
NED	north-east-down.
NIPALS	nonlinear iterative partial least squares.
NSCA	nonlinear scalar control allocation.
OBC	on board computer.
PCA	principal component analysis.
PE	persistent excitation.
PID	proportional-integral-derivative.
PLS	partial least squares.
RHS	right-hand side.
ROS	robot operating system.
RPM	rounds per minute.
RTHS	real-time hybrid simulation.
RTK	real-time kinetic.
SIMPLS	simple partial least squares.
SNAME	Society of Naval Architects and Marine Engineers.
WGN	white Gaussian noise.

Chapter 1

Introduction

In this chapter, the possibilities and the importance of autonomy in various industries are presented, with main focus on the marine industry. Following, the problem description, related work, and contributions are presented. The contributions relate to experimental tests of new methods improving the performance of motion control for surface vessels. Finally the outline for the thesis is presented.

1.1 Motivation

The race to achieve fully autonomous systems is on. During the past few years the car industry has step by step approached the goal of fully autonomous cars. Back in 2015, Waymo operated a fully autonomous car in an open environment, but was limited to operate only in a small area with low speeds (Fairfield, 2016). A commercialized consumer product that works in larger areas is yet to be seen.

Automation of transportation systems is not new. Subway systems such as the Paris, Lausanne, and Copenhagen metro, function without human control and have been automated for many years, but are not considered fully autonomous. According to NATO's definitions, autonomous systems relates to "A unmanned systems own ability of integrated sensing, perceiving, analysing, communicating, planning, decision making, and acting [...]", which makes the safety and control aspects of fully autonomous systems much more advanced and rely on completely different safety standards compared to automated systems (Williams, 2015). Automation, on the other hand, refers to a system that operates in a closed environment that do not interact with humans.

Elon Musk claims that Tesla will reach Level 5 Autonomy for their self driving cars, the highest classification of autonomy, by the end of 2021 (International, 2021; Hyatt, 2021). The CEO of Waymo, head of Teslas biggest competitor on autonomous cars, claims on the other hand that Tesla never will reach this level of autonomy with their current

Figure 1.1: Yara Birkeland undergoing sea-trials, by courtesy of Yara (2020).

approach (Wilkes, 2021). Tesla's approach is to only use cameras as sensors and deep-neural networks to train their system, while Waymo's approach focuses on creating a full 3D model of entire cities, where lidars are used to map the surrounding objects and where cameras read the signs. Waymo does not use machine learning for the maneuvers and mapping of the surrounding but rather use it to predict the traffic and pedestrian movements to smoothly execute the planed route. Tesla uses cameras and machine learning for both the mapping and motion planning, similar to a human's approach to driving. This solution generalizes the problem and works anywhere. There is no doubt that investors see the potential for autonomous systems. In fact, between August 2014 and June 2017, 80 billion US dollars were invested into the automation of the car industry (Zanona, 2017).

The shipping industry is also getting closer to reach fully autonomous vessels. Kongsberg Maritime's and Yara's autonomous ship MS Yara Birkeland shown in Figure 1.1, will be the first autonomous ship of its kind and is foreshadowed to be fully autonomous operational in 2022. The ship has been launched and now undergoes preparations for autonomous operation in a test area in Horten (Yara, 2020). In operation, the ship removes 40 000 truckloads from the roads yearly between Yara's fertilizer factory and the shipping harbors (Stensvold, 2017; Yara, 2018). Kongsberg Maritime and Massterly also signed contracts with ASKO, the leading Norwegian grocery distributor, delivering two new zero-emission autonomous ships in 2022. The ships will be used across the Oslo fjord and will replace 2 million kilometers of truck transport, saving 5 000 tonnes of CO2 annually. Initially, the ships will operate with a reduced crew for a two-year test period. Approval for fully unmanned operations is expected during 2024 (Kongsberg, 2020).

The massive development in computer power and machine learning algorithms has made it possible to develop such advanced systems for autonomous cars and ships. Until recently, the processing of a large amount of data has been a slow process (Divino, 2020). Through contests like ImageNet Large Scale Visual Recognition Competition (ILSVRC), massive development in deep learning algorithms (Russakovsky et al., 2015) have been seen, and Tesla's approach to self-driving cars shows how the technology and industry closely follow

Figure 1.2: Concept illustration of Zeabuz, by courtesy of Zeabuz (2021).

each other.

By 2050 nearly 70% of the world's population will live in cities, 50% more than today (Zeabuz, 2021). Cities are often founded near waterways that also separate districts like seen in New York City. Building bridges and tunnels are costly, non-scalable, and also leaves a large and lasting footprint. The growing infrastructure requirement in the cities sparked the idea to further utilize the seaways for better transportation systems (Cairns, 2020; Knutsen, 2020). This often unused space can be used by environmentally friendly passenger ferries that efficiently transport people across the city. NYC Ferry recently expanded their services with several routes and stops, but unfortunately, they are still not autonomous or electric (Lee, 2019). Norwegian University of Science and Technology (NTNU)'s Autoferry project, with close cooperation with the spin-off company Zeabuz, wants to make this option available. Autonomous vessels will be safer, more energy-efficient, cheaper, and can operate at any time of the day that all would benefit the passengers.

Zeabuz springs of decades of research on hydrolift smart city ferries at NTNU. As a part of the ongoing research, NTNU has financed and built two research vessels, milliAmpere and milliAmpere 2. Based on the experience from the milliAmpere vessels, Zeabuz plans to design and launch their first pilot ferry in 2022 (Zeabuz, 2021).

The Autoferry project is an initiative to make a fully autonomous electric ferry that can cross the channel in the city center of Trondheim between Ravnkloa and Vestre kanalhavn, as seen in Figure 1.3. The two prototypes milliAmpere and milliAmpere 2, are used to develop and test the systems created.

Marine vessels are dependent on precise and efficient motion control for operation purposes. Model-based control is a good approach to accomplish this. A perfect model is, however, impossible to obtain as it will always be based on assumptions and approximations that simplify the real behavior of a system. In most cases, a simplified model is sufficient for control purposes. However, imperfect models in a control system might lead to a waste of energy and imprecise maneuvers due to imprecise control actions. Many systems overlook the value of sensor data that can be used to improve the performance of a system. The milliAmpere ferry collects loads of data from different sensors located on the vessel giving information about the vessel's states and the surrounding environment.

(a) The milliAmpere ferry at the christening, by courtesy of the IE faculty at NTNU.

(b) From the first sea-trials for milliAmpere 2, by courtesy of the IE faculty at NTNU.

(c) Operational route for milliAmpere, by courtesy of Egil Eide.

Figure 1.3: The Autoferry project.

Analyzing the data makes us able to better understand how the vessel behaves and moves in relation to the environment. Jervan (2020) started the design of an adaptive controller for milliAmpere based on big data cybernetics (BDC) to take advantage of all the collected data. Aurlien (2020) expanded the system to also model wind forces. The motivation for this master's thesis is to finalize the adaptive controller and test the system in full scale on the milliAmpere vessel.

BDC is a new and upcoming field in cybernetics (Martens, 2020). With this new approach, the best from control theory, physics-based models, deep neural networks, and big data are combined. The first professorship in BDC was established back in 2015 by NTNU

and Kongsberg. BDC is a unique theoretical approach to Big Data management and is important to utilize the vast amount of data that is measured and stored everywhere around us (Kongsberg Group, 2015). Big data is more valuable than ever and will be important in the development and improvement of current and future systems. NTNU and Kongsberg therefore aim to contribute to world-leading research in the field.

In the context of control theory, BDC is essentially an improvement of the famous feedback loop. MVA is the concept of finding structures in data sets, and through hybrid analysis and modeling (HAM), the models used by control systems can be improved for better performance. HAM describes how to generate a model error based on observed and measured data using all available data to model this model error. Deep learning is not very intuitive but could be a solution. The advantage with HAM is that big data is used to fit existing physics based models that can explain much of the model deviations, making the models intuitive and trustworthy. HAM used for control purposes is BDC in a nutshell (Rasheed et al., 2019). In this thesis, the BDC approach is used to make an adaptive controller detecting model changes or inaccuracies in real-time. This thesis furthermore describes how to improve the motion control performance by identifying and modeling unmodeled dynamics.

1.2 Problem Description

The problem description for this masters thesis is summarized by:

- Continue the work of Aurlien (2020) and perform full-scale experiments of the adaptive control system in closed-loop.
- Extend the adaptive model to support current modeling.
- Solve practical issues related to the transition from simulations to experiments and make the system robust.
  - Find a practical solution to how the lack-of-fit-residual is obtained.
  - Find a precise way to estimate acceleration.
  - Find a good enough set of basis functions to detect changes in the model dynamics.
  - Develop a tuning process for the adaptive system parameters.
- Write an article summarizing the discoveries of the master's thesis.
- Illuminate possibilities, advantages, and limitations of adaptive control systems.
- Perform experimental tests of the carrot-based control system developed by Aurlien (2020).

1.3 Related Work

The Autoferry project is all about developing a fully autonomous ferry suitable for urban areas. Such a complicated project needs many diverse systems to meet safety and reliability conditions. The Autoferry project is built around the six PhD positions on

- Automation and autonomy
- Multi-sensor tracking via shore- and ferry-based sensors
- All-electric power and propulsion
- Human factors, remote monitoring, and control
- Communications and cybersecurity
- Risk management

that combined reflect the goals in the Assuring Trustworthy, Safe and Sustainable Transport for All (TRUSST) project lead by DNVGL (2021). This boils down to three main parts consisting of: 1. collision avoidance systems and monitoring, 2. path planning, docking, and control, and 3. security and risk management.

Master students have contributed to the Autoferry project since the beginning of the project in 2017. Some of the earlier masters thesis has been ”Estimating model parameters” by Pedersen (2019), leading up to the model used on milliAmpere today, ”Efficient docking minimizing energy usage” by Molven (2020), that ensures efficient docking path planning and execution, ”Collision avoidance system” by Thyri (2019), that can use information from radars, cameras, and lidar to map and respond to the environment, and ”Adaptive control system” by Jervan (2020) that started the work to update the vessel model for more precise control actions.

The work of Gale et al. (2017) of improving the model for a robotic manipulator based on multivariate residual modeling has been an important inspiration for the methods suggested in this thesis.

Regarding other approaches to FF controllers, Boerlage et al. (2003) proposes a model-based FF controller for a 2-dof system, that consist of an acceleration FF part and and an inverse dynamics model for flexible modes. The idea is to compensate for higher mode dynamic effects making on-line tuning feasible. Depending on the mode, predefined adjustments in form of skew notch filters are applied to the dynamics, making the inverse dynamics of the plant are accurate. This technique is similar to how the first autopilots for airplanes used to be when dealing with un-linear lift models for different angle-of-attacks (Ioannou and Sun, 2012). This was solved by implementing a parameter scheduler that switched parameters for different ranges of angle-of-attacks.

Another FF design by Lambrechts et al. (2004) uses a 4-order trajectory planning with both velocity, acceleration, jerk, and the derivative of the jerk (snap) in the FF controller for single-axis motion. Trajectory planners for second and third-order models are fairly known in academia, with this thesis suing a second-order trajectory planner for the 3-DOF

system. Higher-order planners are highly complex, but time-optimality actuator effort limitation, reliability, and accuracy can be improved.

Model-based feedforward–feedback tracking control is one of the most efficient methods for real-time hybrid simulation (RTHS). RTHS is a testing technique applied to a structure that consists of physical and numerical components that are coupled in time. The technique can be used to test the strength of a building or a bridge when impacted by earthquakes. Chen et al. (2015) presents an adaptive model-based feedforward–feedback tracking control to apply this technique to structures. The method is tested on a building and compared to actual data from two earthquakes.

1.4 Contributions

In this thesis an adaptive control system for autonomous ferries is suggested, tested, and evaluated. The adaptive controller is tested through realistic simulations and is verified by full-scale experiments on milliAmpere. The suggested adaptive controller adds wind and current modeling support, but this added functionality is not tested in experiments due to the lack of wind and current measurement on milliAmpere. The thesis further presents and experimentally tests the customized carrot-based guidance system by Aurlien (2020), used for better path following. The contributions are summarized as the following:

1. *Finalized an adaptive control system for surface vessels adding wind and current modeling support.*
2. *A method for automated model verification is presented.*
3. *A modified line-of-sight (LOS) guidance law is suggested for the milliAmpère surface vessel.*
4. *Experimental tests proving the robustness and limitations of the system when considering real environment forces and sensor disturbances.*
5. *Wrote and submitted an article for the* 13^{th} *International Federation of Automatic Control (IFAC) Conference on Control Applications in Marine Systems, Robotics, and Vehicles (CAMS) The article is included as Appendix D.*

1.5 Outline

Chapter 2 presents the basic theory of multivariate modeling and motion control of autonomous ferries. Chapter 3 presents improvements to the motion control system regarding path following, modeling, and control actions. Chapter 4 presents the system description and setup, including the specifics for the milliAmpere vessel used for the experiments. Chapter 5 presents and evaluates the simulations and experimental results. Chapter 6 presents the conclusion and further work.

Chapter 2

Background Theory

This chapter presents the basic theory of multivariate modeling and control of autonomous ferries. The content in this chapter is mostly based on Aurlien (2020).

2.1 Mathematical Modeling

This section will describe the mathematical system needed to understand vessel dynamics and interactions with the surrounding environment.

2.1.1 Surface Vessel Model

The marine vessel notation used in this thesis follows the Society of Naval Architects and Marine Engineers (SNAME) notation shown in Table 2.1. For surface vessels, heave, pitch, and roll can be assumed small; hence, the model can be simplified from 6-DOF to 3-DOF. The rigid-body dynamics for a 3-DOF surface vessel can be expressed in a vectorial setting with generalized position vector $\boldsymbol{\eta} = [x, y, \psi]^\top$ and velocity vector $\boldsymbol{\nu} = [u, v, r]^\top$. The pose vector $\boldsymbol{\eta}$ is described in the Earth-fixed NED reference frame and the velocity vector is described in the body reference frame. An illustration of the degrees of freedom is shown in Figure 2.1.

Fossen (2011) describes the kinematics for surface vessels according to

$$\dot{\boldsymbol{\eta}} = \boldsymbol{R}(\psi)\boldsymbol{\nu}, \tag{2.1}$$

$$\boldsymbol{R}(\psi) = \begin{bmatrix} \cos\psi & -\sin\psi & 0 \\ \sin\psi & \cos\psi & 0 \\ 0 & 0 & 1 \end{bmatrix}, \tag{2.2}$$

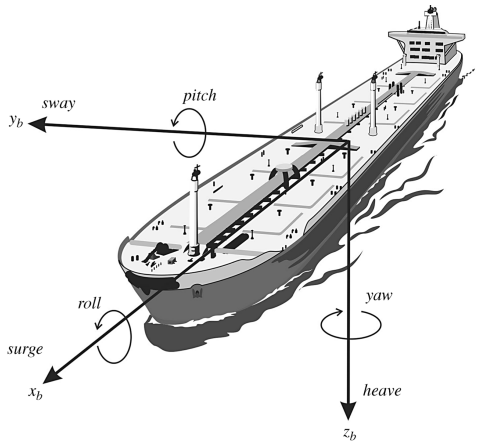

Figure 2.1: Body fixed motion in 6-DOF, by courtesy of (Fossen, 2011).

where $\boldsymbol{R}(\psi)$ is the rotation matrix from the Body to the NED reference frame. The kinetics are described according to

$$\boldsymbol{\tau}_{rb} = \boldsymbol{M}_{rb}\dot{\boldsymbol{\nu}} + \boldsymbol{C}_{rb}\boldsymbol{\nu}, \tag{2.3}$$

where $\boldsymbol{M}_{rb}$ is the inertia matrix, $\boldsymbol{C}_{rb}$ is the Coriolis and centripetal matrix and $\boldsymbol{\tau}_{rb}$ is the rigid body force. Equation (2.3) is Newton's second law of motion on vectorial form.

When a vessel moves through the water it also moves water surrounding the vessel. This volume of water is known as the hydrodynamic added mass and affects the dynamics of the vessel. The considered forces acting on the rigid body forces are

$$\boldsymbol{\tau}_{rb} = \boldsymbol{\tau}_{hyd} + \boldsymbol{\tau} + \boldsymbol{\tau}_{dist} \tag{2.4a}$$

$$\boldsymbol{\tau}_{hyd} = -\boldsymbol{M}_a\dot{\boldsymbol{\nu}} - \boldsymbol{C}_a(\boldsymbol{\nu})\boldsymbol{\nu} - \boldsymbol{D}(\boldsymbol{\nu})\boldsymbol{\nu}, \tag{2.4b}$$

where $\boldsymbol{\tau}_{hyd}$ is the hydrodynamic forces, $\boldsymbol{\tau}$ is the actuator forces, $\boldsymbol{\tau}_{dist}$ is disturbances, $\boldsymbol{M}_a$ is the hydrodynamic added mass matrix, $\boldsymbol{C}_a$ is the added Coriolis and centripetal force, and $\boldsymbol{D}$ is the damping matrix. The added mass and added Coriolis and centripetal are effects resulting from water surrounding the vessel being moved, making the effective mass greater than the rigid body mass. The wind and current impact $\boldsymbol{\tau}_w, \boldsymbol{\tau}_c \in \boldsymbol{\tau}_{dist}$ are for now, considered as unmodeled disturbance components that are components of the rigid body forces. Defining

$$\boldsymbol{M} \coloneqq \boldsymbol{M}_{rb} + \boldsymbol{M}_a \tag{2.5a}$$

$$\boldsymbol{C}(\boldsymbol{\nu}) \coloneqq \boldsymbol{C}_{rb}(\boldsymbol{\nu}) + \boldsymbol{C}_a(\boldsymbol{\nu}), \tag{2.5b}$$

combines the rigid body and hydrodynamic dynamics. The 3-DOFs model for the rigid body kinetics is obtained by combining (2.3), (2.4), and (2.5):

$$\boldsymbol{\tau}_{rb} = \boldsymbol{M}\dot{\boldsymbol{\nu}} + \boldsymbol{C}(\boldsymbol{\nu})\boldsymbol{\nu} + \boldsymbol{D}(\boldsymbol{\nu}), \tag{2.6}$$

where $\boldsymbol{M}$ is the inertia matrix and $\boldsymbol{C}$ is the Coriolis and centripetal matrix.

Table 2.1: The notation for marine vessels defined by the Society of Naval Architects and Marine Engineers.

DOF		Forces and moments	Linear and angular moments	Position and Euler angles
1	Motion in the x direction (surge)	X	u	x
2	Motion in the y direction (sway)	Y	v	y
3	Motion in the z direction (heve)	Z	w	z
4	Rotation in the x direction (roll)	K	p	ϕ
5	Rotation in the y direction (pitch)	M	q	θ
6	Rotation in the z direction (yaw)	N	r	ψ

It is common to assume that the vessel has homogeneous mass distribution and xz plane symmetry so that $I_{xy} = I_yz = 0$ (Fossen, 2011). The body frame is set in the center-line and at the point center of origin (CO) so that $y_g = 0$. Furthermore, it is assumed that the added mass is computed in CO. The effective mass is considered as the sum of the rigid body mass and the hydrodynamic added mass. With all these assumptions, the inertia matrix is constant, positive definite where

$$\boldsymbol{M}_{rb} = \begin{bmatrix} m & 0 & 0 \\ 0 & m & mx_g \\ 0 & mx_g & I_z \end{bmatrix}, \boldsymbol{M}_a = \begin{bmatrix} -X_{\dot{u}} & 0 & 0 \\ 0 & -Y_{\dot{v}} & -Y_{\dot{r}} \\ 0 & -N_{\dot{v}} & -N_{\dot{r}} \end{bmatrix}, \tag{2.7}$$

and m is the mass of the vessel, (x_g, y_g) is the center of gravity (CG) of the vessel, I_z is the moment of inertia for the rigid body in yaw, while the rest of the parameters are scalar terms related to the added hydrodynamic mass.

The Coriolis and centripetal matrix can be described in terms of the inertia matrix so that it always is skew-symmetric

$$\boldsymbol{C}(\boldsymbol{\nu}) = \boldsymbol{C}(\boldsymbol{\nu})^\top \tag{2.8}$$

where

$$\boldsymbol{C}_{rb}(\boldsymbol{\nu}) = \begin{bmatrix} 0 & 0 & -m(x_g r + v) \\ 0 & 0 & mu \\ m(x_g r + v) & -mu & 0 \end{bmatrix}, \tag{2.9}$$

$$\boldsymbol{C}_a(\boldsymbol{\nu}) = \begin{bmatrix} 0 & 0 & c_{13}(\boldsymbol{\nu}) \\ 0 & 0 & c_{23}(\boldsymbol{\nu}) \\ c_{31}(\boldsymbol{\nu}) & c_{32}(\boldsymbol{\nu}) & 0 \end{bmatrix}, \tag{2.10}$$

with

$$c_{13}(\boldsymbol{\nu}) = Y_{\dot{v}} + \frac{1}{2}(N_{\dot{v}} + Y_{\dot{r}})r \tag{2.11a}$$
$$c_{23}(\boldsymbol{\nu}) = -X_{\dot{u}}u \tag{2.11b}$$
$$c_{31}(\boldsymbol{\nu}) = -c_{13}(\boldsymbol{\nu}) \tag{2.11c}$$
$$c_{32}(\boldsymbol{\nu}) = -c_{23}(\boldsymbol{\nu}). \tag{2.11d}$$

The hydrodynamic dampening matrix $\boldsymbol{D}(\boldsymbol{\nu})$ can be described as the sum of linear viscous dampening $\boldsymbol{D}_L$ and nonlinear dampening $\boldsymbol{D}(\boldsymbol{\nu})_{NL}$

$$\boldsymbol{D}(\boldsymbol{\nu}) = \boldsymbol{D}_L + \boldsymbol{D}_{NL}(\boldsymbol{\nu}), \tag{2.12}$$

where the nonlinear dampening describes the cross-flow drag Fossen (2011). The hydrodynamic dampening matrix is positive definite and defined by

$$\boldsymbol{D}_L = \begin{bmatrix} -X_u & 0 & 0 \\ 0 & -Y_v & -Y_r \\ 0 & -N_v & -N_r \end{bmatrix}, \boldsymbol{D}_{NL}(\boldsymbol{\nu}) = \begin{bmatrix} d_{11}(\boldsymbol{\nu}) & 0 & 0 \\ 0 & d_{22}(\boldsymbol{\nu}) & d_{23}(\boldsymbol{\nu}) \\ 0 & d_{32}(\boldsymbol{\nu}) & d_{33}(\boldsymbol{\nu}) \end{bmatrix}. \tag{2.13}$$

The model described by Blanke (1981) uses second order modulus functions to fit the cross-flow drag dynamics where the elements in $\boldsymbol{D}(\boldsymbol{\nu})$ are modeled as

$$d_{11}(\boldsymbol{\nu}) = -X_{|u|u}|u| - X_{uuu}u^2 \tag{2.14a}$$
$$d_{22}(\boldsymbol{\nu}) = -Y_{|v|v}|v| - Y_{|r|v}|r \tag{2.14b}$$
$$d_{23}(\boldsymbol{\nu}) = -Y_{|v|r}|v| - Y_{|r|r}|r| \tag{2.14c}$$
$$d_{32}(\boldsymbol{\nu}) = -N_{|v|v}|v| - N_{|r|v}|r| \tag{2.14d}$$
$$d_{33}(\boldsymbol{\nu}) = -N_{|v|r}|v| - N_{|r|r}|r|, \tag{2.14e}$$

and where the parameters are scalars. The linear part $\boldsymbol{D}_L$ can be neglected for high speed maneuvering models since the higher order terms will dominate, but for station-keeping and low speed maneuvering it is recommended to keep the linear terms. The third order modulus term $X_{uuu}u^2$ can be added, to increase the complexity slightly. This term can be added without any other further modifications because surge is assumed decoupled from sway and yaw. Pedersen (2019) chooses to add $Y_{vvv}v^2$ and $N_{rrr}r^2$ as well to d_{22}, and d_{33} respectively to obtain a more complicated model, but this is considered slightly inaccurate since then other terms should also be added to complete the third order modulus function with coupling in sway and yaw.

2.1.2 Wind Load Model

The movement of a rigid body system will be affected by wind. According to Blendermann (1994), the wind will apply a force to a 3-DOF ship model in the following manner:

$$\boldsymbol{\tau}_w = \frac{1}{2}\rho_a V_{rw}^2 \begin{bmatrix} C_{X_w}(\gamma_{rw})A_{F_w} \\ C_{Y_w}(\gamma_{rw})A_{L_w} \\ C_{N_w}(\gamma_{rw})A_{L_w}L_{0a} \end{bmatrix}, \tag{2.15}$$

where ρ_a is the air density, V_{rw} is the relative air speed, γ_{rw} is the angle of attack of V_{rw} relative to the bow of the ship, $C_X(\gamma_{rw}), C_Y(\gamma_{rw})$ and $C_N(\gamma_{rw})$ are the wind coefficients for horizontal plane motion, L_{0a} is the distance from the bow to the stern, and A_{F_w} and A_{L_w} is the frontal and lateral projected areas, respectively. The relative air speed and the angle of attack are further defined as

$$V_{rw} = \sqrt{u_{rw}^2 + v_{rw}^2}, \tag{2.16}$$

where u_{rw} and v_{rw} are the speed of the rigid body relative to the wind in the longitudinal and lateral direction, respectively, described in the body reference frame and where

$$\gamma_{rw} = -\text{atan2}(v_{rw}, u_{rw}). \tag{2.17}$$

The wind coefficients are defined as

$$C_{X_w}(\gamma_{rw}) = -CD_{lAF}\frac{\cos(\gamma_{rw})}{1 - \frac{\delta}{2}\left(1 - \frac{CD_l}{CD_t}\right)\sin^2(2\gamma_{rw})} \tag{2.18a}$$

$$C_{Y_w}(\gamma_{rw}) = CD_t\frac{\sin(\gamma_{rw})}{\left(1 - \frac{\delta}{2}\left(1 - \frac{CD_l}{CD_t}\right)\sin^2(2\gamma_{rw})\right)} \tag{2.18b}$$

$$C_{N_w}(\gamma_{rw}) = \left[\frac{S_L}{L_{0a}} - 0.18\left(\gamma_{rw} - \frac{\pi}{2}\right)\right]C_{Y_w}(\gamma_{rw}). \tag{2.18c}$$

2.1.3 Current Load Model

Similarly to the wind load model, the current load model can, according to Blendermann (1994), be described as

$$\boldsymbol{\tau}_c = \frac{1}{2}\rho V_{rc}^2 \begin{bmatrix} C_{X_c}(\gamma_{rc})A_{F_c} \\ C_{Y_c}(\gamma_{rc})A_{L_c} \\ C_{N_c}(\gamma_{rc})A_{L_c}L_{0a} \end{bmatrix}, \tag{2.19}$$

where

$$C_{X_c}(\gamma_{rc}) = -2\left(\frac{-X_{|u|u}}{\rho A_{F_c}}\right)\cos(\gamma_{rc})|\cos(\gamma_{rc})| \tag{2.20a}$$

$$C_{Y_c}(\gamma_{rc}) = 2\left(\frac{-Y_{|v|v}}{\rho A_{L_c}}\right)\sin(\gamma_{rc})|\sin(\gamma_{rc})| \tag{2.20b}$$

$$C_{N_c}(\gamma_{rc}) = \frac{2}{\rho A_{L_c}L_{0a}}(-N_{|v|v}\sin(\gamma_{rc})|\sin(\gamma_{rc})| + \frac{1}{2}(X_{\dot{u}} - Y_{\dot{v}})\sin(2\gamma_{rc})). \tag{2.20c}$$

Here, ρ is the density of water, and the subscript c denotes current parameters which make γ_{rc} the angle of attack of the current, V_{rc} is the relative velocity between the vessel and the current, and A_{F_c} and A_{L_c} are the frontal and lateral projected currents areas respectively.

2.2 Motion Control

Motion control describes how to achieve desired movement. A flow chart shown in Figure 2.2 shows an example of subsystems that can be used to achieve motion control.

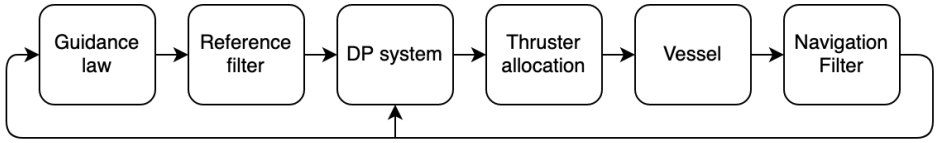

Figure 2.2: Flow chart for achievement of motion control.

2.2.1 Dynamic Positioning

A simple FB and a FF controller can be implemented to keep the surface vessel on a desired trajectory. To handle constant disturbances in NED, the FB controller is suggested to be implemented as a proportional-integral-derivative (PID) controller

$$\boldsymbol{\tau}_{FB} = -\boldsymbol{R}^{\top}(\psi)\boldsymbol{K}_p(\boldsymbol{\eta}-\boldsymbol{\eta}_d) - \boldsymbol{K}_{damping}(\boldsymbol{\nu}-\boldsymbol{\nu}_d) - \boldsymbol{R}^{\top}(\psi)\boldsymbol{K}_i\int_0^t(\boldsymbol{\eta}-\boldsymbol{\eta}_d)dt, \quad (2.21)$$

where $\boldsymbol{K}_p, \boldsymbol{K}_i, \boldsymbol{K}_{damping} \in \mathbb{R}^{3\times3}$ are design gain matrices with $\boldsymbol{K}_p, \boldsymbol{K}_i, \boldsymbol{K}_{damping} \geq 0$, and where the subscript d denotes the desired value. The error is defined in NED because current is considered as the greatest disturbance. By having the integrator in NED, constant disturbances can be compensated for in NED. If the disturbance come from a bias in body, say the motor was mounted with an angle grater than zero, relative to the bow, this constant disturbance in body could be handled with an integration of the body error.

A FF controller can be used to predict and apply the needed force for the desired movement. For control purposes it is convenient to describe the model in terms of the applied actuator force. For now, in this vessel model, the wind and current impact is ignored since the disturbances are considered not measured, but the real environment is still considered to include these disturbances. From (2.6), it can be derived

$$\boldsymbol{\tau} = \boldsymbol{F}(\dot{\boldsymbol{\nu}}, \boldsymbol{\nu}) = \boldsymbol{M}\dot{\boldsymbol{\nu}} + \boldsymbol{C}(\boldsymbol{\nu})\boldsymbol{\nu} + \boldsymbol{D}(\boldsymbol{\nu}). \quad (2.22)$$

When the model is described in this way, the FF control signal gets generated by inserting the desired values for the vessel states into the model

$$\boldsymbol{\tau}_{FF} = \boldsymbol{F}(\dot{\boldsymbol{\nu}}_d, \boldsymbol{\nu}_d), \quad (2.23)$$

so that when applying the force to the real system, the desired speed and acceleration follow. If the FF model is perfect, the FB controller is not needed. However, the model is never perfect and hence the FB controller is needed to support the FF controller. An important aspect of a FF controller is its independence to vessel state measurements which makes the FF controller robust against process noise. In a FB controller, a force gets applied if there is a deviation between the measurement state and the desired state. A FF controller is, therefore, faster than a FB controller because it makes adjustments before a deviation between desired and actual movement occurs. Together, the FF controller and the FB controller form a DP controller

$$\boldsymbol{\tau}_d = \boldsymbol{\tau}_{FB} + \boldsymbol{\tau}_{FF}, \quad (2.24)$$

where the subscript d denotes the desired control action.

2.2.2 Trajectory Tracking

Following a smooth, time varying trajectory $\boldsymbol{\eta}_d(t)$ is accomplished by driving the trajectory error to zero. The trajectory error is defined as

$$\boldsymbol{e}(t) \coloneqq \boldsymbol{\eta}(t) - \boldsymbol{\eta}_d(t) \tag{2.25}$$

where $\boldsymbol{e}(t) \in \mathbb{R}^{3\times 1}$ is the trajectory error at time t. The reference signal $\boldsymbol{\eta}_d$ is generated by filtering the desired waypoints with a third-order filter. The waypoints consist of the desired pose. The filtration ensures a smooth and continuous reference signal for the position, velocity, and accelerations making the trajectory tracking task feasible for the surface vessel since the waypoints are steps in the desired position and heading. The filter is described in a vectorial setting by

$$\boldsymbol{\eta}_d^{(3)} + (2\boldsymbol{\Delta} + I)\boldsymbol{\Omega}\ddot{\eta}_d + (2\boldsymbol{\Delta} + I)\boldsymbol{\Omega}^2 + \boldsymbol{\Omega}^3\boldsymbol{\eta}_d = \boldsymbol{\Omega}^3\boldsymbol{r}, \tag{2.26}$$

where $\boldsymbol{\Omega}, \boldsymbol{\Delta} \in \mathbb{R}^{3\times 3}$ are positive definite design matrices that determine the dynamics of the filter, and where $\boldsymbol{r}$ is the reference setpoint. For the dynamics of the filter, $\boldsymbol{\Delta}$ is the damping ratios, while $\boldsymbol{\Omega}$ is the natural frequencies. Saturating elements are included in the integrals to ensure feasible reference signals.

2.2.3 Path Following

When ignoring the timing aspect of trajectory tracking, the problem simplifies to path following. The path is defined by a set of waypoints in the NED frame that can also include the desired heading.

LOS guidance can be used for path following. There are two types of LOS guidance laws described in Fossen (2011); enclosure-based steering and look-ahead-based steering. What differs the two methods is how the (x_{los}, y_{los}) point in Figure 2.3, is determined. Enclosure-based steering defines the point to be a constant distance away from the vessel, while look-ahead based steering uses a constant along-track distance to determine this point. In practice, only the look-ahead-based steering approach is used.

Look-ahead Based Steering

Look-ahead-based steering is mainly designed for under-actuated vessels, which usually means that a rudder is used to generate a rotational force. The guidance system finds a heading by aiming for a setpoint on the path that is a determined length in front of the vessel's projected position into the path. A common way to implement look-ahead-based steering is to have two separate controllers; one for heading and one for speed.

2.3 Multivariate Modeling and Analysis

This section presents the remaining theory needed to understand how the new contributions to the adaptive controller presented in Chapter 3 work.

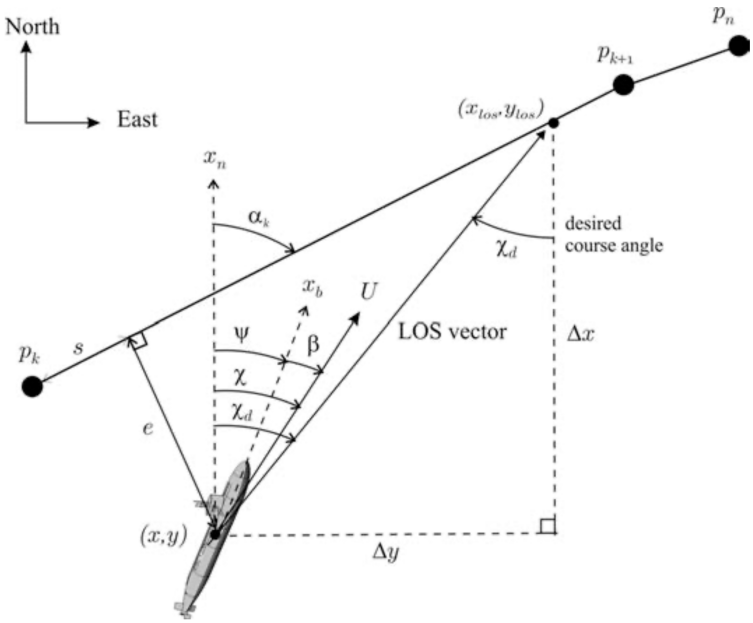

Figure 2.3: Look-ahead based line-of-sight guidance by courtesy of Fossen (2011). All variables follow the Society of Naval Architects and Marine Engineers notation.

2.3.1 Big Data Cybernetics

Big data cybernetics is HAM in the context of adaptive control in cybernetics (Rasheed et al., 2019). HAM combines the best of several research fields; machine learning, big data, and physics based modeling (Tekna, 2019). Figure 2.4 shows how HAM is implemented in cybernetics as BDC (Rasheed et al., 2019). Figure 2.5 shows the pipeline used in HAM to develop a model.

2.3.2 Principal Component Analysis

Principal component analysis (PCA) can be used to find underlying structures of a data set $\boldsymbol{X}$ (Esbensen et al., 2002). This method is useful for finding the core properties of a data set and can optimize the best way to represent a data set when reducing the dimensionality. With $\boldsymbol{X} \in \mathbb{R}^{N \times J}$, the PCA of the $j_{th} \in \{1, 2, \ldots, J\}$ order is

$$\boldsymbol{X} = \boldsymbol{T}_j \boldsymbol{P}_j^\top + \boldsymbol{E}_j, \tag{2.27}$$

where $\boldsymbol{T}_j \in \mathbb{R}^{N \times j}$ are the scores for $\boldsymbol{X}$, $\boldsymbol{P}_j \in \mathbb{R}^{J \times j}$ are the loadings for $\boldsymbol{X}$ and $\boldsymbol{E}_j \in \mathbb{R}^{N \times J}$ is the residual. N and J is the number of samples and dimensions respectively. Figure 2.6 shows the visualization of a second order PCA on a data set. The columns in $\boldsymbol{P}_j$ are the principal components and represent the new axes in the subspace $\mathbb{R}^j \subseteq \mathbb{R}^J$ of the original vector space and the scores $\boldsymbol{T}_j$ are interpreted as the coordinates of the data points in $\boldsymbol{X}$ in the new subspace.

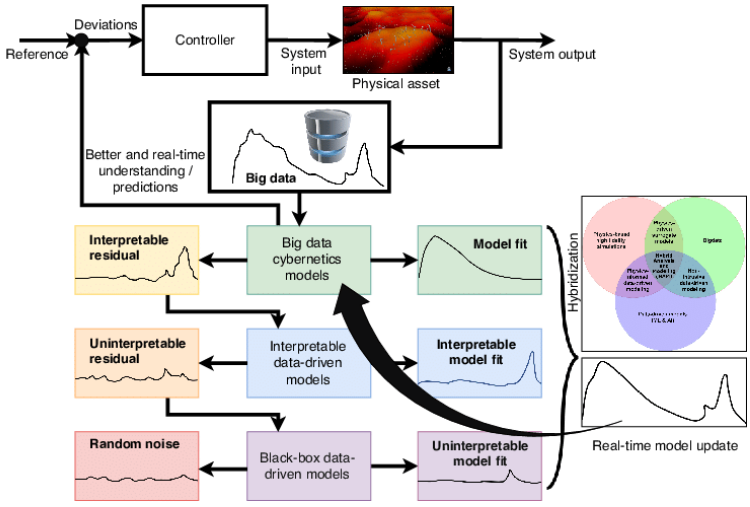

(a) Big data cybernetics.

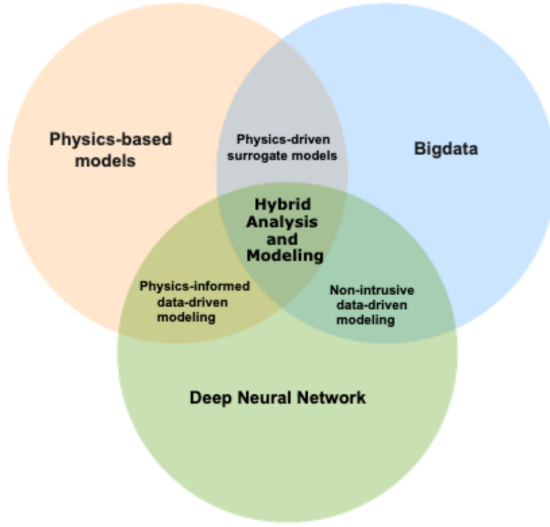

(b) Hybrid analysis and modeling.

Figure 2.4: Hybrid analysis and modeling in the context of big data cybernetics by courtesy of Rasheed et al. (2019).

2.3.3 Partial Least Squares Regression

Partial least squares (PLS) regression can be used to find underlying structures between two data sets. In the case of two data sets $\boldsymbol{X} \in \mathbb{R}^{N \times K}$ and $\boldsymbol{Y} \in \mathbb{R}^{N \times k}$, the goal is to

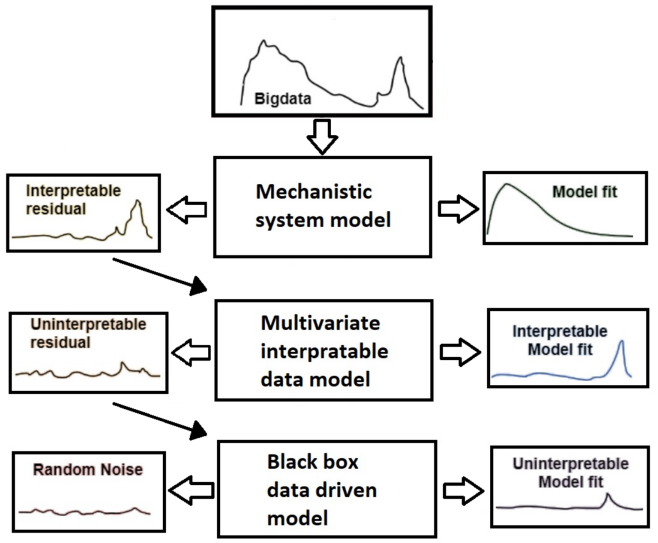

Figure 2.5: The pipeline from data generation to data analysis to the new obtained model by courtesy of Tekna (2019).

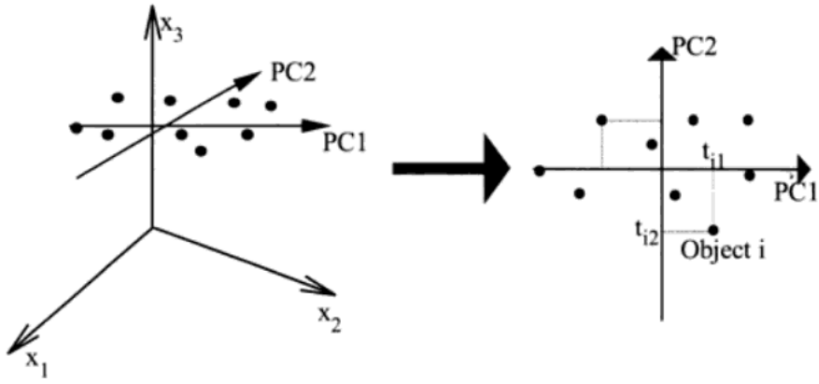

Figure 2.6: A visualization of PCA, by courtesy of Esbensen et al. (2002).

predict $\boldsymbol{Y}$ with a linear combination of $\boldsymbol{X}$ according to

$$\hat{\boldsymbol{Y}} = [\mathbf{1}, \boldsymbol{X}]\boldsymbol{\beta}, \tag{2.28}$$

where $\mathbf{1} \in \mathbb{R}^{N\times 1}$ is a vector, $\boldsymbol{\beta} \in \mathbb{R}^{K+1\times k}$ is a matrix where k is the number of output dimensions, K is the number of input dimensions, and N is the number of samples. In the analysis the correlation between $\boldsymbol{X}$ and $\boldsymbol{Y}$ is maximized so that the residual $\boldsymbol{E}$ in

$$\boldsymbol{Y} = [\mathbf{1}, \boldsymbol{X}]\boldsymbol{\beta} + \boldsymbol{E}, \tag{2.29}$$

is minimized.

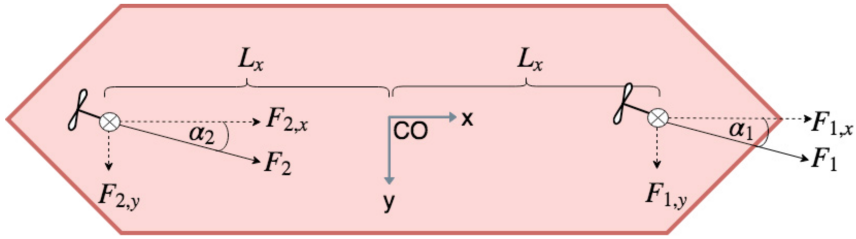

Figure 2.7: Symmetrical two-thruster configuration for double ended vessels, by courtesy of Torben et al. (2019).

Simple Partial Least Squares

The simple partial least squares (SIMPLS) algorithm can be used for PLS regression (De Jong, 1993). The nonlinear iterative partial least squares (NIPALS) algorithm is an alternative algorithm that Jervan (2020) and Gale et al. (2017) use in the MVA for generating new models. The SIMPLS algorithm offers several advantages over the standard NIPALS algorithm (De Jong, 1993). The most important for modeling purposes is that for multivariate $\boldsymbol{Y}$, the SIMPLS algorithm truly maximizes the co-variance criterion, when referring to the original data sets. Secondly, the SIMPLS does not involve a breakdown of the $\boldsymbol{X}$ and/or the $\boldsymbol{Y}$ matrix making it faster and less memory needy than the NIPALS algorithm. Thirdly, it is easier to extract the regressions for direct usage when the factors are already expressed as a linear combination of the original data sets. Alin (2009) verifies that when the number of objects N is much larger than the number of variables K, for $\boldsymbol{X} \in \mathbb{R}^{N \times K}$, the SIMPLS algorithm is not as time consuming as the NIPALS algorithm. Appendix A lists the SIMPLS algorithm as explained by De Jong (1993).

2.4 Control Allocation

For vessels where the control force $\boldsymbol{\tau}$ is indirectly applied by rotating azimuth thrusters, control allocation is needed. Control allocation is a problem where the goal is to find the optimal realization to a control signal subject to constraints and cost functions. For double ended vessels with symmetrical thruster configuration, nonlinear scalar control allocation (NSCA) can be used to solve the control allocation problem (Torben et al., 2019). The method finds the solution to

$$F_{1,x_d} + F_{2,x_d} = X_d \tag{2.30}$$

$$F_{1,y_d} = \frac{N_d + L_s Y_d}{2L_x} \tag{2.31}$$

$$F_{2,y_d} = \frac{N_d - L_s Y_d}{2L_x} \tag{2.32}$$

, where $F_{1,x}$, $F_{1,y}$, $F_{2,x}$, and $F_{2,y}$ are the decomposed azimuth forces in the body frame for the two thrusters respectively, as shown in Figure 2.7. The control force setpoint is

realizes by

$$\boldsymbol{\tau}_d = [X_d, Y_d, N_d]^\top = F_1(\alpha_{1_d}, \omega_{1_d}) + F_2(\alpha_{2_d}, \omega_{2_d}) \tag{2.33}$$

$$\boldsymbol{\tau} = F_1(\alpha_1, \omega_1) + F_2(\alpha_2, \omega_2) \tag{2.34}$$

, where X_d, Y_d, N_d are the desired forces and moment for surge, sway and yaw, respectively, and where α_1, α_2 and ω_1, ω_2 is the azimuth angles and propeller rpm respectively. A separate controller makes the azimuth thrusters obtain the desired set point angle and rpm for each thruster.

2.5 Robot Operating System

ROS is a flexible open-source framework for robotic software development (Quigley et al., 2009). Robot systems are complicated and often rely on many advanced subsystems. Some teams might be experts in sensor fusion, while others are experts in deep neural networks for object detection. The idea behind ROS is to encourage collaboration so that groups can take advantage of each other's expertise. The ROS framework is built in such a way that using others packages is easy to implement in your system.

Chapter 3

Improvements of Existing Methods

In this chapter, the new methods developed for more precise motion control are presented.

3.1 Carrot-based Steering

Carrot-based steering is a new path following guidance system by Aurlien (2020) that is designed for getting the most out of a good vessel model during path following. Traditionally, path-following guidance systems are separated into two independent control systems, a heading controller and a speed controller. Such a control system is designed for autopilots on large ships that mostly move in relatively straight lines using a rudder to control the heading. As mentioned in Chapter 1, smaller fully autonomous vessels start being a reality, and with this development, new navigation laws are needed to better fit the control purposes and abilities of the vessels.

Smaller marine vessels, such as milliAmpere and milliAmpere 2, having azimuth thrusters, are fully actuated and can apply a force in any direction at any time. This makes the LOS approach more restricting than it needs since the course control is independent of the heading control. Additionally, when dealing with high precision control, it is also an advantage if the FF controller described in Section 2.2.1 can be utilized. The generation of a set of position, speed, and acceleration references are not straightforward with the lookahead-based guidance system described in Section 2.2.3. A step in the speed reference signal is not feasible for the system to follow, which shows that the control problem needs adjustments to use a FF controller.

Jervan (2020) used enclosure-based steering in combination with a reference filter for his normal operation test of the adaptive controller. By doing this, the adaptive controller could be used to its full potential for the path following. However, the enclosure-based approach is, in some cases unfitted due to situations where the LOS point is undefined. When replicating his results with the better defined and more commonly used lookahead-based

approach, the speed and acceleration references were observed to be counter-intuitive to a human's approach to the turning movement by accelerating and increasing the speed through the turn and decelerate when finishing the turn. This gave the inspiration to make adjustments that would fix this undesired behavior and creating a new path-following guidance law for FF based control. In the carrot-based steering approach, an imaginary "carrot" is placed in front of the vessel representing a desired pose in the near future. By describing this carrot relative to the current pose of the vessel and update the carrot every time step, the motion is planned into the future without describing it as a trajectory problem where the timing aspects of the pose are considered. Compared to Jervan's (2020) approach to the FF based controller, where the carrot is locked to a specific distance away from the vessel, the new steering by Aurlien (2020) adapts the position of the carrot to ensure smooth and well-defined movements. A detailed description of the algorithm and steering law is described in Appendix B. Since the vessel position is used to place the carrot, one might argue that this is not fully FF based. The reference filter will, however, dampen out all significant impact of measurement noise, leading to smooth reference signals used by the FF controller.

The Carrot-based steering approach to path following combines the best from lookahead-based steering and optimal control approach. In optimal control, the system generates an ideal trajectory for a given time horizon. The trajectory $\boldsymbol{\eta}_d(t)$ can further be used to generate the speed and acceleration references by taking the derivative. The obtained reference signals are then used by the FF and a FB to ensure that the control object stays on its trajectory due to model errors. In the carrot-based steering approach, a trajectory to the carrot is calculated every time step. This approach shares some similarities to model predictive control (MPC) as well because the FF control action adapts to the current pose, unlike the optimal control approach. The relative pose between the vessel and the carrot is fed into a third-order reference filter generating the trajectory. The first step of this trajectory is used by the FF, and the pose of the carrot gets updated according to the steering law.

When the steering law was designed, there were two important criteria:

1. The steering law must result in a set of feasible references that can be used by the FF controller.
2. The movement of the vessel must be comfortable for passengers.

The second criterion relates to the speed reduction in the transition between two path segments. This is a concept many of us have experienced when driving with cruise control. Maintaining the speed through a turn can be uncomfortable. To accomplish a comfortable turning motion, the throttle can be released while gliding through the turn before accelerating towards the exit of the turn. The turning operation happens for a reason and is probably to avoid obstacles close to the vessel. Thus, it makes perfect sense to also reduce speed to ensure a precise and controlled motion.

Figure 3.1 shows the different phases of the carrot-based path following where the "carrot" is considered as the tip of the trajectory planning distance. The first phase shows the approach towards the active waypoint. In this phase, the carrot is placed on the path a

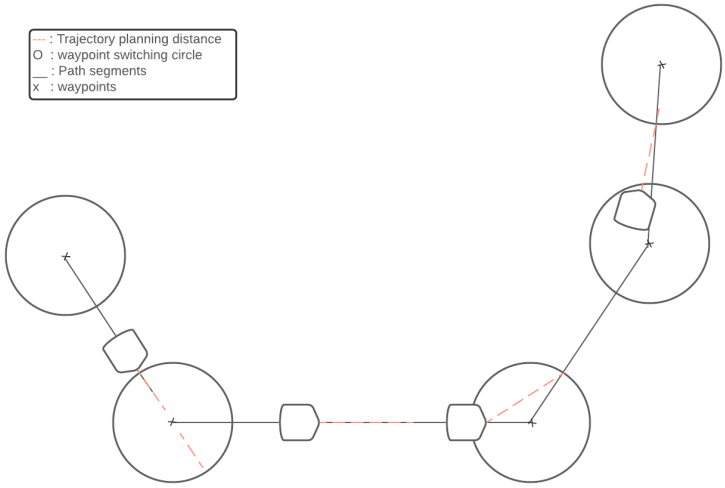

Figure 3.1: Carrot-based guidance.

chosen along-track-distance in front of the vessel. This aiming technique is similar to the look-ahead-based steering law described by Fossen (2011). When the vessel enters the switching radius, the carrot is rebased and stays stationary at the intersection between the new path segment and the switching circle rim. Once the along-track distance greater than zero, switching to the first phase completes the exit of the turn and starts the transition towards the next waypoint. The reference filter makes the vessel brake harder for sharper turns because the vessel is closer to the carrot. The trajectory will always end in a full stop at the desired waypoint. Turns sharper than $90°$, skipping phase two is no problem because the reference filter is defined in NED, leading to hard deceleration when the velocity and acceleration references are rotated into the body frame.

3.2 Multivariate Modeling and Analysis

The improvements suggested for the multivariate modeling and analysis are based on the work done by Jervan (2020). With the improvements, the system handles wind disturbances, and the improved model is selected automatically.

3.2.1 Lack-of-fit Residual

The lack-of-fit residual is a measure for a model error. For the specific surface vessel model described in this thesis (2.23), the precision can be tested by comparing historical data of the applied actuator force and the force that the model estimates was applied. In this thesis, the measured actuator force is considered to be perfect. If this assumption is correct, it can be used to gain information on how bad or good our model understands the behavior of the system. By analyzing and finding meaning in the lack-of-fit residual,

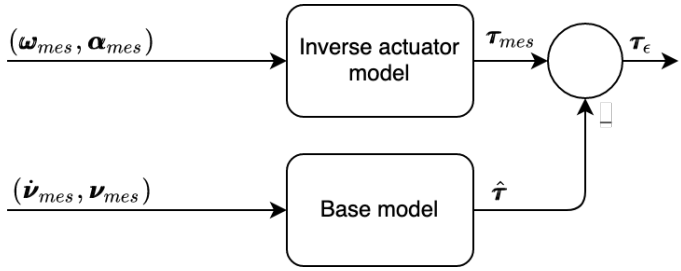

Figure 3.2: A block diagram showing the generation of the lack-of-fit residual.

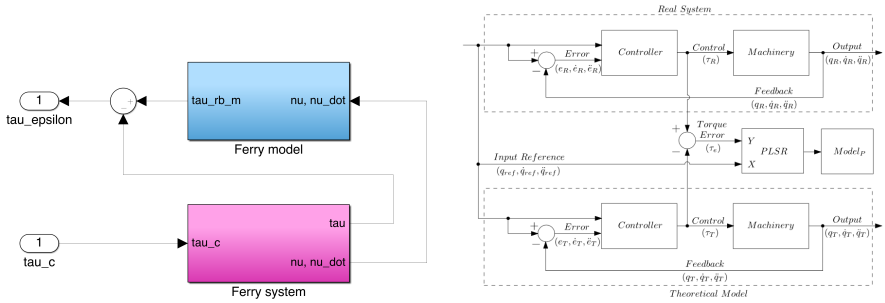

(a) The lack-of-fit residual iteration of Jervan (2020) designed for surface vessels.

(b) The generation of the lack-of-fit residual, by courtesy of Gale et al. (2017).

Figure 3.3: The generation for the lack-of-fit residual by a) Jervan (2020) and b) Gale et al. (2017).

new information is obtained, leading to a better model. Figure 3.2 shows how the lack of fit residual for a surface vessel model can be generated. Here, the lack of fit residual is defined as

$$\boldsymbol{\tau}_{\epsilon} \triangleq \boldsymbol{\tau}_{mes} - \hat{\boldsymbol{\tau}}, \tag{3.1}$$

with $\boldsymbol{\tau}_{mes}(\boldsymbol{\omega}_{mes}, \boldsymbol{\alpha}_{mes})$ being the inverse actuator model and where $\hat{\boldsymbol{\tau}} = \boldsymbol{F}(\dot{\boldsymbol{\nu}}_{mes}, \boldsymbol{\nu}_{mes})$ is the surface vessel model. $\boldsymbol{\omega}_{mes}, \boldsymbol{\alpha}_{mes} \in \mathbb{R}^{a \times 1}$ are vectors that store the propeller rpm and azimuth angle for a number of thrusters respectively.

The approach shown in Figure 3.2 is slightly different from the approach by Gale et al. (2017) and Jervan (2020). The idea of system analysis using partial least squares originated from Wold et al. (1983), and was further iterated by Gale et al. (2017) using the method to improve the model and control of a robotic manipulator. The solution of Gale et al. (2017) is shown in Figure 3.3b. Jervan (2020) further used this technique to suggest an adaptive controller for surface vessels. The generation of the lack-of-fit residual is shown in Figure 3.3a. The two approaches to the generation of the lack-of-fit residual are slightly different. Gale et al. (2017) compare the real system against a simulation of the system. Jervan (2020) uses the inverse vessel model to simplify the implementation process, but the concept of assessing how well the model performs compared to real behavior stays the same. Due to actuator dynamics, the reverse actuator model is needed to generate the

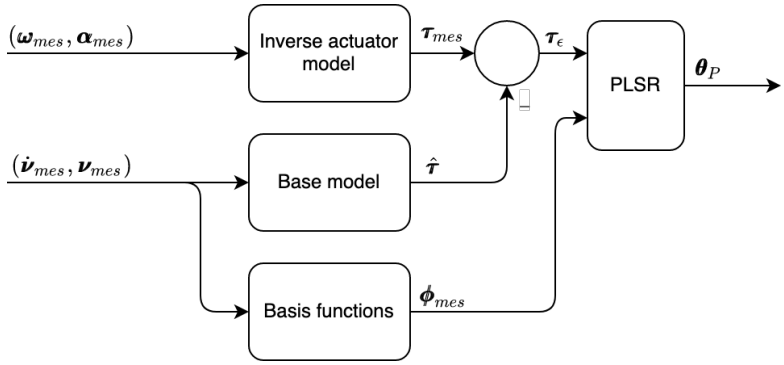

Figure 3.4: A block diagram showing the generation of new models.

lack-of-fit residual in practice. According to Jervan (2020), the control setpoint $\boldsymbol{\tau}_d$ can be used instead of $\boldsymbol{\tau}_{mes}$, depending on the signal to be optimized. Here, $\boldsymbol{\tau}_d$ should be used for best trajectory tracking performance since the lack-of-fit residual also include components describing the actuator dynamics. This approach is questionable. It is suggested to create a model using vessel states to estimate the control setpoint. Due to the delay in the actuator dynamics, the control setpoint needs to be ahead in time to perfectly compensate for the delaying mechanics for realizing the desired movement in time. The approach might be possible in theory, and a model for the dynamics might be fitted by adding additional measurements for the jerk and acceleration of the azimuth angle and rpm. However, for all practical considerations, this is an over-complicated and possible infeasible approach to the problem.

3.2.2 Updating the Model

The process for generating new models are shown in Figure 3.4. If measuring wave and current, $V_{rw}, V_{rc}, \gamma_{rw}$, and γ_{rc} should also be included as input to the base model and basis functions blocks of Figure 3.4. The base model only uses the measurements if a relevant model already exist since the base model is not normally updated. The lack-of-fit residual is modeled, using PLS regression as a linear combination of a set of basis functions. For a successful analysis, the lack-of-fit residual can be described as

$$\boldsymbol{\tau}_{\epsilon}(t) \approx \boldsymbol{\theta}^{\top} \boldsymbol{\phi}(t), \tag{3.2}$$

where $\boldsymbol{\phi}(t) \in \mathbb{R}^{b \times 1}$ are the selected basis functions dependent on the measurements, $\boldsymbol{\theta} \in \mathbb{R}^{b \times 3}$ is the scores of the selected basis functions, and b is the number of basis functions used. $\boldsymbol{\theta}_P$ is later used as Model P when the model is used in the DP system. In a real environment there will always be noise and components to the lack-of-fit-residual that can not be modeled, hence $\boldsymbol{\theta}^{\top}\boldsymbol{\phi}$ is only an approximation to the lack-of-fit residual. Compared with (2.28), $\boldsymbol{\phi} \in \mathbb{R}^{(K+1)\times N} = [\mathbf{1}, \boldsymbol{X}]^{\top}$, while $\mathbf{E}$ contains the rest of the unmodeled components of the lack-of-fit residual.

The more realistic approach, which is also suggested by Jervan (2020), and how this is done in practice, is the approach taken in this thesis. The new approach by Jervan (2020)

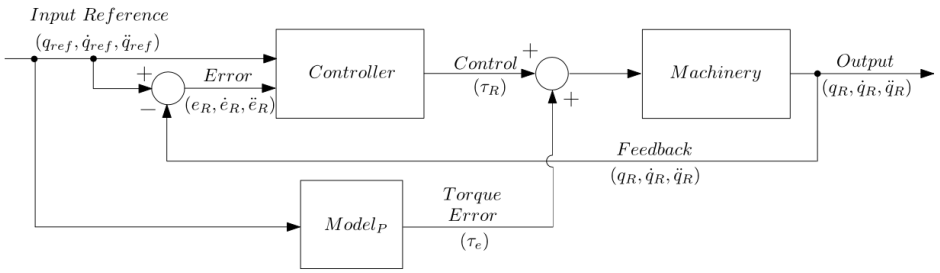

Figure 3.5: Error prediction and compensation where $Model_P$ corresponds to the P^{th} model update, by courtesy of Gale et al. (2017).

that skips the parallel simulated system suggested by Gale et al. (2017), is on the other hand, completely fine.

The advantage of describing the lack of fit residual as done in (3.1) is that the improved model can be described by

$$\boldsymbol{F}_P(\dot{\boldsymbol{\nu}}, \boldsymbol{\nu}, \boldsymbol{\phi}) = \boldsymbol{M}\dot{\boldsymbol{\nu}} + \boldsymbol{C}\boldsymbol{\nu} + \boldsymbol{D}\boldsymbol{\nu} + \boldsymbol{\theta}_P^\top \boldsymbol{\phi}, \tag{3.3}$$

where P denotes the P^{th} model update. Figure 3.5 shows a block diagram of how the model is used to obtain more precise control signals (Gale et al., 2017).

3.2.3 Model Variables

A good approach to model the lack of fit residual is to use the decoupled 3-DOF model introduced in Chapter 2, since it is assumed that this model is accurate when correctly fitted. To be able to use the PLS regression method introduced in Section 2.3.3 to model the lack-of-fit residual, a linear-combination of the selected basis functions must be a good fit. The basis functions of the 3-DOF decoupled model is deduced from writing out (2.6) and removing all the parameters leaving only the variables. The terms that are left are

$$\begin{aligned}\boldsymbol{\phi}_1 = [&\dot{u}, \dot{v}, \dot{r}, uv, ur, vr, rr, u, v, r, sgn(u)u^2, sgn(v)v^2, \\ &sgn(r)r^2, u^3, v^3, r^3, |u|u, |v|v, |r|r|v|r, |r|v]^\top.\end{aligned} \tag{3.4}$$

Repeating the same strategy for (2.15) to find the basis functions for wind does, unfortunately, not result in a linear combination of variables because the denominator of C_{Y_w} in itself is a linear combination of variables. According to Fossen (2011), the wind coefficients can be approximated by

$$C_{X_w}(\gamma_{rw}) \approx -c_x \cos(\gamma_{rw}) \tag{3.5a}$$
$$C_{Y_w}(\gamma_{rw}) \approx c_y \sin(\gamma_{rw}) \tag{3.5b}$$
$$C_{N_w}(\gamma_{rw}) \approx c_n \sin(2\gamma_{rw}). \tag{3.5c}$$

When these approximations are used instead of (2.18), $\boldsymbol{\tau}_{wind}$ is described as a linear combination of the basis functions

$$\boldsymbol{\phi}_2 = [V_{rw}^2 \cos(\gamma_{rw}), V_{rw}^2 \sin(\gamma_{rw}), V_{rw}^2 \sin(2\gamma_{rw})]^\top, \tag{3.6}$$

when the equation is fully written out.

Finally the basis functions that describe (2.19) as a linear combination are

$$\boldsymbol{\phi}_3 = [V_{rc}^2 \cos(\gamma_{rc})|\cos(\gamma_{rc})|, V_{rc}^2 \sin(\gamma_{rc})|\sin(\gamma_{rc})|, V_{rc}^2 sin(\gamma_{rc}), V_{rc}^2 \sin(2\gamma_{rc}). \tag{3.7}$$

A collection of all the basis functions can be defined as

$$\boldsymbol{\phi} = [\boldsymbol{\phi}_1^\top, \boldsymbol{\phi}_2^\top, \boldsymbol{\phi}_3^\top]^\top, \tag{3.8}$$

and are the selected basis functions for the MVA.

3.2.4 Updating Criterion

An updating criterion is needed for the adaptive controller to automatically suggest new model updates. Depending on what to model, the strategy varies. To compensate for passenger load, quick updates are needed to take advantage of the model before the passengers leave the ferry. On the other hand, it is preferable to have as much data as possible in our data set to ensure that the signal is persistent excitation (PE). A fresh test set is also needed since the real dynamics might have changed. A suggested updating criterion to compensate for passenger load can be as follows: Use half of a channel crossing as data material. Extract every k sample of the data material and define the extracted samples as the validation set. The remaining part of the data material is used as the training set. If the new model significantly improves the mean squared error (MSE) of the estimated applied actuator force, which will be an improvement of $5\ \%$ or more, the model is accepted and replaces the previous one. The validation step is needed because the analysis can fail and lead to a worse model if the training data is not PE.

3.2.5 Updating Base Model

An outer loop model update is a suggestion that can be implemented to assure that the initial model improves over time. A collection of different model updates might result in an oscillation around a specific model. If, for example, the vessels on average carry ten persons, but the base model was generated when only two persons were on board, on average, an adaptive model compensating for eight persons would be found. If this is a lasting trend, the base model could be redefined to be the average of the latest models. The slow updating process is described by

$$\boldsymbol{F}(\dot{\boldsymbol{\nu}}, \boldsymbol{\nu}, \boldsymbol{\phi}) = \frac{1}{S} \sum_{P=1}^{S} \boldsymbol{F}_P(\dot{\boldsymbol{\nu}}, \boldsymbol{\nu}, \boldsymbol{\phi}) \tag{3.9}$$

where S is a predefined constant for the number of models to average.

Chapter 4

System Description and Setup

This chapter shows how the system is implemented to verify how the adaptive controller works. The milliAmpere vessel is also described in detail.

4.1 The milliAmpere Research Vessel

This section presents the system-specific properties for milliAmpere and practical decisions taken to make the system robust.

4.1.1 Vessel Characteristics

The adaptive system is tested for the milliAmpere research vessel shown in Figure 4.1. The vessel has a length of $5\ m$, a beam of $2.8\ m$, and weighs $1670\ kg$. It is controlled by two electric azimuth thrusters delivering up to $500.3\ N$ at $2kW$ each, giving the vessel a top speed of 4.7 knots (Torben et al., 2019; Molven, 2020). The vessel is powered by six $24\ V$ DC batteries with a capacity of $600\ Ah$, corresponding to $14.4kWh$. The thruster configuration of milliAmpere is shown in Figure 2.7, where $L_x = 1.8\ m$.

4.1.2 Surface Vessel Model

For Pedersen's (2019) model used on the main system of milliAmpere, symmetry in the xy and xz is assumed making the CO and CG correspond. The model is therefore simplified to a decoupled 3-DOF model. The parameters are determined in Pedersen (2019) and are listed in Table 4.1. Pedersen (2019) also estimated the wind load parameters for milliAmpere listed in Table 4.2.

Table 4.1: Estimated parameters for the model for milliAmpere (Pedersen, 2019).

Parameter	Value	Parameter	Value
m_{11}	2389.657	$Y_{\|v\|v}$	-116.486
m_{12}	0	Y_{vvv}	-24.313
m_{13}	0	$Y_{\|r\|v}$	-1540.383
m_{21}	0	Y_r	24.732
m_{22}	2533.911	$Y_{\|v\|r}$	572.141
m_{23}	62.386	$Y_{\|r\|r}$	-115.457
m_{31}	0	N_v	3.524
m_{32}	28.141	$N_{\|v\|v}$	-0.832
m_{33}	5068.910	$N_{\|r\|v}$	336.827
X_u	-27.632	N_r	-122.860
$X_{\|u\|u}$	-110.064	$N_{\|r\|r}$	-874.428
X_{uuu}	-13.965	N_{rrr}	0.000
Y_v	-52.947	$N_{\|v\|r}$	-121.957

Table 4.2: Wind load parameters for milliAmpere found by Pedersen (2019).

Parameter	Value	Description
A_{F_w}	2.9 m^2	Frontal surface area
A_{L_w}	8.6 m^2	Lateral surface area
L_{0a}	5 m	Length overall
S_L	0 m	Centroid projected area on main section
CD_t	0.90	Transverse resistance
$CD_{l_{AF}}$	0.5	Longitudinal resistance
δ	0.80	Cross-force
κ	1.1	Rolling moment

Figure 4.1: The milliAmpere research vessel.

4.1.3 Thruster Force Model

The thruster force model used on milliAmpere is a fifth-order polynomial

$$F_{1,2}(\omega) = 2.396\,752\,90 \times 10^{-2}\omega + 2.135\,249\,53 \times 10^{-4}\omega^2 + 7.693\,299\,24 \times 10^{-7}\omega^3 \\ -1.081\,512\,33 \times 10^{-10}\omega^4 - 4.096\,994\,44 \times 10^{-13}\omega^5. \quad (4.1)$$

where $F_{1,2}(\omega)$ is the directional force produced by one thruster. To ensure the validity of the model, ω is clipped so that $\omega_{min} < \omega < \omega_{max}$. From here the total force $\boldsymbol{\tau}(\boldsymbol{\omega}, \boldsymbol{\alpha})$ from the two thrusters are calculated by simple geometry. The azimuth angles $\boldsymbol{\alpha} = [\alpha_1, \alpha_2]$ are measured by reading encoder values.

4.1.4 Navigation Sensors

The sensors used for navigation are

- a Real-time kinetic (RTK) global navigation satellite system (GNSS) (Vector^{TM}VS330 GNSS Receiver),
- an Inertial measurement unit (IMU) (Xsens MTi20), and
- an error state Kalman filter (ESKF) taking care of the sensor fusion of the GNSS and IMU data that with an RTK lock on the GNSS measurements deliver positional precision down to centimeters.

4.1.5 Computer Software

The software runs on the on board computer (OBC) that is an Axiomtek eBOX670-883-FL with an Intel Core I7 processor. The environment used is Ubuntu 16.04LTS with the

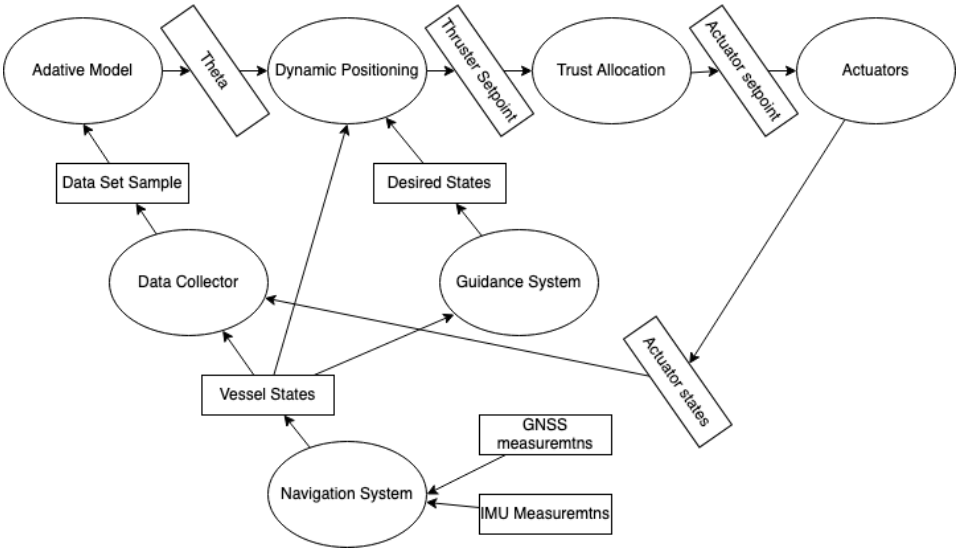

Figure 4.2: A simplified ROS graph of the software implementation. Boxes represent ROS topics, and circles represent ROS nodes. The arrows show nodes publishing to the topics and which topics each node subscribe to.

Kinetic ROS distribution. The vessel is manually controlled by a radio controller and is equipped with two emergency switches.

4.2 ROS Graph

A simplified ROS graph of the system implementation is shown in Figure 4.2.

4.3 Base Model

$\boldsymbol{F}_0$ is referred to as the the model used when booting the adaptive system. The current model of milliAmpere is the model obtained by Pedersen (2019). Since this model is assumed to be good, a scaled version of Pedersen's (2019) model is selected as the base model both for simulations and experiments. In the simulations, Pedersen's (2019) model defines the real dynamics. The system matrices for the base model $\boldsymbol{F}_0$ are defined as

$$\boldsymbol{M} = \delta \boldsymbol{M}^* \tag{4.2}$$

$$\boldsymbol{C}(\boldsymbol{\nu}) = \delta \boldsymbol{C}^*(\boldsymbol{\nu}) \tag{4.3}$$

$$\boldsymbol{D}(\boldsymbol{\nu}) = \sigma \boldsymbol{D}^*(\boldsymbol{\nu}) \tag{4.4}$$

$$\boldsymbol{\tau} = \zeta \boldsymbol{\tau}^*, \tag{4.5}$$

where $\delta = \sigma = 0.4$, $\zeta = 1$, and * denotes Pedersen's (2019) model. This ensures that components in the lack-of-fit residual can be found that the adaptive system can model.

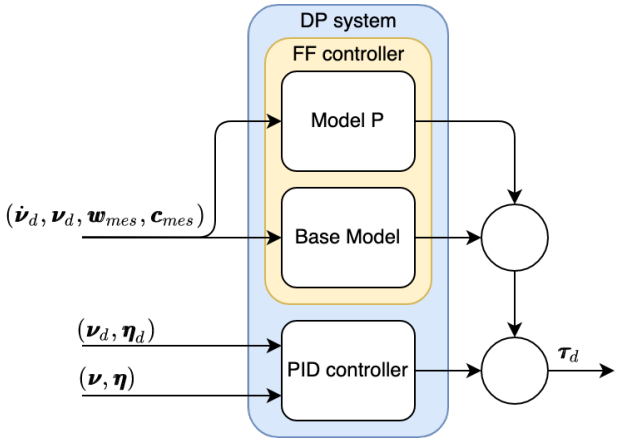

Figure 4.3: A block diagram of the DP system.

The slow outer updating loop suggested in Section 3.2.5 and the updating criterion in Section 3.2.4 are not implemented for the tests in this thesis because these topics are problems that need to be tuned for the specific operation the adaptive controller is used in, but also because the implementations can interrupt the predictability of the model updates when testing the adaptive controller.

4.4 Implementation of the Controller

The adaptive part of the FF controller is separated from the initial FF controller. Figure 4.3 shows how the learned model dynamics are added in the controller. Here, $\boldsymbol{w} = [V_{rw}, \gamma_{rw}]$, and $\boldsymbol{c} = [V_{rc}, \gamma_{rc}]$ are used to simplify the notation for the wind and current measurements.

The values to be used for $\boldsymbol{\phi}$ in the FF should be carefully chosen. The goal for the FF is to apply the control force giving the desired vessel movement according to $\dot{\boldsymbol{\nu}}$ and $\boldsymbol{\nu}$. With (3.3), a new understanding of the rigid body forces acting on the vessel is obtained. The lack-of-fit residual is generated in such a way that when obtaining the model update (3.3), the FF is updated according to

$$\boldsymbol{\tau}_{FF} = \boldsymbol{F}_P(\dot{\boldsymbol{\nu}}_d, \boldsymbol{\nu}_d, \boldsymbol{\phi}_{FF}), \tag{4.6}$$

where $\boldsymbol{\phi}_{FF}(\dot{\boldsymbol{\nu}}_d, \boldsymbol{w}_{mes}, \boldsymbol{c}_{mes}) = [\boldsymbol{\phi}_{1_d}^\top, \boldsymbol{\phi}_{2_{mes}}^\top, \boldsymbol{\phi}_{3_{mes}}^\top]^\top$.

An example, where only the FF is used, can explain why this works. The use of FB is also acceptable, but complicates the equations unnecessarily. In the equations, $\hat{}$ means that it is a model, and * refers to the correct force or model.

Step 1: To start, the rigid body dynamics are

$$\boldsymbol{\tau}^* + \boldsymbol{\tau}_w^* + \boldsymbol{\tau}_c^* = \boldsymbol{\tau}_{RB}^* \triangleq \boldsymbol{M}^*\dot{\boldsymbol{\nu}} + \boldsymbol{C}^*(\boldsymbol{\nu})\boldsymbol{\nu} + \boldsymbol{D}^*(\boldsymbol{\nu})\boldsymbol{\nu}, \tag{4.7a}$$

where the external rigid body forces are on the left-hand side (LHS) and the 3-DOF model by Fossen (2011) on the right-hand side (RHS).

Step 2: The model for the applied actuator force is obtained by

$$\boldsymbol{F}_0(\dot{\boldsymbol{\nu}}, \boldsymbol{\nu}, \boldsymbol{w}, \boldsymbol{c}) = \boldsymbol{M}\dot{\boldsymbol{\nu}} + \boldsymbol{C}(\boldsymbol{\nu})\boldsymbol{\nu} + \boldsymbol{D}(\boldsymbol{\nu})\boldsymbol{\nu} - \hat{\boldsymbol{\tau}}_w(\boldsymbol{w}) - \hat{\boldsymbol{\tau}}_c(\boldsymbol{c}). \tag{4.7b}$$

For the RHS, all terms are filled with whatever model that already exists. The models do not need to be correct.

Step 3: When the control system is only driven by the FF controller, the applied force is

$$\boldsymbol{\tau}^* = \boldsymbol{F}_0(\dot{\boldsymbol{\nu}}_d, \boldsymbol{\nu}_d, \boldsymbol{w}_{mes}, \boldsymbol{c}_{mes}) = \boldsymbol{M}\dot{\boldsymbol{\nu}}_d + \boldsymbol{C}(\boldsymbol{\nu}_d)\boldsymbol{\nu}_d + \boldsymbol{D}(\boldsymbol{\nu}_d)\boldsymbol{\nu}_d - \hat{\boldsymbol{\tau}}(\boldsymbol{w}_{mes}) - \hat{\boldsymbol{\tau}}_c(\boldsymbol{c}_{mes}). \tag{4.7c}$$

Step 4: Use the model to find the estimated actuator force

$$\hat{\boldsymbol{\tau}} = \boldsymbol{M}\dot{\boldsymbol{\nu}}_{mes} + \boldsymbol{C}(\boldsymbol{\nu}_{mes})\boldsymbol{\nu}_{mes} + \boldsymbol{D}(\boldsymbol{\nu}_{mes})\boldsymbol{\nu}_{mes} - \hat{\boldsymbol{\tau}}(\boldsymbol{w}_{mes}) - \hat{\boldsymbol{\tau}}_c(\boldsymbol{c}_{mes}), \tag{4.7d}$$

where the measured vessel velocities and accelerations, wind and current speed and direction are inserted into the models.

Step 5: Generate the lack-of-fit residual

$$\boldsymbol{\tau}_\epsilon \triangleq \boldsymbol{\tau}_{mes} - \hat{\boldsymbol{\tau}} = \boldsymbol{\tau}^* - \boldsymbol{M}\dot{\boldsymbol{\nu}}_{mes} - \boldsymbol{C}(\boldsymbol{\nu}_{mes})\boldsymbol{\nu}_{mes} + \hat{\boldsymbol{\tau}}(\boldsymbol{w}_{mes}) + \hat{\boldsymbol{\tau}}_c(\boldsymbol{c}_{mes}), \tag{4.7e}$$

which is the difference between the measured and estimated actuator force. It is assumed that the measured force is correct and equal to the actual applied force.

Step 6: This step is the crucial part for the adaptive system to work. To show the concept, the the lack-of-fit residual is assumed to be perfectly modeled through the MVA.

$$\hat{\boldsymbol{\tau}}_\epsilon = \hat{\boldsymbol{\tau}}^* - \boldsymbol{M}\dot{\boldsymbol{\nu}} - \boldsymbol{C}(\boldsymbol{\nu})\boldsymbol{\nu} + \hat{\boldsymbol{\tau}}_w(\boldsymbol{w}) + \hat{\boldsymbol{\tau}}_c(\boldsymbol{c}) \tag{4.7f}$$

The overall RHS model include the perfect rigid body model, but also contains neutralizing terms of the existing model.

Step 7: Once the lack of fit residual model is added to the existing model

$$\boldsymbol{F}_1(\dot{\boldsymbol{\nu}}, \boldsymbol{\nu}, \boldsymbol{w}, \boldsymbol{c}) = \boldsymbol{F}_0 + \hat{\boldsymbol{\tau}}_\epsilon = \hat{\boldsymbol{\tau}}^*, \tag{4.7g}$$

the updated model should be the perfect vessel model.

Step 8: The updated model written fully out:

$$\boldsymbol{\tau}^* = \boldsymbol{F}_1(\dot{\boldsymbol{\nu}}, \boldsymbol{\nu}, \boldsymbol{w}, \boldsymbol{c}) = \boldsymbol{M}^*\dot{\boldsymbol{\nu}} + \boldsymbol{C}^*(\boldsymbol{\nu})\boldsymbol{\nu} + \boldsymbol{D}^*(\boldsymbol{\nu})\boldsymbol{\nu} + \hat{\boldsymbol{\tau}}^*_w(\boldsymbol{w}) + \hat{\boldsymbol{\tau}}^*_c(\boldsymbol{c}). \tag{4.7h}$$

To make this to work, the lack-of-fit is generated so that if the lack-of-fit residual is modeled, as in (4.7e), and added to the exiting model $\boldsymbol{F}_0$, the existing model is neutralized, and the new model $\boldsymbol{F}_1$ in (4.7f) is modeling the perfect dynamics. It is, however, only possible to obtain a sub-optimal model of the lack-of-fit residual. This will, nevertheless, lead to an

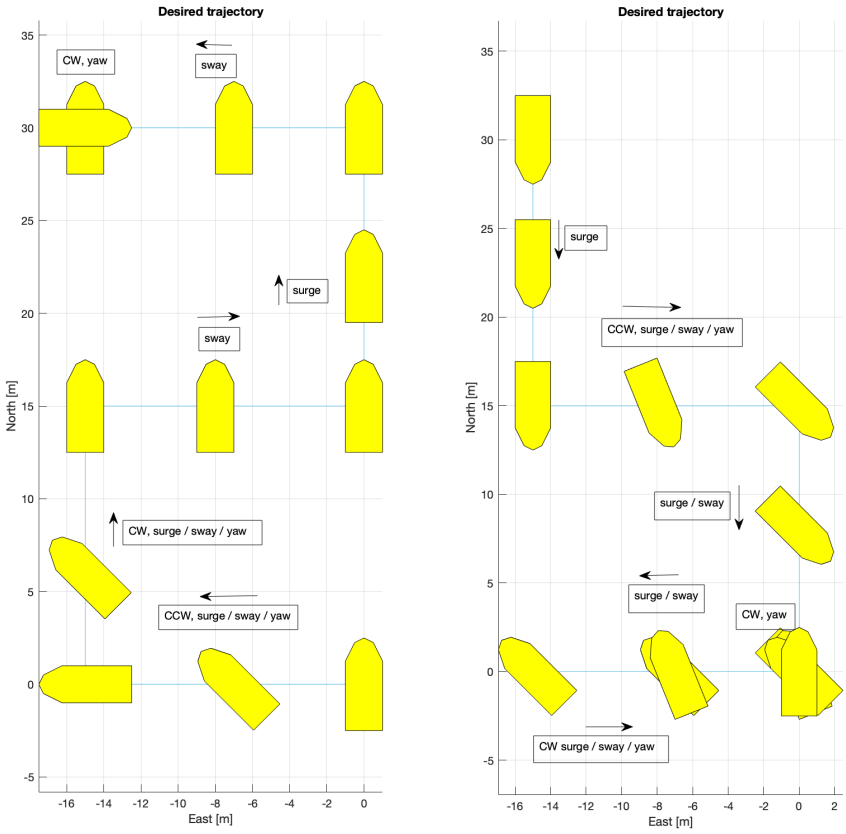

(a) Part one of the 12 corner trajectory.

(b) Part two of the 12 corner trajectory.

Figure 4.4: The calibration trajectory.

improved model. The better the model of the lack-of-fit residual gets, the closer the model is to the perfect model.

The advantage of modeling wind and current is that knowledge of the environment can be used to move more like a sailing ship. Knowledge tells that when moving forward with tailwind, the actuator force can be reduced since the wind will help the vessel to reach its desired movement.

4.5 Calibration Setup

An important concept in adaptive control is the property of PE for the input signal to a system (Ioannou and Sun, 2012). When designing a simulation or experimental test, it is essential to generate a rich signal that can describe the vessel's dynamics accurately.

Table 4.3: Waypoints - 12 corner test, by courtesy of Jervan (2020).

$x(m)$	$y(m)$	$\psi(m)$
0	-15	-90
15	-15	0
15	0	0
30	0	0
30	-15	0
30	-15	180
15	-15	180
15	0	135
0	0	135
0	0	-45
0	-15	-45
0	0	0

Skjetne et al. (2017) suggests using a four corner test to generate information about how the states are coupled. Jervan suggests the 12-corner test, a modified version of the 4-corner test, to be used so that no symmetry is assumed for any direction. It is necessary to include rotation in yaw while sway movement occurs, since a coupling of these states is expected. With this path, the data is expected to be PE. Figure 4.4 shows the path of the 12 corner test.

To generate a feasible trajectory for the 12-corner test, the waypoints are used as setpoints to the reference filter described in 2.2.1. The setpoint is changed every 60 seconds. When the vessel finishes the calibration cycle, it momentarily starts another round in the calibration pattern and automatically generates a model based on the earlier rounds performed during the session. Thus, the model used by the controller during Round 3 is trained with data collected in Round 1 and Round 2.

4.6 Estimation of Body Acceleration

The process of estimating the body acceleration proved to be a more difficult problem than first expected. At first, IMU measurements were used to extract acceleration data for the surge and sway movement. This proved to be impossible because the IMU data is in reality the data used to estimate the pose of milliAmpere. For the pose estimation, it is assumed that the only acceleration the IMU experiences is the g force. This is a good assumption, since the maximum acceleration in the horizontal plane is $0.05\ m/s^2$. This is such a small component compared to the g force that the pose estimation is very accurate, as illustrated in Figure 4.5. With the same argument, using IMU to estimate the body acceleration is close to impossible. The smallest deviations in roll or pitch would make the g force completely dominate the measured acceleration in the horizontal plane. In practice, this could still work using an alternative way to estimate the pose of the vessel. One solution

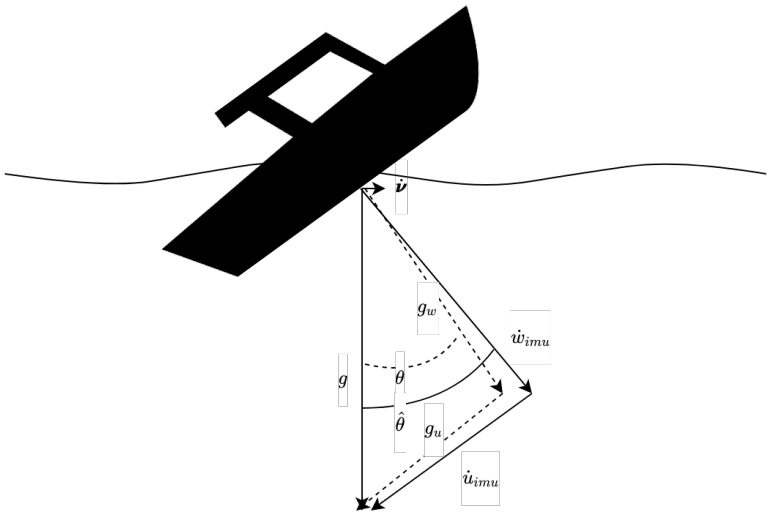

Figure 4.5: Pose estimation.

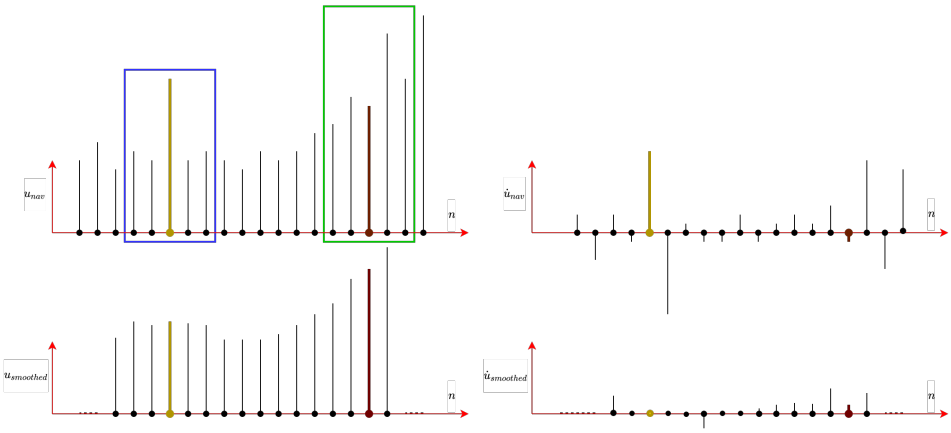

Figure 4.6: Illustration of the smoothing prosess. Here, u_{nav} is the estimated surge velocity by the navigation filter, and $u_{smoothed}$ is the smoothed surge estimate that is used in the MVA.

could be to use three GNSS antennas to estimate the pose, and if the estimates are accurate enough, the impact of the g force could be filtered out in the IMU measurements so that only the actual horizontal acceleration is left.

The way the estimation problem is solved, is to take the numerical derivative of the velocity estimate provided by the navigation filter. This can work because of two important properties of the adaptive system. First, the MVA handles white noise, since a white noise signal is correlation-free. The second property is that the real-time estimates of the ac-

celeration are not needed, since the data will be used as a training set. Since the velocity noise is not white and too big to use in the MVA, the velocity estimates must be improved. Only relative new data is needed, which opens the possibility for post-processing the navigation data by smoothing. This improves the velocity estimates and reduces the impact of colored noise. An illustration of the smoothing process is shown in Figure 4.6. The smoothing process of the velocity estimates proved to be essential for the acceleration estimates to be precise enough for the MVA to work.

Smoothing is a filtering process where data is used, not only from the past, but also from the future. The convolution

$$\boldsymbol{\nu}_{smoothed}(t) = \boldsymbol{\nu}(t) * \boldsymbol{g}(t) = \int_{-\infty}^{\infty} \boldsymbol{\nu}(\xi)\boldsymbol{g}(t-\xi)d\xi, \tag{4.8}$$

where $\boldsymbol{g}$ is a square window, describes the smoothing process. The integral of the window is 1, which in reality makes this an averaging process. The integral is approximated by Euler integration so that our discrete measurements can be used. In practice, the smoothing process is implemented by making a circular buffer that stores all velocity measurements from the window used. Then the average value of the data stored in the buffer is used as the estimate for the mid-value of the velocity buffer. The acceleration is then estimated by taking the derivative of the smoothed velocity signal. The rest of the measurements are also stored in a buffer to ensure that the data is synchronized. With this post-process technique, good estimates for the acceleration are obtained while still having data no older than half the window length, which is no problem at all for our purposes.

A Kalman filter (KF) was also tested, modeling the movement of milliAmpere as a constant acceleration process impacted by process noise. The navigation estimates of the pose and velocity were used as measurements. The tuning process suggested by Brekke (2019) proved to be hard without several experimental tests, and the results obtained were not precise enough for the high standards needed. Additionally, the relaxing property of not needing real-time estimates made the numerical derivative approach with smoothing far superior, both considering robustness and simplicity.

4.7 Performance Metrics

There are many metrics that can be used to evaluate the performance of the system. To compare motion controllers for surface vessels Sørensen and Breivik (2015) suggest the following metrics: The integral of the square of the error (ISE) is defined as

$$ISE = \int_0^t e^2 dt, \tag{4.9}$$

and penalizes large errors more than small errors. The integral of the absolute error (IAE) is defined as

$$IAE = \int_0^t |e| dt, \tag{4.10}$$

and penalizes errors linearly. The integral of the absolute error multiplied by the energy consumption (IAEW) is defined as

$$IAEW = \int_0^t |e(t)|dt \int_0^t P(t)dt, \tag{4.11}$$

and scales the precision with the power usage. In addition, the energy consumption (EC) is interesting to know. The EC defined by

$$EC = \int_0^t P(t)dt, \tag{4.12}$$

where $P = |\boldsymbol{\nu}^\top \boldsymbol{\tau}|$ represents the mechanical power.

To evaluate how much the use of the FB can be limited by an improved FF controller, the power of a signal can be used. The power of a discrete signal x is defined as

$$P_x = \lim_{N\to\infty} \frac{1}{2N} \sum_{n=-\infty}^{n=\infty} |x[n]|^2. \tag{4.13}$$

4.8 Software Upgrade for High Precision of Encoder Values

Before the experiments can take place, the firmware on milliAmpere needs a software update for azimuth thruster angles to be precise. The software update changes the encoder-values of the thruster angles to be represented as floats and not integers. This update is necessary because the applied force deviates from the measured force if the angle is not measured precisely. For the adaptive system to work, it is essential that the measured actuator force can be relied on as the true applied force.

4.9 Practical Considerations

This master thesis is focused on the experimental results and the practical decisions done for the proof of concept of the adaptive controller in real conditions. It was therefore decided to remove some concepts and implementations that were included in Aurlien (2020). The main difference to the approach taken by Aurlien (2020) is not to search for a new theoretical model improving existing models. Thus, multiple potential basis functions, with the intent of removing the basis functions not contributing to the model, are no longer included. This was one of the main contributions by Aurlien (2020), but the process of removing unwanted basis functions proved to be difficult and not very successful. Instead, a 3-DOF decoupled model is assumed to be sufficient to find significant improvements in the model. This is assumed to be a better and more robust approach to the problem since the goal is to detect model changes rather than trying to find a better technique to determine model parameters. However, it is also assumed that the method presented in this thesis is a good approach for model identification in itself.

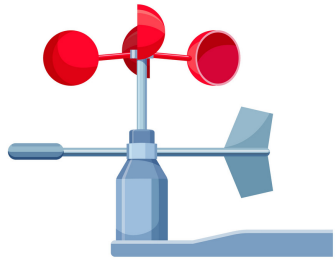

Figure 4.7: An anemometer device that can measure the speed and direction of wind and current flow. By courtesy of Matt Jameson.

It was decided to drop further analysis of current and wind impact, since the simulation results by Aurlien (2020) are quite realistic and promising, showing that the adaptive system is capable of modeling the wind impact quite accurately. Since the current impact is close to identical to the wind impact, there is no reason to believe that simulations should make any practical changes in simulations as long as a signal that is PE can be assured. Therefore, more interesting problems were emphasized, since milliAmpere does not have the opportunity to measure the wind nor the current. Measurements can be added by, for example, installing anemometer devices at the center of the roof and on the outside of the hull. An anemometer is shown in Figure 4.7.

Chapter 5

Simulations and Experimental Results

In this chapter, the results of the simulations and the experiments done to test the adaptive control system are presented. The first experiments are pilot tests included to show the process of how the final adaptive control system is reached. A summary of the key elements from each experiment and why several experiments were needed is shown in Table 5.1.

5.1 Proof of Concept Simulation Results

Proof of concept simulation results for the adaptive controller and the carrot-based steering law are presented in previous work (Aurlien, 2020).

5.2 Pilot Tests

The pilot tests are designed to get familiarized with the experimental environment and to plan further tests. As these tests are not directly representative of the final performance of the adaptive control system, in-depth analysis is not presented.

5.2.1 Pilot Tests Day 1

The importance of the pilot tests day 1 can be summarized by:

Goals

- Familiarizing with the milliAmpere system and procedures.

Table 5.1: Summaray of Experimental tests. The columns are **A**: Good Data Set **B**: Well Tuned Adaptive System, **C**: Well Tuned Reference Filter, **D**: Final Adaptive Control System, **E**: Environmental Disturbances, and **F**: Satisfying Results

Experiment	A	B	C	D	E	F
Pilot tests day 1	Yes	No	No	No	Negligible	No
Pilot tests day 2	Yes	Not optimal	No	No	Negligible	No
Experiment 1	Yes	Yes	Yes	Yes	Wind	Yes
Experiment 2	No	Yes	Yes	Yes	Wind and waves	No
Experiment 3	Yes	Not optimal	No	No	Negligible	Yes

- Verifying the software update for improved azimuth encoder measurements is functioning.
- Collecting data sets to evaluate the closed-loop performance. Differences between simulations and experiments will identify problems that should be targeted in further tests.

Lessons learned

- This version of the adaptive system does not work as intended, as no improvements in the performance metrics occur.
- It is, at this point, assumed that the acceleration estimates are the only cause of the system not improving.

5.2.2 Pilot Tests Day 2

The importance of the pilot tests day 2 can be summarized by:

Goals

- Test if the new acceleration estimates, using the smoothing approach, improve the system performance.
- Finding optimal smoothing window length.

Lessons learned

- Acceleration estimates can not be the sole cause of the non-improving system performance, as the performance still does not improve with better acceleration estimates.
- It can no longer be assumed that the base model used is inaccurate and that it is easy to see improvements with this base model. The system works in the simulator when including noise in the measurements, which indicates that the system has the potential to show good results.

- Discovering that the reference filter used in the DP system is wrongly tuned in earlier work by others, might explain some of the deteriorating performance during the pilot tests. The bad tuning makes the reference signals for velocity and acceleration saturate quickly, leading to sharp and infeasible control signals. Sharp and quick reference signals are not feasible to realize precisely due to delay in the thruster dynamics. Additionally, the desired rounds per minute (RPM) can be reached faster than the desired angle; hence non-smooth and fast-changing FF control signals may lead to worse performance compared to a slower and smoother control signal. The reference filter was returned to give smooth reference signals similar to what is seen in Aurlien (2020).
- Simulation must be updated due to control system updates.

5.3 Tuning the System

The two parts of the adaptive control system that need to be tuned are:

1. The number of principal components input for the SIMPLS regression algorithm.
2. The length of the window used in the smoothing of $\boldsymbol{\nu}$ for surge sway and yaw.

5.3.1 Tuning Number of Principal Components

To tune the number of principal components, the parameter in the SIMPLS algorithm was varied while keeping the training and test-set constant. Since the smoothing window length might impact the quality of the analysis, tests for different window lengths must be done. The MSE of the lack-of-fit residual is used to compare and evaluate the models. Results indicate that 12 principal components are the optimal choice and will perform well for all window lengths.

5.3.2 Tuning the Smoothing Window Length

Tuning of the smoothing window length was done with a data set from Experiment 1, and where different smoothing windows on this data set were used. This means that training data is varied in the post process, while still being based on the same original data set. Since the controller has not used these different models in experiments, evaluating the performance can only be done from a modeling perspective. That is, how the lack-of-fit residual will turn out to be. However, if the model correctly predicts the observed dynamics, the DP system should perform well.

The different models are evaluated on a test set from Experiment 2 using smoothing of 1 second. Smoothing the data set is needed because the variance of the force prediction signal will vary depending on how much smoothing is used in the training set. The noise in the predicted actuator force that occurs due to noisy measurements is no problem in itself, since the data is from a test set and because only smooth reference values are used as model input in the DP system. It is, however, difficult to compare the models by using the MSE of the lack-of-fit residual. The impact of smoothing the training set is shown in

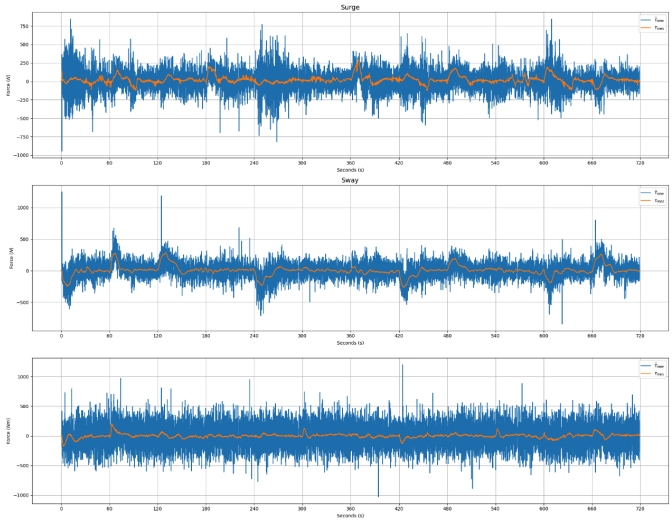

(a) Training-set with smoothing window of $0.5\ s$.

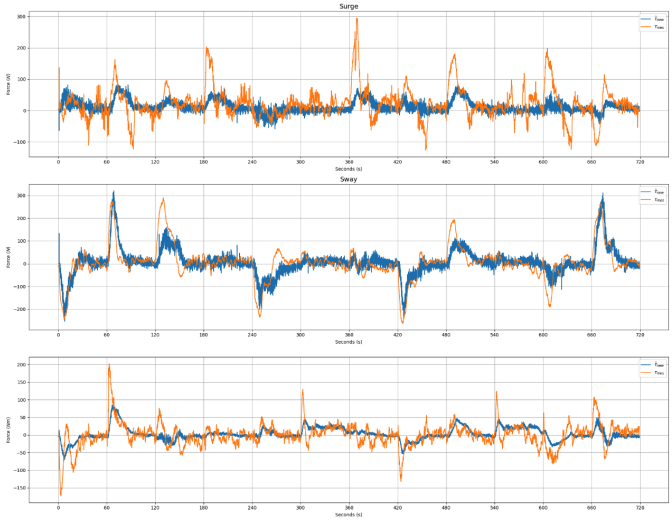

(b) Training-set with smoothing window of $0.0\ s$.

Figure 5.1: Impact on the predicted applied force when smoothing the training-set. The test-set is not smoothed. Here, $\hat{\boldsymbol{\tau}}_{new}$ uses the obtained model.

Figure 5.1. Using a smoothed test-set eliminated this effect, as seen in Figure 5.2. The performance metrics used to evaluate the models are also here the MSE of the lack-of-fit residual. By comparing the different models, a smoothing window of 1 second resulted in the lowest MSE for both surge, sway, and yaw. The training set was smoothed with windows of $0.0, 0.25, 0.5, 1.0$, and 1.5 seconds, resulting in 5 different models.

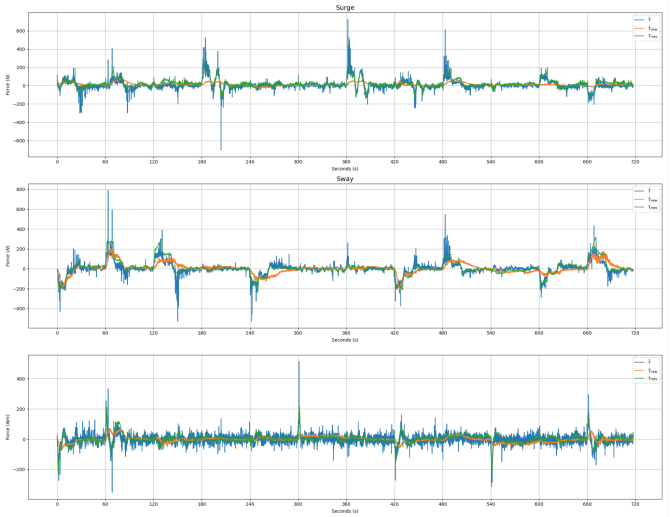

(a) Training-set with smoothing window of $1.5\ s$.

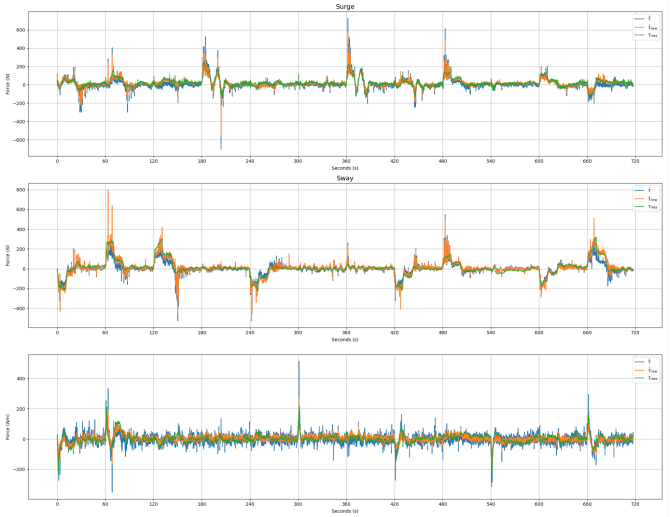

(b) Training-set with smoothing window of $0.0\ s$.

Figure 5.2: Impact on the predicted applied force when smoothing the test-set. The test-set is smoothed with a window of $1.0\ s$. Here, $\hat{\boldsymbol{\tau}}_{new}$ uses the obtained model and $\hat{\boldsymbol{\tau}}$ uses the Master Model.

5.4 Extended Simulation Results

In the simulation, no external wind is generated, but the wind resistance due to the movement itself is included. Measurement noise is included and modeled as white Gaussian noise (WGN) with standard deviations according to Table 5.2. Since the environmental

Table 5.2: Standard deviation of measurement processes, by courtesy of Brage (2019).

States	Standard deviation
x	0.02 m
y	0.02 m
ψ	0.2 deg
u	0.05 m/s
v	0.05 m/s
r	0.2 deg/s
$\dot{u}$	0.01 m/s^2
$\dot{v}$	0.01 m/s^2
$\dot{r}$	0.1 deg/s^2

disturbances are lower in simulations than in experiments, a smoothing window of 0.25 seconds turns out to be the optimal smoothing window length. As seen in Figure 5.3, the adaptive system works as intended, and the performance metrics improve for every new model update. The system uses two rounds of training before the model converges.

Due to a slightly inaccurate simulator, the comparison to the control system initiated with the simulation model is inaccurate. Inaccuracies occur because the simulated rigid body dynamics do not correspond to the simulated rigid body model, but this does not impact the qualitative performance of the adaptive control system. The simulations done in Aurlien (2020) are more accurate in regards to dynamics and external disturbances and better reflect the robustness and potential of the system. The lack of thruster dynamics in the simulations by Aurlien (2020) is not relevant in regards to the MVA. The simulations introduced in this thesis are, however, done with the same software as used in the experiments and verifies that the system is implemented correctly.

5.5 Experimental Results

This section shows the results of the experiments performed to test the adaptive control system and the novel carrot-based steering law for path following. The test setup for the adaptive control system is explained in detail in 4.3 and 4.5. Procedures regarding safety precautions and practical execution of the experiments are included as Appendix C. For Experiments 1 and 2, the control system initiates the base model with Pedersen's (2019) parameters and uses $\delta = \sigma = 0.4$ and $\zeta = 1$, to ensure that the system can improve. For Experiment 3 the control system is initiated with Pedersen's (2019) parameters and uses $\delta = \sigma = \zeta = 1 = 1$. An overview of all different rounds, different data sets, and obtained models from Experiments 1, 2, and 3, is listed in Table 5.3.

5.5.1 Experiment 1: Performance In Windy Conditions

In the preparations for Experiment 1, a strategy was developed to tune the smoothing filter without performing new experiments. The tuning of the reference filter dynamics was also

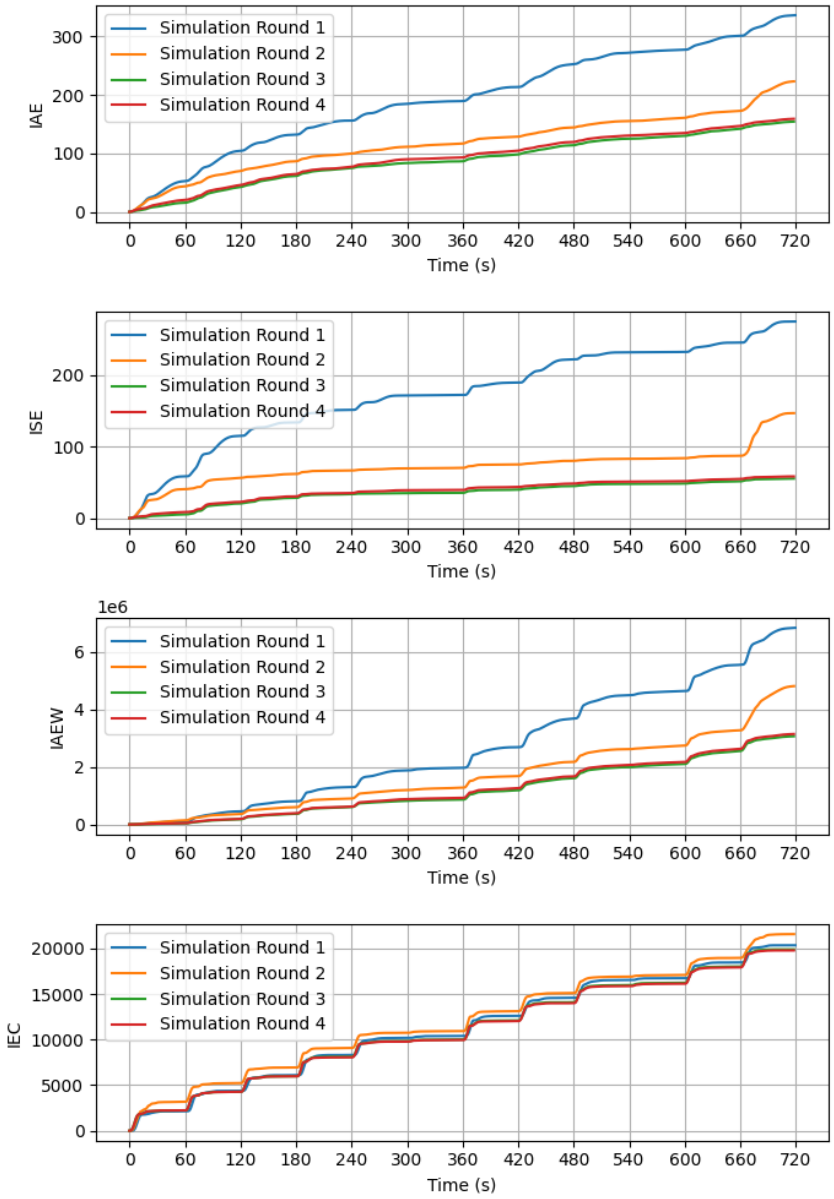

Figure 5.3: Metric comparison related to model accuracy.

fixed to ensure that the control signal was easier for the actuators to realize. Initiating the system with a scaled version of the current model of milliAmpere was a practical decision made to show that the adaption mechanism of the controller works in case the Master Model is close to the optimal model. An additional test is than needed to test

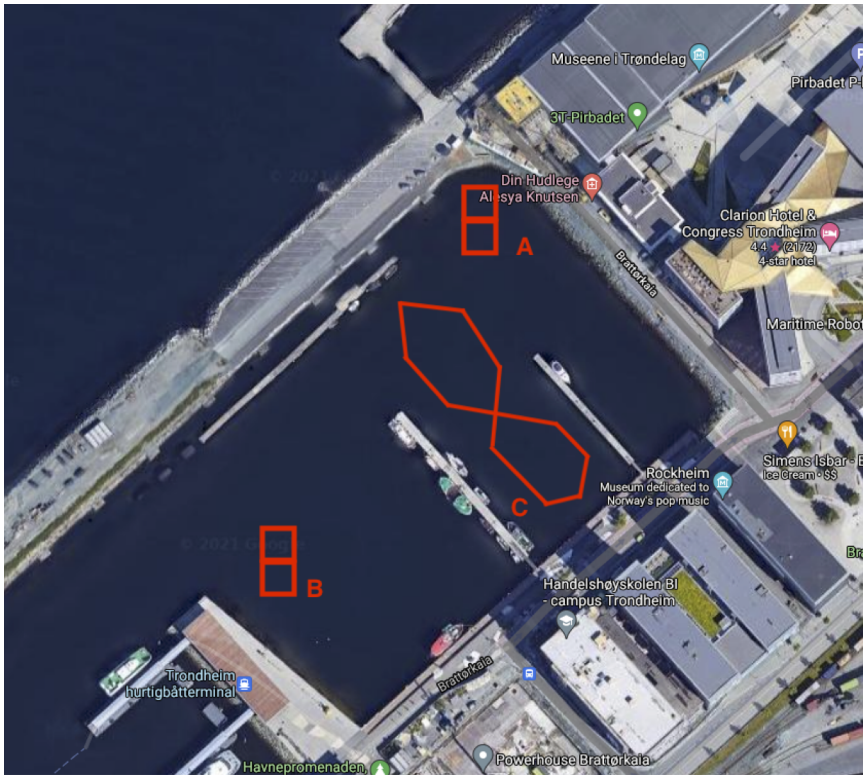

Figure 5.4: Location of the experiments from Experiment 1 (A), Experiment 2 (B), and Experiment 3 (C).

the performance of the current model of milliAmpere. The weather conditions during Experiment 1 were dominated by strong winds. According to the weather forecast, the wind came from the NW direction and with speeds of 6 m/s and gusts up to 10 m/s. Because of the molo, extending roughly 1.5 meters, and shielding buildings, winds were estimated to range from 0 to 10 m/s depending on time and location in the path. The location of the test leads to negligible wave disturbances. The goals of Experiment 1 can be summarized as:

- Testing the system performance with improved tuning of the reference filter.
- Testing the system performance with improved adaptive tuning.
- Testing the system performance in strong winds.

Performance

The adaptive controller improves the precision and lowers the energy consumption as the models are trained with larger data sets, as shown in Figure 5.5. The improvement from Round 2 to Round 3 is, however, small, and from all earlier experiments, the performance

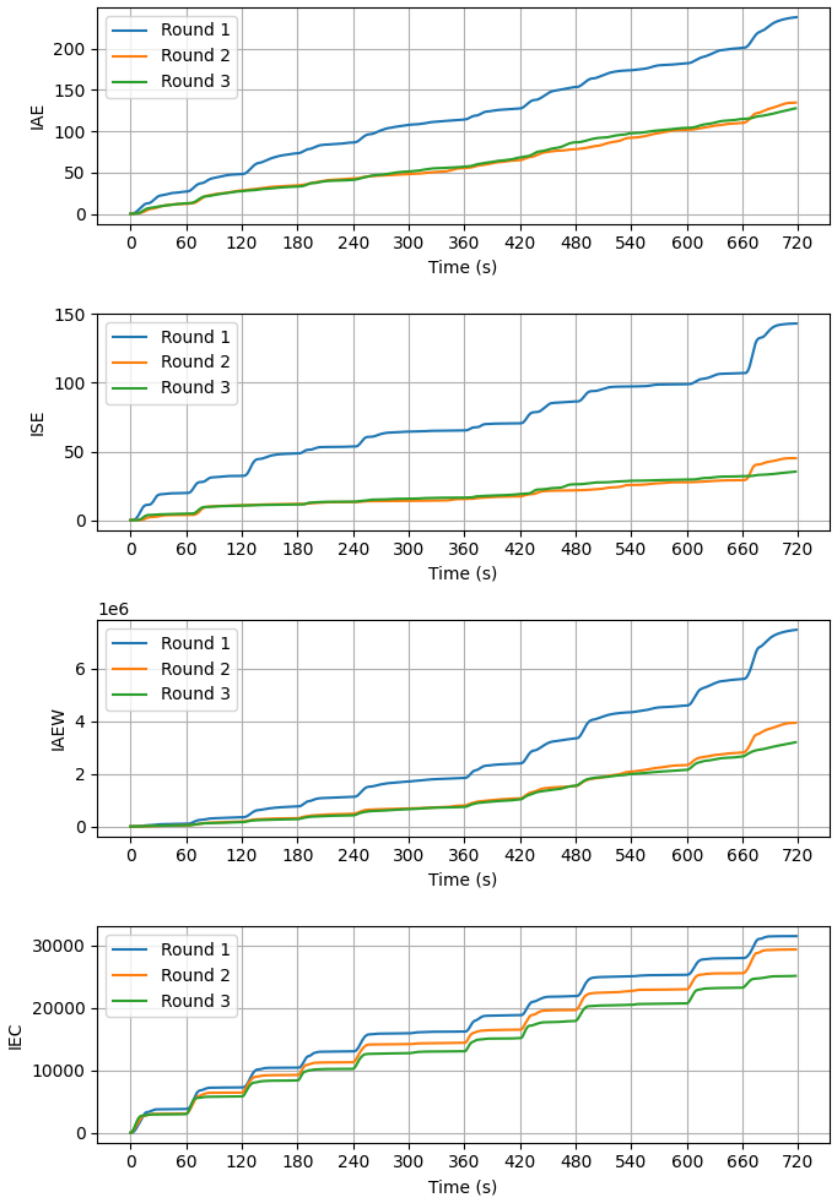

Figure 5.5: Performance metrics for Experiment 1.

has converged within two rounds of training, which indicates that it is unlikely that Model 3 would lead to further improvements.

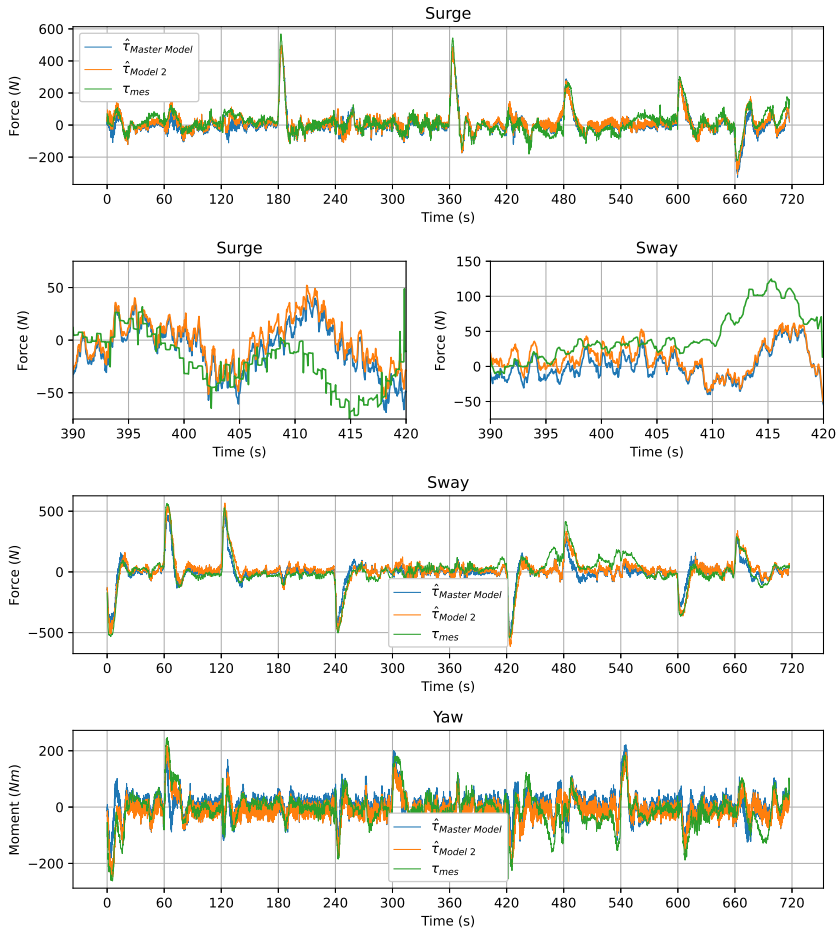

Figure 5.6: Model fit for the Master Model and Model 2.

Model Fit

The model fit of Model 2 and the Master Model on Data Set 3 is shown in Figure 5.6 with additional zoomed-in sections of surge and sway. Here, $\boldsymbol{\tau}_{mes}$ is the actual applied actuator force, and $\hat{\boldsymbol{\tau}}$ is the predicted applied actuator force using the model specified by the subscript. If the MSE of the lack-of-fit residual is used to compare the two models, Model 2 performs 84%, 87%, and 68% better than the Master Model for surge, sway, and yaw respectively.

Even though Model 2 reduces the MSE of the lack-of-fit residual significantly compared to the Master Model, Model 2 still does not fully manage to estimate the applied force correctly. Since wind is not measured, and therefore not a part of the MVA, Model 2 has no understanding of the wind impact and can not separate it from the applied actuator

Table 5.3: Overview of the data sets used in different models. Rounds 1-3 are from Experiment 1, Rounds 4-8 are from Experiment 2, and Rounds 9-11 are from Experiment 3. Master Model refers to the current model of milliAmpere, which is Pedersen's (2019) model with $\delta = \sigma = 1$ and $\zeta = 1$.

Round	Model Used	Data Set Created	Model Created	Data Source
Round 1	Base Model	Data Set 1	Model 1	Data Set 1
Round 2	Model 1	Data Set 2	Model 2	Data Sets 1-2
Round 3	Model 2	Data Set 3	Model 3	Data Sets 1-3
Round 4	Base Model	Data Set 4	Model 4	Data Set 4
Round 5	Model 4	Data Set 5	Model 5	Data Sets 4-5
Round 6	Model 5	Data Set 6	Model 6	Data Sets 4-6
Round 7	Model 6	Data Set 7	Model 7	Data Sets 4-7
Round 8	Master Model	Data Set 8	Model 8	Data Set 8
Round 9	Master Model	Data Set 9	Model 9	Data Set 9
Round 10	Master Model	Data Set 10	Model 10	Data Sets 9-10
Round 11	Model 10	Data Set 11	Model 11	Data Sets 9-11

force. Because the force impact can not be separated, deviation in the lack-of-fit residual occurs. The model only observes the resulting movement and connects it to actuator forces. If a wind gust from NW pushes the vessel off its trajectory, the FB ideally reacts with an equal and opposite force to counteract the wind impact. Because of the nature of a FB being error-driven and not managing to act momentarily, the vessel is accelerating in the SE direction while an actuator force is applied in the NW direction. The model will naturally believe that the movement in the SE direction is caused by an actuator force in the SE direction, but in reality, the actuator force applies the force in the opposite direction to neutralize this undesired movement. This shows the weakness of not including measurements of the known impacting environmental forces.

This is observed in the deviations in Figure 5.6. The deviations fit a natural compensating force of the wind impact from NW. In the time period between $t = 390$ and $t = 420$ of the calibration pattern, the vessel's heading is $\psi = 180$, and it tries to keep its pose. At $t = 405$, a wind gust from the NW hits the vessel. The estimates and applied force fit the description that the vessel's movement and the applied force are initially in the opposite directions. Shortly after, the FB controller manages to take control of the ground movement in the desired direction and lead the vessel back to the desired trajectory.

Currents can also cause the estimate of the applied force to deviate from the measured force. Currents cause the ground movement to deviate from the relative water movement, which is problematic when all state measurements are relative to ground. If the current speed is equal, but in opposite direction to the vessel speed, the vessel will stay still relative to ground. Without measuring the current, the model's best guess is to assume that no force is applied.

It is expected to see unmodeled dynamics in the model fit due to the lack of wind and current measurements and modeling. It is therefore a good sign that the system still manages

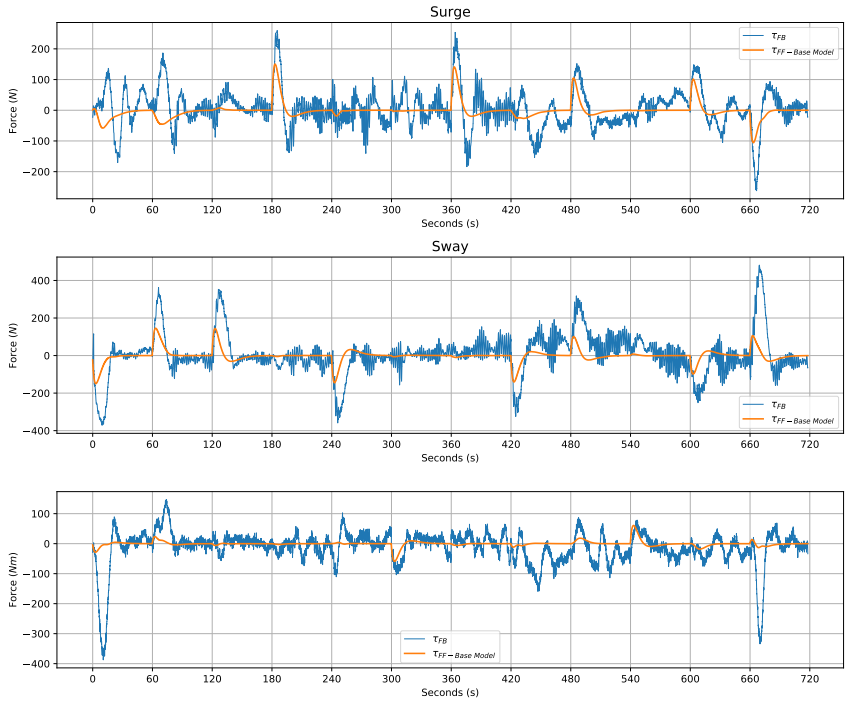

Figure 5.7: Experiment 1: The FF and FB contribution to the control signal Round 1, using the Base Model.

to obtain a good model that explains the rest of the components in the lack-of-fit residual. This indicates that the adaptive system is well-tuned so that the lack-of-fit residual is not over-fitted. However, the model does contain a small bias in yaw due to the symmetry of milliAmpere. When milliAmpere turns 180 degrees, the wind impact is still trying to rotate the vessel in the same direction, while the surge and sway biases are canceled out, due to the more balances data set of head, side, and tail wind. The conditions are stable enough for the adaptive model to outperform the Master Model also for sway, but would probably not be the case for sway, if tested with a data set from calmer conditions.

Shift from FB to FF Control

The FF and FB control signals from Round 1 is shown in Figure 5.7. The corresponding data for Round 3 is shown in Figure 5.8. Finding and comparing the power of the FB control signal $\boldsymbol{\tau}_{FB}$ from Round 1 and Round 3 tells us whether the adaptive control system successfully transfers more of the control response from FB to FF control. From Round 1 to Round 3, the power is reduced by 39%, 61%, and 51% for the surge, sway, and yaw components, respectively. An easy place to spot the difference between the two figures is in surge at $t = 240$ to $t = 300$. In Figure 5.7 it can be seen that the FB controller drives most of the actuator force. In Figure 5.8, however, the FB control signal is much

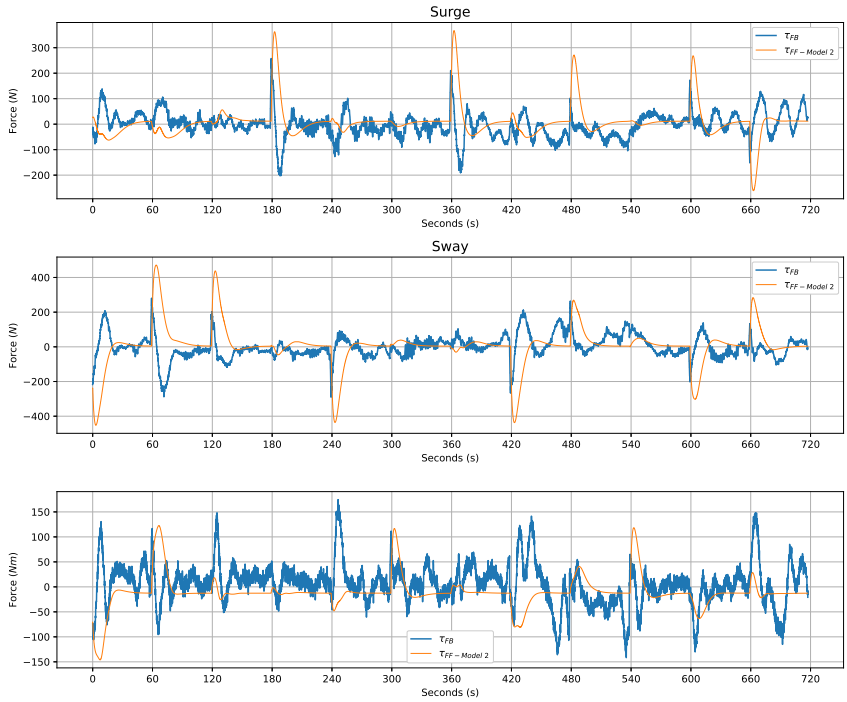

Figure 5.8: Experiment 1: The FF and FB contribution to the control signal Round 3, using Model 2.

lower in the period where the FF is active. A common trend seen in Figure 5.8 is that the FB control signal spikes when the FF control signal activates when new waypoints are set. This is probably due to the delay and dynamics of the actuators that make it difficult to apply the desired force instantly. Because of the actuator delay, an error is observed, and the FB control signal makes correcting adjustments. Strong winds in both Round 1 and Round 3 increase the need for FB adjustments, especially in yaw. This is expected considering milliAmpere's low moment of inertia in yaw.

5.5.2 Experiment 2: Performance in Windy and Wavy Conditions

The original goal for Experiment 2 was to re-test the adaptive system under ideal weather conditions and to compare the performance when using the adaptive model and Pedersen's (2019) model. However, the winds were also significant during Experiment 2, even though they were lighter than during Experiment 1. In addition, the waves were also significant during Experiment 2. This made Experiment 2 rather focus on how robust the system is, and how the adaptive system handles wave disturbances in addition to wind. The goals for Experiment 2 can be summarized as:

- Analysing how the adaptive control system performs compared to the current control

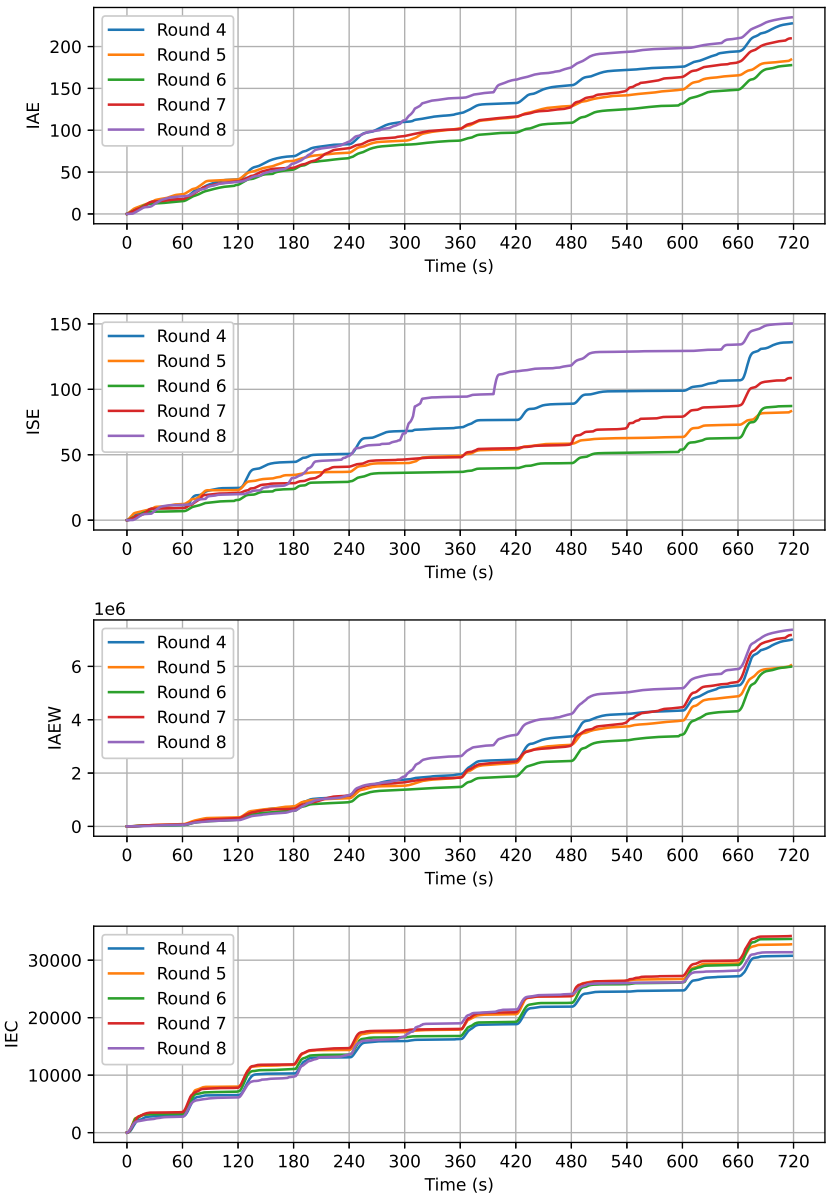

Figure 5.9: Experiment 2: Performance metrics.

system on milliAmpere.

- Analysing how robust the system is in regards to wave disturbances in addition to wind.

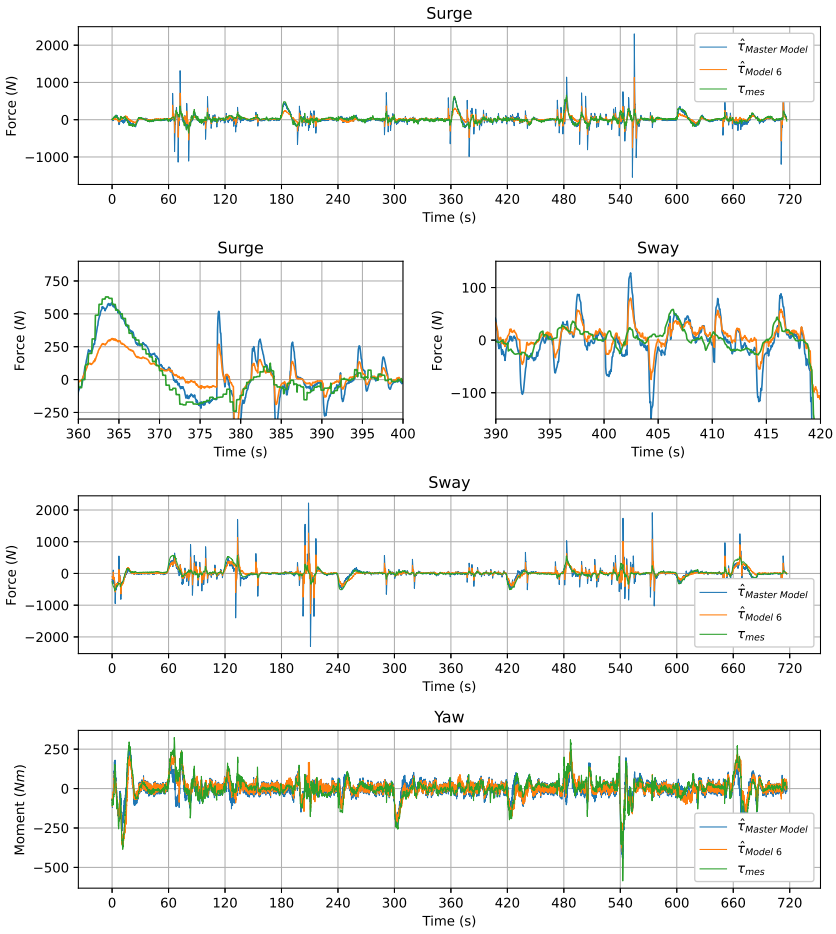

Figure 5.10: Experiment 2: Model fit for Model 6 and the Master Model on Data Set 7.

During Experiment 2, the wind speed was around 3 m/s from NE, which is considered a light breeze according to the Buford scale (Beaufort, 1805). The wind was relatively stable and little to no gusts.

System Performance

The performance of the system is shown in Figure 5.9. The system does not nearly perform as well as in Experiment 1. The performance in Round 4 is worse than the performance in Round 2 and Round 3, both for precision and energy usage.

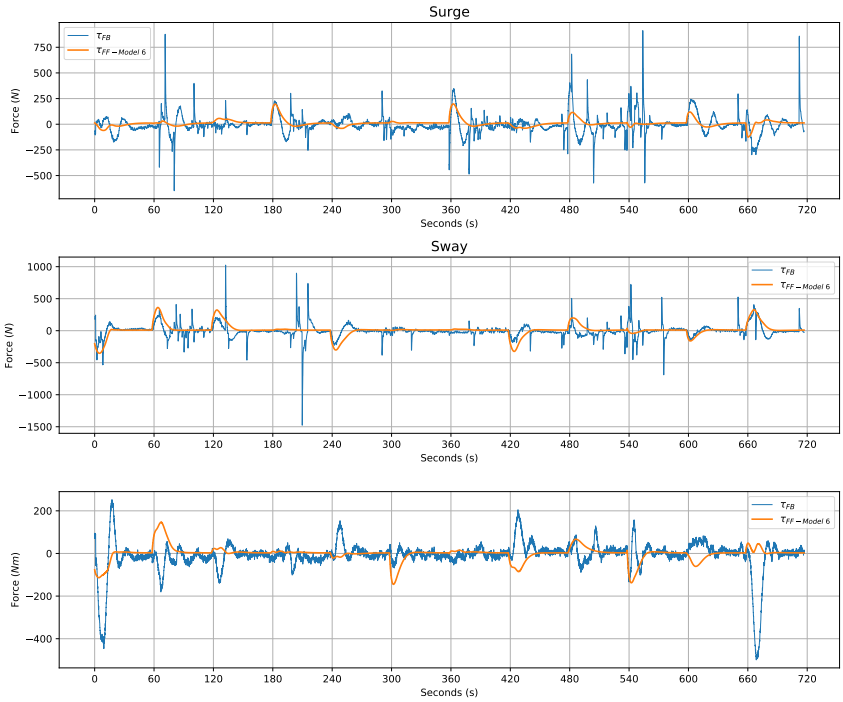

Figure 5.11: FB and FF control signal for Round 7, using Model 6.

Model Fit

In Figure 5.10, Model 6 and the Master Model are tested on Data Set 7. At $t = 365$ in surge, Model 6 struggles to match the precision of Model Master. Model 6 is, however, closer in the spikes that occur due to wave disturbances, as seen in the sway from $t = 400$ to $t = 420$. This behavior is not unexpected because the unknown external force disturbance from the waves is much greater than the force disturbance from the wind, which makes Data Sets 4-6 much harder to fit accurately.

Wave Impact

The FB control signal from Round 7 shown in Figure 5.11 makes corrections up to $1500N$. Similar plots from Rounds 4-6 reveal several instances of correction of at least $600N$ and up to $1000N$ in the FB control signal. These kinds of adjustments are never seen in the data from Experiment 1, where FB control signals in its peaks lie between $100N$ to $200N$ for all rounds. The FB control signal is not the real applied force and will be smoothed out when realized because of the thruster dynamics, but the control signal can still be used to indicate the impact of the disturbances.

The wave's impact on the vessel's movements from Round 8 can be seen Figure 5.15, and corresponds with the timing of the FB control signal spikes in Figure 5.13. It is also at

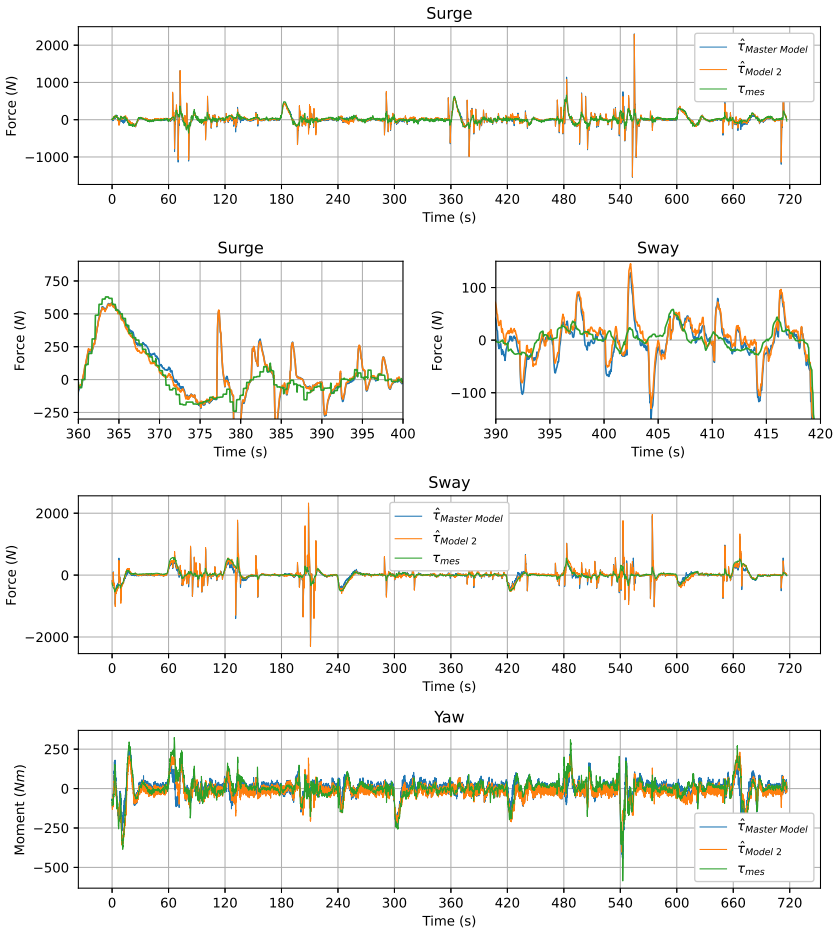

Figure 5.12: Experiment 2: Model fit for Model 2 on Data Set 7.

these time instances that the biggest steps in the performance metrics from Round 8 in Figure 5.9 occur. The wave disturbance makes a significant impact on the performance metrics, and variations in the waves from round to round explain why the precision in Round 7 is worse than in Round 6.

Reasons for the Waves

The difference in the wave disturbance between Experiments 1 and 2 is primarily due to the test location and external interference. The biggest waves occur because of other vessels passing by. There will be more time for the waves to build up further away from the molo. Considering the wind directions from NE and the location of the tests as seen in Figure 5.4, it is reasonable to believe that the general wave disturbance was more signifi-

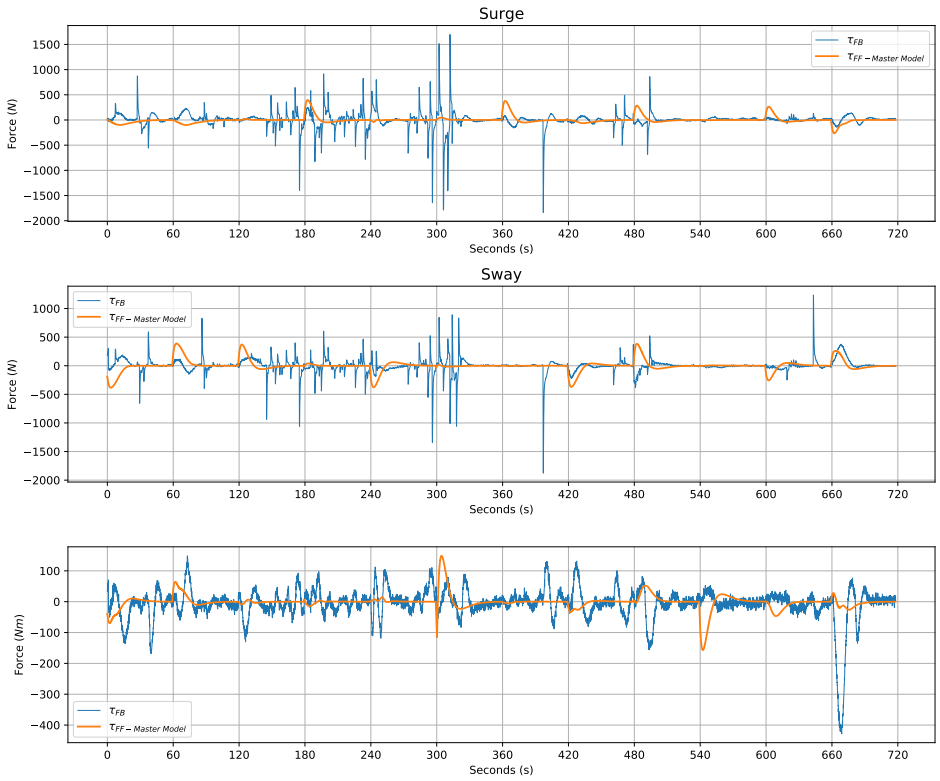

Figure 5.13: Experiment 2: Wave impact on FB control signal from Round 8.

cant during Experiment 2 compared to Experiment 1, even though the winds were lighter. This fits with the experienced disturbances onboard during the Experiments, the observed FB adjustments, and the model error observed in Figure 5.10.

Waves Cause Bad Models

The adaptive models in Experiment 2 also contribute to the bad performance. The FB and FF control signals from Round 7 where Model 6 is used is shown in Figure 5.11. Compared to the FF and FB usage from Round 3 where Model 2 is used, it can be seen that Model 6 does not manage to shift the FB control into FF control to the same degree as with Model 2. In Figure 5.14 a direct comparison between the FF control signals from Rounds 3 and 7 is shown. It can be seen that the FF signal is not as aggressive in Round 7 compared to Round 3 which reflects the needed FB in Figure 5.11.

A comparison between Model 4 and Model 8 reveals how much the wave disturbances impact the resulting model. Round 4 and Round 8 are impacted by small waves and big waves, respectively, which makes it interesting to analyze the properties of Model 4 versus Model 8. Testing Model 4 versus Model 8 on Data Set 7 shows that Model 8 scores poorly

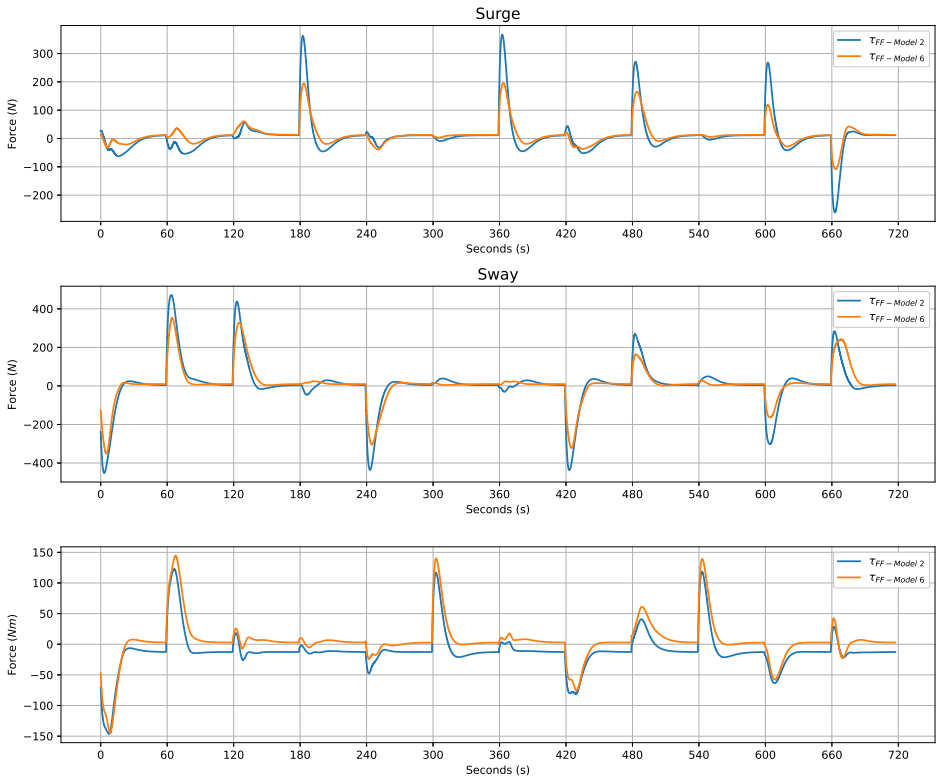

Figure 5.14: Direct comparison of FF control signal generated with Models 2 and 6 from reference signals in Data Set 3.

with a MSE of the lack-of-fit residual that is 217%, 171%, and 58% worse than Model 4 for surge, sway, and yaw respectively. This indicates that the waves' disturbance can break the model and is not easily filtered out.

Using the MSE to check the model precision of Models 2 and 6 on Data Set 7, Model 6 scores better. The model fits are shown in Figure 5.12 and Figure 5.10 respectively. The MSE of the lack-of-fit residual is used to evaluate models and predict which model leads to the best performance. Low MSE should give good performance. However, this contradicts the observed behavior of Model 2 and Model 6, where Model 2 used less FB control. This is a result of the lack of wave modeling. As earlier explained, the models can not separate unmodeled external forces from the applied actuator force. When obtaining a model without wave dynamics, the wanted lack-of-fit residual is what is seen in Figure 5.12. In the calibration pattern at $t = 360$, the vessel starts to move in the surge direction towards the South. In the beginning, the Master Model and Model 2 accurately estimate the applied force, indicating that the wave disturbance at this point is not significant. From $t = 375$ to $t = 420$, the greater impact by the waves is observed, reflected by the differences in the estimate and measured applied force.

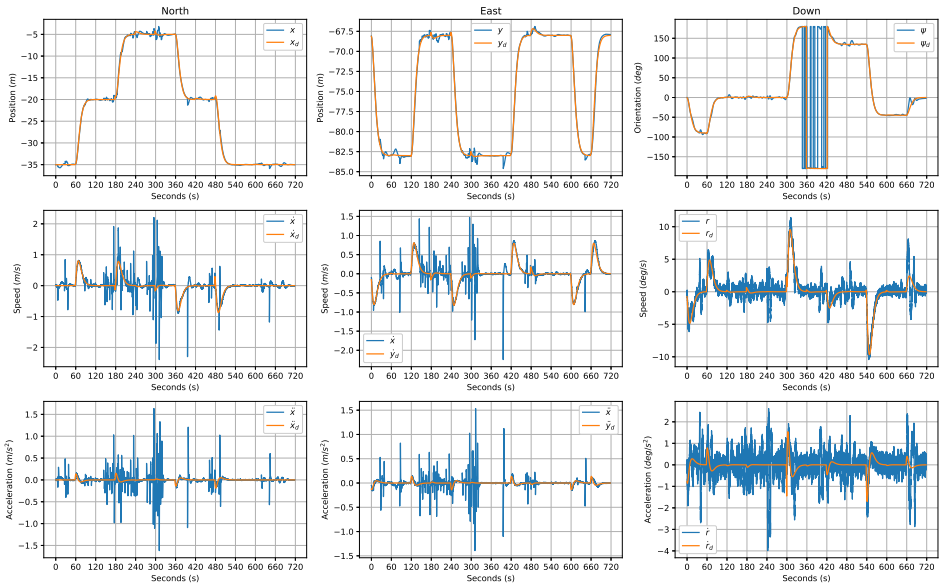

Figure 5.15: Experiment 2: Wave impact on the vessel states from the master round.

Due to Models 4-6 being trained to minimize lack-of-fit residuals containing big wave components, the best fitting model is not necessarily the model that performs the best. In Figure 5.10 it is seen that the dampening of the spikes in surge and sway comes with the price of imprecise estimates around $t = 360$, where it should be precise. Since the waves are of such a big impact, Models 4-6 have learned that acceleration and applied motor force are not as tightly correlated as in reality, leading to bad fit in surge between $t = 360$ to $t = 375$. Reflecting back to the corresponding situation from Experiment 1, the correct model leads to the best overall fit. Trying to over-fit the small wave components would have caused too big misfits for the rest of the data set; hence the wave impact was correctly filtered out. In Experiment 1, the better MSE for Model 6 compared to the Master Model was actual model improvements and not wind over-fitting, since the Master Model does not outperform Model 6 at any location in the model fit. This is especially clear in Figure 5.6 in surge at $t = 600$ and $t = 660$.

The over-fitting of wave components points out a weakness of the adaptive system. Trying to fit an insufficient model of the lack-of-fit residual, might cause the adaptive system to wrongly update the model when not desired. Small force disturbances like wind are handled, but if the impact is too significant, as wave forces are, the system will struggle to obtain the optimal model.

5.5.3 Experiment 3: Testing the Carrot-based Steering Law

Additionally, on the day of the Pilot Tests Day 2, the carrot-based steering law was tested on an operational path similar to the operation path described in Aurlien (2020) but with

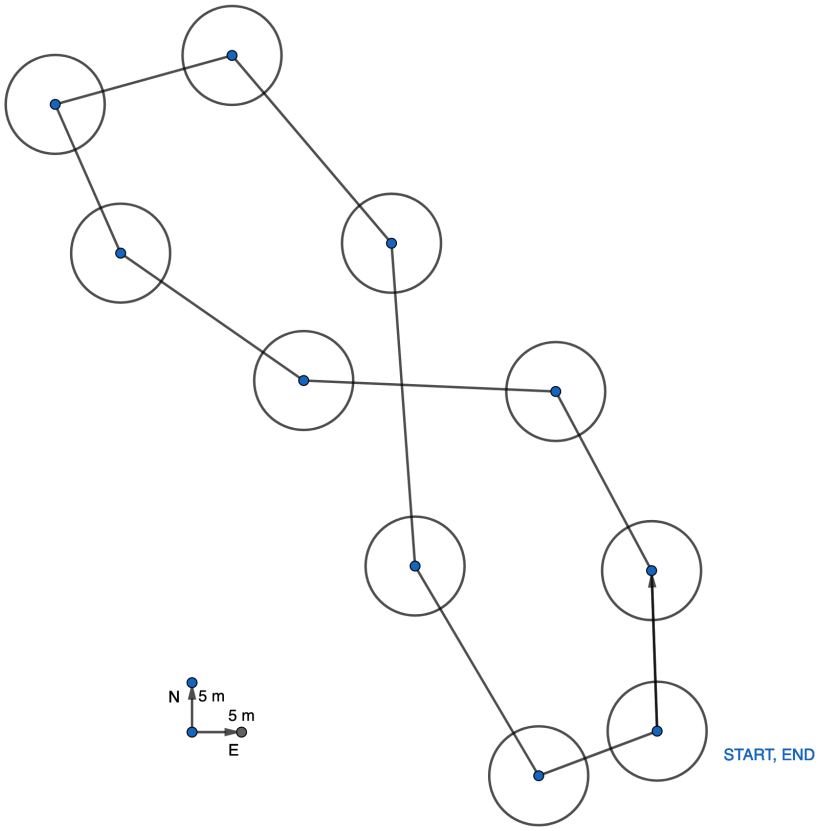

Figure 5.16: Experiment 3: Operation path.

waypoints that were chosen from a manual run. The desired path created is shown in Figure 5.16, where the switching radius circles of $5\ m$ are also illustrated. For Experiment 3, rounds are referred to as 12 minutes of path following. By chance, this fits quite good with a complete cycle of the operational path.

For Experiment 3, in addition to test the carrot-based steering law for 24 minutes using the Master Model, the adaptive controller was also tested. Using Data Sets 9-10, Model 10 was obtained and given to the DP system for Round 11. The adaptive tuning was not optimal, using a smoothing window of 1.5 seconds for the acceleration estimates, and 17 principal components in the SIMPLS algorithm.

The body and NED responses from Round 10 are shown in Figure 5.17 and Figure 5.18 respectively. Looking closer at for example $t = 60$ in Figure 5.17 verifies that the speed slows down while turning, before the vessel accelerates when exiting the turn. Similar results can be seen around $t = 180$, when the vessel is in the north end of the path and two quick waypoint changes occur.

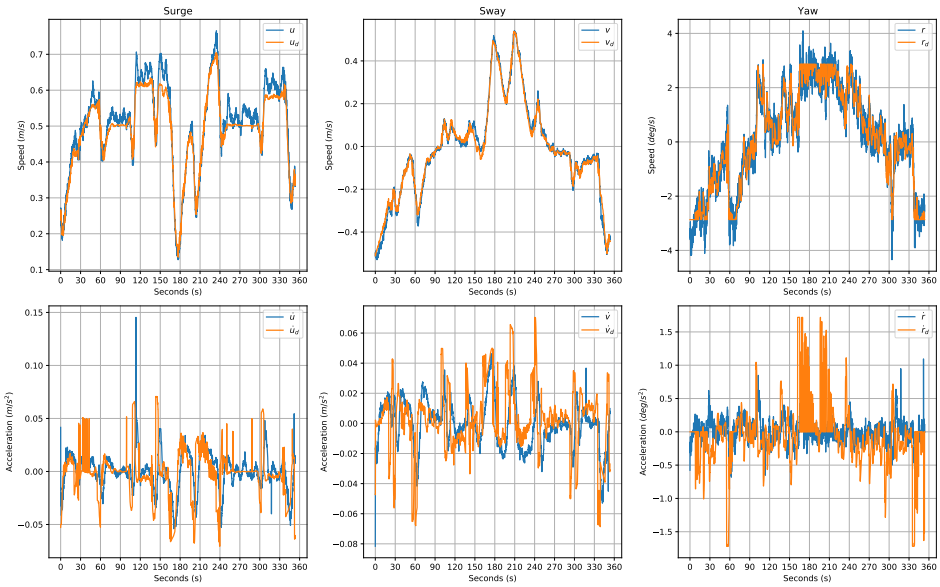

Figure 5.17: Experiment 3: Response in body for Round 10.

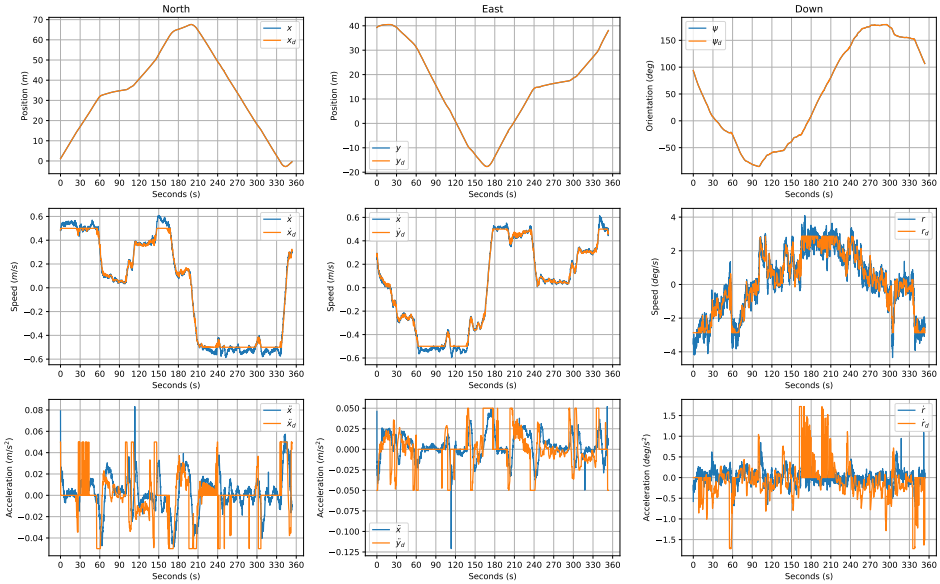

Figure 5.18: Experiment 3: Response in NED for Round 10.

The results prove that the carrot-based steering law performs according to the design criteria, reducing the speed when entering a turn and accelerating when exiting.

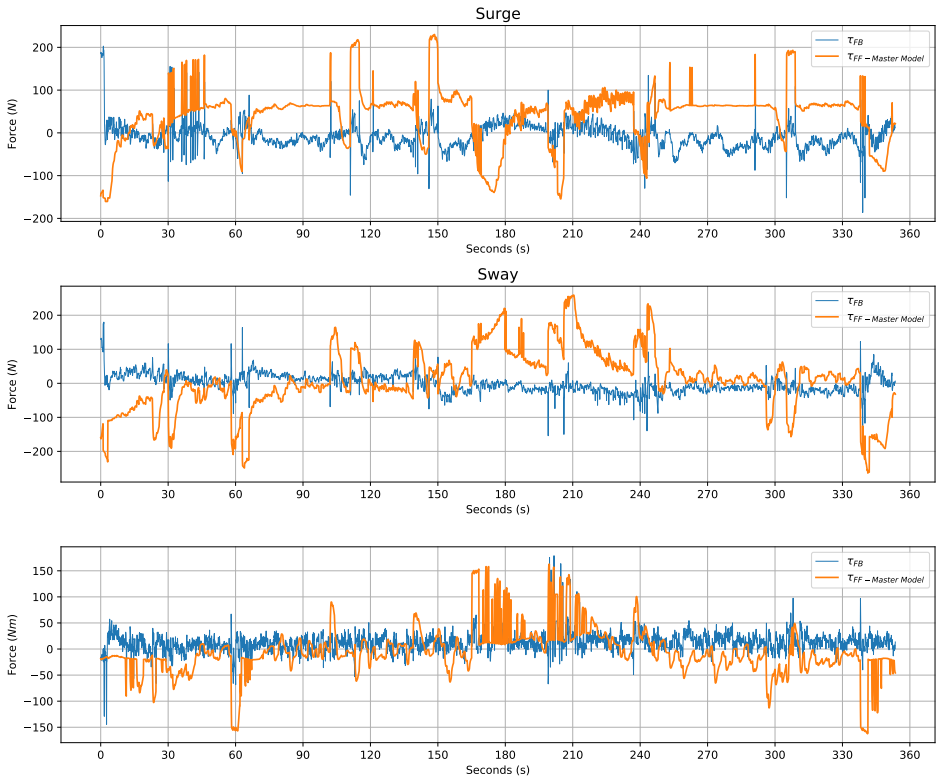

Figure 5.19: Experiment 3: FB and FF control signal for Round 10.

The FB and FF control signals for Round 10 are shown in Figure 5.19. As discussed previously, the reference filter from pilot tests day 2 was not properly tuned, which also is the case for Experiment 3. The FF control signal is therefore quite sharp, leading to some spikes in the FB control signal. Ignoring this factor, the FB control signal is relatively small, indicating that the path following is FF driven.

The FB and FF control signals for Round 11 are shown in Figure 5.20. It is difficult to notice any significant change in the FB usage between Round 10 and 11 indicating that the adaptive model is doing well.

5.6 Discussion

This section covers an in-depth discussion of the experimental results.

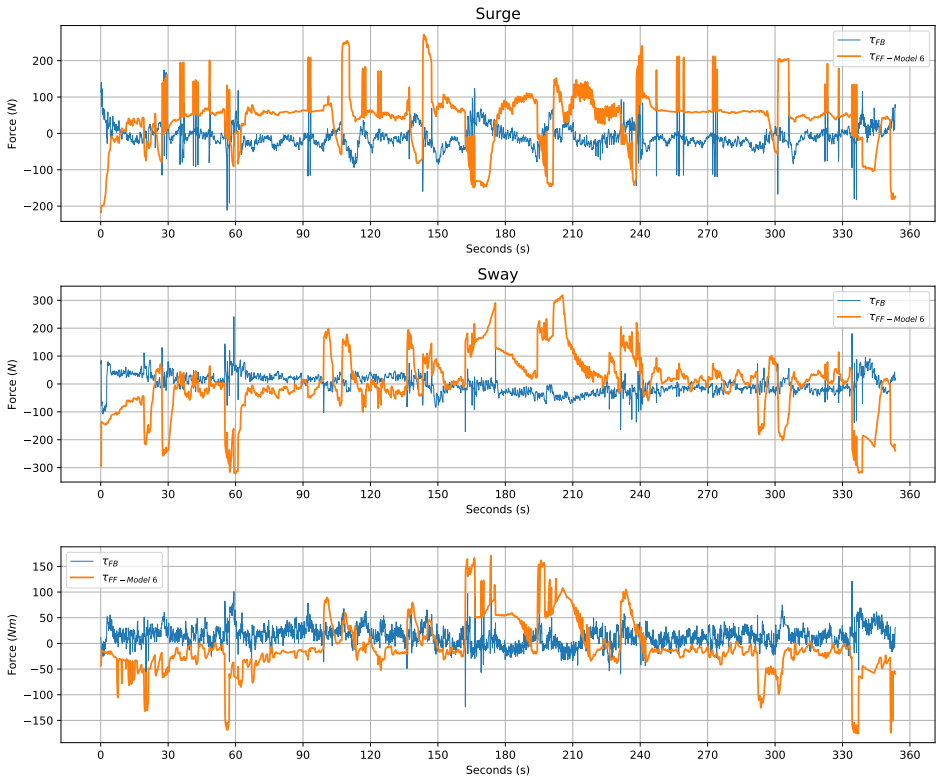

Figure 5.20: Experiment 3: FB and FF control signal for Round 11.

5.6.1 Solving Practical Issues

Before the Experiments could start, some practical issues needed to be solved. First of all, the system needed to be moved from the simulator into a real environment, which limited the sensors and signals that were available to work with. This gave complications with the thruster dynamics and the acceleration measurements. The navigation system of milliAmpere did not include estimation of the body acceleration, which was crucial for the adaptive system to function. Exploring several different solutions lead to the smoothing technique, which proved to be successful. Without going back and forth between the pilot tests and further analysis of the system, the final system would never be realized. The pilot tests made it possible to tune the system under real conditions that were different from what could be simulated.

5.6.2 Experimental Performance

The experimental results show that the adaptive control system works and improves precision during the tests. Even in the presence of wind disturbances, the adaptive system manages to find a precise model that even beats the current model of milliAmpere, which

indicates that the adaptive system is well-tuned.

The high use of the FF control in Experiment 3 proves the carrot-based steering law to be a success. The development of this steering law is crucial to take full advantage of the adaptive control system for path following purposes, since the similar enclosure-based FF approach can not fully be relied on.

5.6.3 Many New Possibilities

The development of this new approach to adaptive controllers for marine vessels opens many new possibilities. First of all, it can be used to quickly and accurately make models for all different kinds of ships, without being dependent on small-scale models in wind tunnels to estimate the model parameters. Secondly, since the system is continuously running, the system can detect and adapt to changing dynamics. Because the system is flexible, the best fitting model will quickly be found, leading to fuel savings due to more precise and optimal applied forces. Thirdly, a more precise and reliable control system gives higher trust and robustness, increasing safety onboard the vessel.

Additionally, the adaptive model is flexible and can easily be extended to model wind and current, leading to even better performance. This support can easily be added to milliAmpere by adding an anemometer below the hull and on top of the roof. Wave modeling has not been inspected closely, but since roll and pitch are exclusively related to waves, assuming centered and non-moving load, and the actuators can not control these degrees of freedom significantly, the wave disturbance could potentially be modeled indirectly by a 5-DOF model. The pitch and roll measurements would then give information on how big the waves are and correspondingly how big force the wave impact makes.

5.6.4 Proof-of-concept Simplifications

The experiments in this thesis show the proof of concept on this new approach to adaptive control systems for marine vessels. Many simplifications have been done, revealing possibilities for further improving the system. The basis functions used, are based on 2. order modulus functions for an uncoupled 3-DOF model that the MVA does not limit to only be used in their intended dimension. This leads to somewhat odd models. The basis function u is for example not necessarily weighted by zero in sway and yaw, even though the basis functions chosen, suggest that the system tries to model a decoupled model.

Adjusting the basis functions to more complicated models is easy to do and should be tested in further work. Models that can be tested are a 2. order modulus functions for a fully coupled system and the 4-DOF model based on nonlinear model based on low-Aspect ratio wing theory by Ross et al. (2007). A 4-DOF or even 5-DOF model is interesting to investigate further for possibilities regarding wave modeling.

5.6.5 Aspects Concerning the Success for Operational Use

Results from Experiment 2 show that the system is vulnerable to wave disturbances that can break the analysis resulting in a bad model. If the wave issues can not be solved, an

important topic is whether the adaptive control system is best used for model identification or if it still can be robust enough to be used in operations. The success of the adaptive system in operations also depends on what the goal of the adaptive controller is. Some different goals could be:

- Detect model changes due to passenger and cargo load
- Detect model changes due to bulks in the hull
- Detect model changes due to moss and algae

Importance of PE Data Sets

The success of these goals boils down to whether the data-set is PE and disturbance-free. Say it is found a way to extend the model to include wave impact or find a way to disregard data that includes wave disturbance. If the goal is to adjust the model to passenger load, there is not much time to obtain a model if the system should take advantage of the model before the passengers leave the ferry. The challenge here is to get a rich enough signal to fit a new model properly. Detecting slower changing dynamics such as bulks, moss, and algae are easily detected since the data-set can stretch over a larger time span without problems. For these dynamics, it is sufficient to update the model, for example, once every week.

A potential issue is that test sets also need to be based on the new conditions. Say the passenger and cargo load modeling is addressed, and data is collected from the quay to half across the channel. This data must be split into a training and test set if the updating criterion is implemented according to Section 3.2.4. The model might perform better in the test set, but a concern is that once new unseen maneuvers are done, the FF controller might do strange things because the training data is only based on surge movement. There is a famous saying by Aristotle, ”For the things we have to learn before we can do them, we learn by doing them.” which is quite relevant here. The system can not be expected to perform well in situations it has not been trained for, and relates to the PE issue.

When new models are created, the system forgets everything it has learned in the past if the new dynamics should be detected accurately. If the data set is not PE, the extra maneuvers needed to ensure the PE data set quickly exceeds the potential fuel save by the updated model. Therefore, it needs to be investigated into what is needed for PE data set, or if an imperfect model is OK if the data set used is representative for the future movements. In regular operation, milliAmpere will mostly use surge and not rotate much due to the hatch in both ends of milliAmpere. Results from Experiment 3 do not indicate that the adaptive model obtained during operation is significantly worse than the Master model, but this needs more investigation.

The lack of a PE data-set is scary because the model can easily be over-fitted. In a hypothetical situation moving directly against the current, the adaptive system, without current measurements, will learn that it has a constant bias force in surge. If it then changes direction and moves with the current, the learned bias will now be applied in the wrong direction, leading to undesirable behavior. The current impact could potentially be filtered

out by extending the data-set to contain both down- and upstream movements, but it is not a viable solution.

Introducing a Forgetting-factor

A different approach to the quickly changing dynamics, is to introduce a forgetting factor and might solve some of the issues introduced. A forgetting factor can be implemented by defining

$$\bar{\boldsymbol{\theta}}_P = \sum_{i=1}^{P-1} (\alpha_i \boldsymbol{\theta}_i) + \beta \boldsymbol{\theta}_P, \tag{5.1}$$

where $[\alpha_1, ..., \alpha_P - 1]$ and β are scalars that sum up to 1 and $\bar{\boldsymbol{\theta}}_P$ being the theta that is used in the DP system. In this way, some of the knowledge by earlier models can be kept, while still trying to quickly adapt to the new dynamics.

Another approach to compensate for passenger load for milliAmpere, is to reduce the adaptive model to a 1-DOF surge model and lock the model for sway and yaw. Since surge can be assumed decoupled from sway and yaw, extra data including all possible maneuvers would, in theory, not affect the obtained model in surge. The data set could therefore consist of some seconds of data while accelerating away from the quay and update the surge model thereafter.

Measuring the Passenger and Cargo Load

The optimal, and probably the best solution to the passenger and cargo load modeling is to measure the weight directly. Since the vessel is floating, the weight load and distribution can be estimated by observing the waterline of all four corners of the vessel. Cameras can be installed, and a deep neural network can be trained to estimate the waterline. If the weight is measured, a weight load model can be created and treated similarly to other measured disturbances. If this solution is robust, the adaptive system no longer needs to update the model to handle the variable weight correctly. The data sets could therefore span over longer time periods since all variables are measured.

Chapter 6

Conclusion and Further Work

This thesis covers the development and evaluation of a novel adaptive controller for autonomous vessels improving the vessel model, leading to increased performance and reduced energy consumption. A novel FF-based path-following steering law is also tested in combination with the adaptive model for high precision path-following.

Through MVA, an imprecise 3-DOF decoupled model is improved by formulating and fitting a lack-of-fit residual using PLS regression. The lack-of-fit residual is obtained by comparing the measured applied force to the estimated applied force using the model.

Experiments verify that the system works as intended. In the experiments, basis-functions from a 3-DOF decoupled model is sufficient to find a performance-increasing model, showing the proof-of-concept. Metric values, evaluated before and after the adaptive model update, implies performance improvements. Even in rough wind conditions, the system manages to find model improvements that also outperform the model currently existing for milliAmpere. This comparison is based on the MSE of the lack-of-fit residual. The improved performance is a result of a shift in the control action from FB to FF. The adaptive controller also supports wind and current modeling if measurements are obtained, leading to further improvements.

The current adaptive system is disturbed by unmodeled wave impact. The wave disturbances are too significant to find a proper model in these specific conditions. For normal operations, an assumption of no waves is not realistic. Therefore, a more complex model is needed to model the wave disturbance.

The development of this new approach to adaptive controllers for marine vessels opens many new possibilities. First, it is a quick and robust system for model identification, that works for all sorts of marine vessels, and can be performed without wind tunnels and small-scale models. Secondly, when using the adaptive controller in combination with the FF carrot-based control law, precision for path following can be increased to a new level. Thirdly, since the system is constantly active, the system can detect and adapt to changing

dynamics. The best-fitting model will quickly be found, leading to better performance and lower fuel costs. Fourthly, a more reliable and robust control system increases the safety and leads to a better experience for passengers onboard.

The adaptive controller still has room for improvement. The following topics could be further explored:

- Add measurements of the known disturbances wind, current, and weight load. Including measurements of the disturbances makes it possible to extend the model even further, leading to even better performance. Anemometers can measure the wind and current impact, and the weight load and distribution can be estimated by measuring the waterline in all four corners of the vessel.
- Strategies for when to suggest model updates. For the current adaptive system tested on milliAmpere, there will be a trade-off between too short and too long intervals between model updates. It is not desirable to make continuous updates because of too small data sets. It is not desirable to wait weeks before suggesting an update because dynamic changes like passenger loads would then not be compensated.
- Operation performance when training with normal operation data. A crucial component for the adaptive controller to work in everyday operations is that the data used to obtain the models are sufficient to increase the model performance. The calibration pattern used in the experiments is explicitly designed to ensure a PE data set. For normal operations of milliAmpere, the vessel confines itself to mostly surge movements. The question to be answered is whether the new models obtained to compensate for passenger load will increase the performance of crossings even if the models lack training data to understand movements in sway and yaw.
- Creating performance-improving models based on small data sets. If it proves to be difficult to obtain performance-improving models with small data sets, the following approaches could be evaluated:
  - Introducing forgetting factor to model updates. In this way, the controller can still mostly rely on earlier models while still adapting quickly to new conditions.
  - Reducing to a 1-DOF adaptive surge model. A simplified solution can be to assume surge decoupled from sway and yaw, so that a 1-DOF adaptive surge model can be updated based on limited data sets from crossings.
- Using basis-functions that are based on more advanced models. In this thesis, a simple 3-DOF model has been used as a proof of concept. Further work should also look into more complicated models that introduce other basis functions. A suggestion is to try the nonlinear model based on the low-aspect-ratio wing theory suggested by Ross et al. (2007). Wave models should also be looked further into. One possible approach interesting to look into is:
  - Using a 5-DOF model, including roll and pitch, to measure the size and direction of the wave. Only waves cause significant roll and pitch different to zero, which could make it possible to quantify characteristics of the direction

and size of the waves. A simplified model based on these variables could potentially describe some of the wave components of the lack-of-fit residual.

- A better navigational filter to estimate acceleration. A necessary condition for the MVA to work is to have accurate estimates for the vessel states. The solution presented in this thesis might not be the optimal solution, and a more detailed and complicated navigation filter might lead to better performance.

Bibliography

Alin, A., 2009. Comparison of PLS algorithms when number of objects is much larger than number of variables. Statistical papers 50, 711–720.

Aurlien, A., 2020. Multivariate Modeling and Adaptive Control of Autonomous Ferries. Specialization project report. Norwegian University of Science and Technology.

Beaufort, F., 1805. Beaufort wind scale. British Rear-Admiral .

Blanke, M., 1981. Ship propulsion losses related to automatic steering and prime mover control. Technical University of Denmark.

Blendermann, W., 1994. Parameter identification of wind loads on ships. Journal of Wind Engineering and Industrial Aerodynamics 51, 339–351.

Boerlage, M., Steinbuch, M., Lambrechts, P., van de Wal, M., 2003. Model-based feedforward for motion systems, in: Proceedings of 2003 IEEE Conference on Control Applications, 2003. CCA 2003., pp. 1158–1163 vol.2.

Brage, S., 2019. Development and Testing of Navigation and Motion Control Systems for milliAmpere. Master's thesis. Norwegian University of Science and Technology.

Brekke, E., 2019. Fundamentals of Sensor Fusion. NTNU.

Cairns, R., 2020. Norway pioneered electric ferries. Now it's making them self-driving. URL: `https://edition.cnn.com/travel/article/norway-self-driving-ferries-zeabuz-spc-intl/index.html`.

Chen, P.C., Chang, C.M., Spencer, B.F., Tsai, K.C., 2015. Adaptive model-based tracking control for real-time hybrid simulation. Bulletin of Earthquake Engineering 13, 1633–1653.

De Jong, S., 1993. SIMPLS: an alternative approach to partial least squares regression. Chemometrics and intelligent laboratory systems 18, 251–263.

Divino, R., 2020. An introduction to multivariate data analysis. URL: https://towardsdatascience.com/an-introduction-to-multivariate-data-analysis-ece93ceb1ed3.

DNVGL, 2021. Autonomous urban mobility: Taking digital assurance to the next level. URL: https://www.dnv.com/feature/autonomous-urban-mobility.html.

Esbensen, K.H., Guyot, D., Westad, F., Houmoller, L.P., 2002. Multivariate data analysis: in practice: an introduction to multivariate data analysis and experimental design. Multivariate Data Analysis.

Fairfield, N., 2016. On the road with self-driving car user number one. URL: https://medium.com/waymo/scenes-from-the-street-5bb77046d7ce#.tq11yyoqw.

Fossen, T.I., 2011. Handbook of marine craft hydrodynamics and motion control. John Wiley & Sons.

Gale, S., Rahmati, H., Gravdahl, J.T., Martens, H., 2017. Improvement of a Robotic Manipulator Model Based on Multivariate Residual Modeling. Frontiers in Robotics and AI 4, 28.

Hyatt, K., 2021. Elon Musk says Tesla's full self-driving tech will have level 5 autonomy by the end of 2021. URL: https://www.cnet.com/roadshow/news/elon-musk-full-self-driving-tesla-earnings-call/.

International, S., 2021. Taxonomy and Definitions for Terms Related to Driving Automation Systems for On-Road Motor Vehicles. URL: https://www.sae.org/standards/content/j3016_202104/.

Ioannou, P.A., Sun, J., 2012. Robust adaptive control. Courier Corporation.

Jervan, M., 2020. Improvement of an Autonomous Passenger Ferry Model Based on Multivariate Residual Modeling. Master's thesis. Norwegian University of Science and Technology.

Knutsen, M., 2020. Plans for an autonomous world first. URL: https://maritimecleantech.no/2020/06/02/plans-for-an-autonomous-world-first/.

Kongsberg, 2020. Crossing into new territory. URL: https://www.kongsberg.com/maritime/the-full-picture-magazine/2020/12/asko/.

Kongsberg Group, 2015. World's first professorship in Big Data Cybernetics. URL: https://www.kongsberg.com/newsandmedia/news-archive/2015/worlds-first-professorship-in-big-data-cybernetics.

Lambrechts, P., Boerlage, M., Steinbuch, M., 2004. Trajectory planning and feedforward design for high performance motion systems, in: Proceedings of the 2004 American Control Conference, pp. 4637–4642 vol.5.

Lee, I., 2019. NYC ferry announces system expansion with new routes & additional stops. URL: https://www.ferry.nyc/blog/nyc-ferry-service-to-expand-to-staten-island-coney-island-the-west-side-of-manhattan-and-the-east-bronx/.

Martens, H., 2020. Big Data Cybernetics. URL: http://folk.ntnu.no/martens/?BigDataCybernetics.

Molven, E.D., 2020. Optimal Control-based Docking for Autonomous Ferries. Master's thesis. Norwegian University of Science and Technology.

Pedersen, A.A., 2019. Optimization based system identification for the milliAmpere ferry. Master's thesis. Norwegian University of Science and Technology.

Quigley, M., Conley, K., Gerkey, B., Faust, J., Foote, T., Leibs, J., Wheeler, R., Ng, A.Y., et al., 2009. Ros: an open-source Robot Operating System, in: ICRA workshop on open source software, Kobe, Japan. p. 5.

Rasheed, A., San, O., Kvamsdal, T., 2019. Hybrid analysis and modeling as an enabler for big data cybernetics, in: Proceedings of the 32nd Nordic Seminar on Computational Mechanics, At Oulu, Finland, pp. 24–25.

Ross, A., Perez, T., Fossen, T.I., 2007. A novel manoeuvering model based on low-aspect-ratio lift theory and Lagrangian mechanics. IFAC Proceedings Volumes 40, 229–234. 7th IFAC Conference on Control Applications in Marine Systems, Lisbon, Portugal.

Russakovsky, O., Deng, J., Su, H., Krause, J., Satheesh, S., Ma, S., Huang, Z., Karpathy, A., Khosla, A., Bernstein, M., Berg, A.C., Fei-Fei, L., 2015. ImageNet Large Scale Visual Recognition Challenge. International Journal of Computer Vision (IJCV) 115, 211–252. doi:10.1007/s11263-015-0816-y.

Skjetne, R., Sørensen, M.E.N., Breivik, M., Værnø, S.A.T., Brodtkorb, A.H., Sørensen, A.J., Kjerstad, Ø.K., Calabrò, V., Vinje, B.O., 2017. AMOS DP Research Cruise 2016: Academic Full-Scale Testing of Experimental Dynamic Positioning Control Algorithms Onboard R/V Gunnerus. Proceedings of the ASME 2017 36th International Conference on Ocean, Offshore and Arctic Engineering Volume 1: Offshore Technology. URL: https://doi.org/10.1115/OMAE2017-62045, doi:10.1115/OMAE2017-62045.

Stensvold, T., 2017. Verdens første autonome skip i drift skal erstatte 40.000 vogntogturer i året. URL: https://www.tu.no/artikler/verdens-forste-autonome-skip-i-drift-skal-erstatte-40-000-vogntogturer-i-aret/382717.

Sørensen, M.E.N., Breivik, M., 2015. Comparing Nonlinear Adaptive Motion Controllers for Marine Surface Vessels. IFAC-PapersOnLine 48, 291–298. URL: https://www.sciencedirect.com/science/article/pii/S2405896315021862, doi:https://doi.org/10.1016/j.ifacol.2015.10.295. 10th IFAC Conference on Manoeuvring and Control of Marine Craft MCMC 2015, Copenhagen, Denmark.

Tekna, 2019. URL: https://www.tekna.no/fag-og-nettverk/IKT/ikt-bloggen/stordata-kybernetikk/.

Thyri, E.H., 2019. A Path-Velocity Decomposition Approach to Collision Avoidance for Autonomous Passenger Ferries. Master's thesis. Norwegian University of Science and Technology.

Torben, T.R., Brodtkorb, A.H., Sørensen, A.J., 2019. Control allocation for double-ended ferries with full-scale experimental results. IFAC-PapersOnLine 52, 45–50. URL: https://www.sciencedirect.com/science/article/pii/S2405896319321664, doi:https://doi.org/10.1016/j.ifacol.2019.12.281. 12th IFAC Conference on Control Applications in Marine Systems, Robotics, and Vehicles CAMS 2019, Daejeon, Republic of Korea.

Wilkes, W., 2021. Tesla's Autopilot Won't Achieve Full Autonomy, Waymo CEO Says. URL: https://www.bloomberg.com/news/articles/2021-01-22/tesla-s-autopilot-won-t-achieve-full-autonomy-waymo-ceo-says.

Williams, A., 2015. Autonomous Systems: Issues for Defence Policymakers.

Wold, S., Martens, H., Wold, H., 1983. The multivariate calibration problem in chemistry solved by the PLS method, in: Kågström, B., Ruhe, A. (Eds.), Matrix Pencils, Springer Berlin Heidelberg, Berlin, Heidelberg. pp. 286–293.

Yara, 2018. The first ever zero emission, autonomous ship. URL: https://www.yara.com/knowledge-grows/game-changer-for-the-environment/.

Yara, 2020. Yara Birkeland press kit — Yara International. URL: https://www.yara.com/news-and-media/press-kits/yara-birkeland-press-kit/.

Zanona, M., 2017. Driverless car investments top $80 billion. URL: https://thehill.com/policy/transportation/355696-driverless-car-investments-top-80-billion.

Zeabuz, 2021. miliAmepere. URL: https://zeabuz.com/miliampere/.

Appendices

Appendix A

Detailed SIMPLS Algorithm.

Algorithm 1: SIMPLS

Input: $n \times p$ matrix $\boldsymbol{X}$,
$n \times m$ matrix $\boldsymbol{Y}$,
number of factors A.

Output: $\boldsymbol{B}, \boldsymbol{h}$, **var**$\boldsymbol{X}$, **var**$\boldsymbol{Y}$

$\boldsymbol{Y}_0 = \boldsymbol{Y} - \text{MEAN}(\boldsymbol{Y})$ // center $\boldsymbol{Y}$

$\boldsymbol{S} = \boldsymbol{X}'^{*}\boldsymbol{Y}_0$ // cross-product

for $a = 1, \ldots, A$ **do** // For each dimention

  $\boldsymbol{q} =$ dominant eigenvector of $\boldsymbol{S}'^{*}\boldsymbol{S}$ // $\boldsymbol{Y}$ block factor weights

  $\boldsymbol{r} = \boldsymbol{S}^{*}\boldsymbol{q}$ // $\boldsymbol{X}$ block factor weights

  $\boldsymbol{t} = \boldsymbol{X}^{*}\boldsymbol{r}$ // $\boldsymbol{X}$ block factor scores

  $\boldsymbol{t} = \boldsymbol{t} - \text{MEAN}(\boldsymbol{t})$ // center scores

  $normt = \text{SQRT}\boldsymbol{t}'^{*}\boldsymbol{t}$ // compute norms

  $\boldsymbol{t} = \boldsymbol{t}/normt$ // normalize scores

  $\boldsymbol{r} = \boldsymbol{r}/normt$ // adapt weights accordingly

  $\boldsymbol{p} = \boldsymbol{X}'^{*}\boldsymbol{t}$ // $\boldsymbol{X}$ block factor loadings

  $\boldsymbol{q} = \boldsymbol{Y}_0'^{*}\boldsymbol{t}$ // $\boldsymbol{Y}$ block factor loadings

  $\boldsymbol{u} = \boldsymbol{Y}_0^{*}\boldsymbol{q}$ // $\boldsymbol{Y}$ block factor scores

  $\boldsymbol{v} = \boldsymbol{p}$ // initial orthogonal loadings

  if $a > 1$ **then**

    $\boldsymbol{v} = \boldsymbol{v} - \boldsymbol{V}^{*}(\boldsymbol{V}'^{*}\boldsymbol{p})$ // make $\boldsymbol{v} \perp$ previous loadings

    $\boldsymbol{u} = \boldsymbol{u} - \boldsymbol{T}^{*}(\boldsymbol{T}'^{*}\boldsymbol{u})$ // make $\boldsymbol{u} \perp$ previous $\boldsymbol{t}'$ values

  end if

  $\boldsymbol{v} = \boldsymbol{v}/\text{SQRT}(\boldsymbol{v}'^{*}\boldsymbol{v}$ // normalize orthogonal loadings

  $\boldsymbol{S} = \boldsymbol{S} - \boldsymbol{v}^{*}(\boldsymbol{v}'^{*}\boldsymbol{S})$ // deflate $\boldsymbol{S}$ with respect to current loadings

  Store $\boldsymbol{r}, \boldsymbol{t}, \boldsymbol{p}, \boldsymbol{q}, \boldsymbol{u}$, and $\boldsymbol{v}$ into $\boldsymbol{R}, \boldsymbol{T}, \boldsymbol{P}, \boldsymbol{Q}, \boldsymbol{U}$, and $\boldsymbol{V}$ respectively.

end for

$\boldsymbol{B} = \boldsymbol{R}^{*}\boldsymbol{Q}'$ // regression coefficients

$\boldsymbol{h} = \text{DIAG}(\boldsymbol{T}^{*}\boldsymbol{T}') + 1/n$ // leverages of objects

var$\boldsymbol{X}$ $\text{DIAG}(\boldsymbol{P}'^{*}\boldsymbol{P})/(n-1)$ // variance explained for $\boldsymbol{X}$ variables

var$\boldsymbol{Y}$ $\text{DIAG}(\boldsymbol{Q}'^{*}\boldsymbol{Q})/(n-1)$ // variance explained for $\boldsymbol{Y}$ variables

Appendix B

Carrot-based Steering Law

Algorithm 2: Carrot-based Steering Law

Input: $n \times 2$ matrix of waypoints $\boldsymbol{Q}$,
2×1 vector $\boldsymbol{\eta} = [x, y]^\top$,
switching-circle radius r

Output: 3×1 vector $\boldsymbol{\eta}_d = [x_d, y_d, \psi_d]^\top$

$lad = 2r$ // look-ahead distance
$\boldsymbol{q}_{prev} = \boldsymbol{Q}_{0,:}$ // previous waypoint
$\boldsymbol{q}_{curr} = \boldsymbol{Q}_{1,:}$ // current waypoint
if *NORM*$(\boldsymbol{q}_{curr} - \boldsymbol{\eta}) \leq r$ **then** // inside switching circle
  ROLL($\boldsymbol{Q}$, axis= 0) // circular shift all rows 1 step up
  $\boldsymbol{q}_{prev} = \boldsymbol{Q}_{0,:}$ // previous waypoint
  $\boldsymbol{q}_{curr} = \boldsymbol{Q}_{1,:}$ // current waypoint
end if
$[x_k, y_k]^\top = \boldsymbol{q}_{prev}$ // coordinates of previos waypoint
$[x_{k+1}, y_{k+1}]^\top = \boldsymbol{q}_{curr}$ // coordinates of current waypoint
$\alpha_k = \text{arctan2}(y_{k+1} - y_k,\ x_{k+1} - x_k)$ // path angle
$atd = (x - x_k)\cos(\alpha_k) + (y - y_k)\sin(\alpha_k)$ // along track distance
$\boldsymbol{R} = \boldsymbol{R}_{ned}^{path}(\alpha_k)$ // rotation matrix from path to NED
if $atd >$*NORM*$(\boldsymbol{q}_{curr} - \boldsymbol{q}_{prev})$ **then** // error handling: re-aim
  $[x_d, y_d]^\top = \boldsymbol{q}_{curr}$ // desired pos
else if $atd > 0$ **then** // phase 1: approaching waypoint
  $[x_d, y_d]^\top = \boldsymbol{q}_{prev} + R[atd + lad, 0])$ // desired pos
else // phase 2: deaccelearate and turn
  $[x_d, y_d]^\top = \boldsymbol{q}_{prev} + R[r, 0])$
end if
$\psi_d = \alpha_k$

Appendix C

Procedures for Experiments with milliAmpere

C.1 Safety

When using milliAmpere it is important that safety and HMS-guidelines are followed. Operating an experimental vessel with unverified software can cause undesired situations to occur. It is also important that procedures are followed making it easy for the next group to complete their experiments. The following procedures and guidelines should be followed carefully:

C.1.1 Before Testing

- The crew must be of at least two persons.
- All crew members must be trained in procedures and risk analysis.
- All crew members must use a life-jacket when leaving the quay.
- Battery status must be checked.
- Emergency buttons must be tested.
- The weather must be suitable and the crew must be aware of other activity in the harbour.

C.1.2 During Testing

- The harbour activity must constantly be observed.
- The controller and emergency buttons must always be in reach.

- For the maneuvering, margins of error are added, and responsibly handled.

C.1.3 After Testing

- The vessel is safely moored ashore.
- The monitor, keyboard and life-jackets are placed in the boxes and locked.
- Both main power switches is switched off.
- The milliAmpere is connected to shore power.
- The controller and emergency system is charged and brought back to ”murhuset”.

C.2 Test Goal

Goals for Experiment 1:

- Testing the system performance with improved tuning of the reference filter.
- Testing the system performance with improved adaptive tuning.
- Testing the system performance in strong winds.

Goals for Experiment 2:

- Analysing how the adaptive control system performs compared to the current control system on milliAmpere.
- Analysing how robust the system is in regards to wave disturbances in addition to wind.

C.3 Handling of Test Data

ROS-bags are used to store all the complete log for all topics. ROS-bags can be replayed and re-simulate the system at a later time. To skip the re-simulation data from performance and data sets are stored and saved as a pickle file containing a dictionary of numpy arrays. A complete procedure is the following:

- Start the recording of a ROS-bags containing all topics.
- Store the generated picle files on the computer after each finished calibration round.
- Use a timer for 12 minutes to keep track the calibration cycles.

C.3.1 Organization and Storage

ROS-bags are automatically named witht the following convention:
MA_YYYY-MM-DD-HH-MM-SS.BAG.

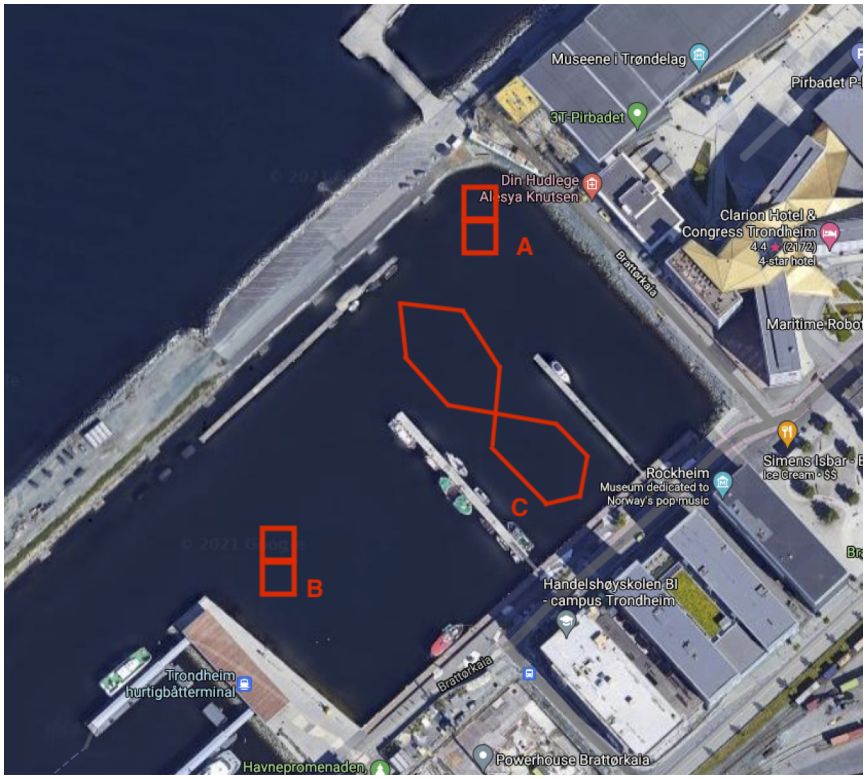

Figure C.1: Location of the experiments from Experiment 1 (A), Experiment 2 (B), and Experiment 3 (C).

- Note the time when a test is started and the time when the rosback started recording.
- Note that the time is according to the GMT time.

C.4 Location

The tests are conducted in the Brattøra harbour in Thondheim. The locations of Experiments 1, 2, and 3 are shown in Figure C.1.

C.5 Experiments 1 and 2: Calibration Procedures

Experiments 1 and 2 run the same test. The following procedure is followed for each experiment.

1. Manually maneuver milliAmpere close to the desired starting point.

2. Activate the DP system in the bridge and set the desired waypoint.
3. Update the starting position in the waypoint scheduler.
4. When milliAmpere has stabilized, boot the adaptive model node, the data-collector node, and the waypoint scheduler.
5. Now, pay attention to the surroundings while the test is beeing conducted.
6. Store the auto-saved data in a fitting folder for every completed round.
7. When the number of desired calibration rounds have been completed, stop the adaptive model node, data collector node, and the waypoint scheduler node.

C.6 Experiment 3: Path Following Procedures

The following procedure is followed for Experiment 3.

1. Manually maneuver through the desired path. Note the desired waypoints.
2. Activate the DP system.
3. Insert the desired waypoints into the path-following script.
4. Manually maneuver milliAmpere close to the desired starting point.
5. Activate the DP system and set the starting position.
6. When milliAmpere has stabilized, boot the path-following node.
7. Now, pay attention to the surroundings.
8. Store the auto-saved data in a fitting folder.
9. When the number of desired cycles has been completed, stop the path-following node and take active control of milliAmpere.

Appendix D

IFAC CAMS Paper Contribution

Multivariate Modeling and Adaptive Control of Autonomous Ferries

Andreas Aurlien* **Bjørn-Olav H. Eriksen*** **Morten Breivik***

** Center for Autonomous Marine Operations and Systems, Department of Engineering Cybernetics, Norwegian University of Science and Technology, N0-7491 Trondheim, Norway*
E-mail: andreas@aurlien.net, bjorn-olav.holtung.eriksen@ntnu.no, morten.breivik@ieee.org

Abstract: This paper deals with the design and evaluation of a multivariate-based adaptive controller for marine surface vessels. The goal is to make a system that periodically updates the vessel model, used by a dynamic positioning (DP) controller, in order to improve the motion-control performance. The model is generated by analyzing speed and acceleration data using multivariate analysis (MVA) to fit a 3-degrees of freedom (DOF) surface vessel model. Experimental results show that the adaptive control system works as intended and manages to make significant improvements in all performance metrics, compared to the initial system. The results also show that the system is robust even with the impact of wind and wind gusts of at least 6 m/s.

Keywords: Autonomous ferries, Big data cybernetics, Adaptive control, Multivariate analysis, Model-based control.

1. INTRODUCTION

Autopilots for ships have existed for a long time, but only in the past few years fully autonomous vehicles has started to become a reality. We see automated public transportation such as trams and busses, and Tesla is close to make their cars fully autonomous. Investments of 80 billion US dollars occurred between August 2014 and June 2017 for automation of the car industry (Zanona, 2017). The shipping industry is also gaining speed in the process of automating the industry. Kongsberg Maritime's and Yara's autonomous ship MS Yara Birkeland is soon ready for sea tests (Yara, 2020). This ship is the first of its kind and is expected to replace 40 000 truckloads yearly, between Yara's fertilizer factory and the shipping harbors (Stensvold, 2017).

The growth of infrastructure in the cities has sparked the idea to further utilize the seaways for transportation (Cairns, 2020; Knutsen, 2020). This often unused space can be used by environmentally friendly passenger ferries as an additional mobility option or even as a replacement for some of the transportation on land. Through Norwegian University of Science and Technology (NTNU)'s Autoferry project, we have designed the research vessel milliAmpère, showed if Fig. 1, which is used to develop algorithms needed for fully autonomous ferries. The Autoferry team designs and creates systems such as collision avoidance systems, docking systems, thruster allocation, interactive design, and regulations.
Recently, we launched the second version of milliAmpère. Its design supports the transportation of 12 passengers across the canal in the city center of Trondheim (Stensvold, 2016). NTNU's research on autonomous ferries has also lead to the spin-off company Zeabuz, that plans to design and launch their first system in 2022 (Zeabuz, 2021).

When controlling autonomous ferries, an accurate and efficient system is needed for docking and other high-accuracy operations. Model-based control is a good way to achieve high accuracy for such systems. A perfect model is, however, impossible to obtain. Assumptions and approximations are made to get a simplified model of the vessel system. In most cases, this results in a good enough model for control purposes. However, an imperfect model will result in sub-optimal control actions. This can result in energy inefficient and imprecise maneuvers. Many systems overlook the value of sensor data that can be used to obtain a better model.

Big data cybernetics (BDC) is a new and upcoming field in cybernetics (Martens, 2020). NTNU, Kongsberg and Equinor have established the world's first professorship in BDC (Group, 2015). The CEO of Kongsberg, Walter Qvam, says that the need to utilize smart data will only grow bigger as new methods for production, operation, and industrial solutions are taken into use (Group, 2015). We are on the verge of an industrial revolution in regards to the value of data, and NTNU and Kongsberg want to contribute to world-leading research in the field of BDC (Group, 2015). In BDC, multivariate analysis (MVA) forms the basis for modeling unmodeled dynamics by analyzing sensor data. Analyzing the data collected from the sensors gives an estimate of the model error. The concept is that MVA finds a correlation in the data that best describes the model error. With this kind of analysis, an adaptive control system for updating the model is obtained, which can reduce the inconsistency observed in

Fig. 1. The milliAmpère 1 ferry right after the launching.

the gathered data. This method for generating an adaptive control system is the core focus of this paper.

In this paper, Jervan (2020) started the design of an adaptive controller for milliAmpère that used available sensor data to improve the model and Aurlien (2020) continued the work to finalize the controller and test the system full scale. We have used Gale et al. (2017)'s improvement of a robotic manipulator model as the basis of our work. The motivation for this paper is to share the design of an adaptive control system and how it performs compared to a non-adaptive control system.

Section 2 introduces the surface vessel model and Section 3 shows how we can use such a model to obtain precise and efficient motion control. The core part of the adaptive control system that builds on MVA gets introduced in in Section 4. Section 5 describes the experimental setup and shows the improvements in performance due to the adaptive control system. Finally, in Section 6, we sum up the paper and presents the conclusion.

2. SURFACE VESSEL MODEL

The motion of a surface vessel is with the Society of Naval Architects and Marine Engineers (SNAME) notation represented by the pose vector $\boldsymbol{\eta} = [x, y, \psi]^\top \in \mathbb{R}^2 \times \mathbb{S}$ and the velocity vector $\boldsymbol{\nu} = [u, v, r] \in \mathbb{R}^3$. Here (x, y) is the Cartesian position and ψ is the yaw angle, both given in a local north-east-down (NED) frame. Furthermore, (u, v) are the linear velocities given in the body-fixed frame, and r is the yaw rate.

Fossen (2011) models the 3 degrees of freedom (DOF) dynamics of a surface vessel as:

$$\dot{\boldsymbol{\nu}} = \boldsymbol{R}(\psi)\,\boldsymbol{\nu} \tag{1}$$

$$\boldsymbol{M}^*\dot{\boldsymbol{\nu}} + \boldsymbol{C}^*(\boldsymbol{\nu})\boldsymbol{\nu} + \boldsymbol{D}^*(\boldsymbol{\nu})\boldsymbol{\nu} = \boldsymbol{\tau}^* + \boldsymbol{R}^\top(\psi)\boldsymbol{w}^*, \tag{2}$$

where

$$\boldsymbol{R}(\psi) = \begin{bmatrix} cos(\psi) & -sin(\psi) & 0 \\ sin(\psi) & cos(\psi) & 0 \\ 0 & 0 & 1 \end{bmatrix} \tag{3}$$

is a rotation matrix $\boldsymbol{R} \in SO(3)$, and where $\boldsymbol{M}^*$, $\boldsymbol{C}^*$, $\boldsymbol{D}^*$, and $\boldsymbol{\tau}^*$ are the real inertia matrix, Coriolis and centripetal matrix, damping matrix, and control input vector respectively. The vector $\boldsymbol{w}^*$ models the real disturbances which includes environmental forces such as wind and current.

In the model, the system matrices are assumed to satisfy the properties $\boldsymbol{M}^* = \boldsymbol{M}^{*\top} > 0$, $\boldsymbol{C}^*(\boldsymbol{\nu}) = -\boldsymbol{C}^*(\boldsymbol{\nu})^\top$, and $\boldsymbol{D}^*(\boldsymbol{\nu}) > 0$. The considered model will, however, never be perfect. We model the uncertainties related to the error between the real and considered model as

$$\boldsymbol{M}^* = \frac{1}{\delta}\boldsymbol{M} \tag{4}$$

$$\boldsymbol{C}^*(\boldsymbol{\nu}) = \frac{1}{\delta}\boldsymbol{C}(\boldsymbol{\nu}) \tag{5}$$

$$\boldsymbol{D}^*(\boldsymbol{\nu}) = \frac{1}{\sigma}\boldsymbol{D}(\boldsymbol{\nu}) \tag{6}$$

$$\boldsymbol{\tau} = \rho\boldsymbol{\tau}, \tag{7}$$

where $\delta \in \mathbb{R}^+$ express the uncertainty associated with the inertia and Coriolis matrix, $\sigma \in \mathbb{R}^+$ express the uncertainty associated with the damping matrix, and $\rho \in \mathbb{R}^+$ is the uncertainty associated with the control input vector. The goal of the adaptive controller is to minimize this model error.

3. MOTION CONTROL

Motion control for autonomous ferries describes how to achieve the desired movement. Fig. 2 shows a flow chart of how a motion control system can be designed. The guidance law provides way-points that when combined maps out a path for the vessel to follow. A third-order reference filter then uses the way-points to calculate a feasible transition between the way-points by providing desired values for position, velocity, and acceleration. The dynamic positioning (DP) system then uses the desired values and measurements to maintain the desired trajectory. The control signal from the DP system is processed by a thruster allocation system that finds a feasible way for the thrusters of the vessel to make the desired control action.

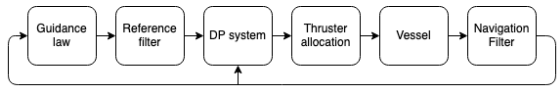

Fig. 2. Flow chart for achievement of motion control.

3.1 Dynamic Positioning

A DP system's task is to maintain a ships position and heading. Such a system can be implemented as a PID controller and a feed-forward (FF) controller. The PID controller is defined as

$$\boldsymbol{\tau}_{PID} = -\boldsymbol{R}^\top(\psi)\boldsymbol{K}_p(\boldsymbol{\eta} - \boldsymbol{\eta}_d) - \boldsymbol{K}_d(\boldsymbol{\nu} - \boldsymbol{\nu}_d) - \boldsymbol{R}^\top(\psi)\boldsymbol{K_i}\int_0^t (\boldsymbol{\eta} - \boldsymbol{\eta}_d)dt, \tag{8}$$

where $\boldsymbol{K}_p, \boldsymbol{K}_i, \boldsymbol{K}_d \in \mathbb{R}^{3\times3}$ are design gain matrices with $\boldsymbol{K}_p, \boldsymbol{K}_i, \boldsymbol{K}_d \geq 0$ and $\boldsymbol{\nu}_d \in \mathbb{R}^3$ is the desired velocity vector. To improve the performance, we also use a FF controller that is defined as

$$\boldsymbol{\tau}_{FF} = \boldsymbol{F}(\dot{\boldsymbol{\nu}}_d, \boldsymbol{\nu}_d), \tag{9}$$

where

$$\boldsymbol{F}(\dot{\boldsymbol{\nu}}, \boldsymbol{\nu}) = \boldsymbol{M}\dot{\boldsymbol{\nu}} + \boldsymbol{C}(\boldsymbol{\nu})\boldsymbol{\nu} + \boldsymbol{D}(\boldsymbol{\nu})\boldsymbol{\nu} - \boldsymbol{R}^\top(\psi)\boldsymbol{w} \tag{10}$$

is the surface vessel model.

4. MULTIVARIATE ANALYSIS

By analysing the vessel state measurements an improved vessel model can be obtained by checking for model inconsistency. Partial least squares (PLS) regression can be used to find underlying structures between two data sets. For the data sets $\boldsymbol{X} \in \mathbb{R}^{N\times K}$ and $\boldsymbol{Y} \in \mathbb{R}^{N\times k}$, the goal is to predict $\boldsymbol{Y}$ with a linear combination of $\boldsymbol{X}$ according to

$$\hat{\boldsymbol{Y}} = [\boldsymbol{1}, \boldsymbol{X}]\boldsymbol{\beta}, \tag{11}$$

where $\boldsymbol{1} \in \mathbb{R}^{N\times 1}$ is a vector, $\boldsymbol{\beta} \in \mathbb{R}^{K+1\times k}$ is a matrix where k is the number of output dimensions, K is the number of input dimensions, and N is the number of samples. In the analysis the correlation between $\boldsymbol{X}$ and $\boldsymbol{Y}$ is maximized so that the residual $\boldsymbol{E}$ in

$$\boldsymbol{Y} = [\boldsymbol{1}, \boldsymbol{X}]\boldsymbol{\beta} + \boldsymbol{E}, \tag{12}$$

is minimized. This means that white noise will not affect the analysis, since there are no correlation in white noise. The simple partial least squares (SIMPLS) algorithm can be used to solve the PLS regression problem.

Storing and analysing the error between model predicted and real motion can lead to an improved vessel model. The lack-of-fit residual is a measure of the unmodeled forces acting on a surface vessel. It is defined as

$$\boldsymbol{\tau}_\epsilon \triangleq \boldsymbol{\tau} - \hat{\boldsymbol{\tau}}, \tag{13}$$

where

$$\hat{\boldsymbol{\tau}} = \boldsymbol{F}(\dot{\boldsymbol{\nu}}_{mes}, \boldsymbol{\nu}_{mes}) \tag{14}$$

is the estimated applied force, $\dot{\boldsymbol{\nu}}_{mes}, \boldsymbol{\nu}_{mes} \in \mathbb{R}^3$ is the measured vessel acceleration and speed, respectively.

With MVA the lack-of-fit residual is modeled as

$$\boldsymbol{\tau}_\epsilon \approx \boldsymbol{\theta}^\top \boldsymbol{\phi}, \tag{15}$$

where $\boldsymbol{\phi}(t) \in \mathbb{R}^{b\times 1}$ contains the selected basis functions, $\boldsymbol{\theta} \in \mathbb{R}^{b\times 3}$ is the scores of the selected basis functions, and b is the number of basis functions. To clarify, this is the model for the lack-of-fit residual, so when comparing to (11) that has gathered samples over a period of time, we have $\boldsymbol{\phi} \in \mathbb{R}^{(K+1)\times N} = [\boldsymbol{1}, \boldsymbol{X}]^\top$ and $\boldsymbol{\theta} = \boldsymbol{\beta}^\top$.

Better estimates of the parameters describing the model of Fossen (2011) can be made by adding each term in the model as a basis function in the MVA. The basis functions that describe the 3 DOF model of Fossen (2011) without disturbances is

$$\boldsymbol{\phi}_1 = [\dot{u}, \dot{v}, \dot{r}, uv, ur, vr, rr, u, v, r, sgn(u)u^2, sgn(v)v^2, sgn(r)r^2, u^3, v^3, r^3, |u|u, |v|v, |r|r|v|r, |r|v]^\top. \tag{16}$$

The remaining components in the lack of fit residual such as current and wind impact should be modeled by other basis functions. According to Blendermann (1994), the wind will apply a force to a 3 DOF ship model in the following manner:

$$\boldsymbol{\tau}_{wind} = \frac{1}{2}\rho_a V_{rw}^2 \begin{bmatrix} C_X(\gamma_{rw})A_{F_w} \\ C_Y(\gamma_{rw})A_{L_w} \\ C_N(\gamma_{rw})A_{L_w}L_{0a} \end{bmatrix}, \tag{17}$$

where ρ_a is the air density, $V_{rw} \in \mathbb{R}$ is the relative air speed, γ_{rw} is the angle of attack of V_{rw} relative to the bow of the ship, $C_X(\gamma_{rw}), C_Y(\gamma_{rw})$, and $C_N(\gamma_{rw})$ are the wind coefficients for horizontal plane motion, L_{0a} is the overall length, and where A_{F_w} and A_{L_w} is the frontal and lateral projected areas, respectively. The basis functions

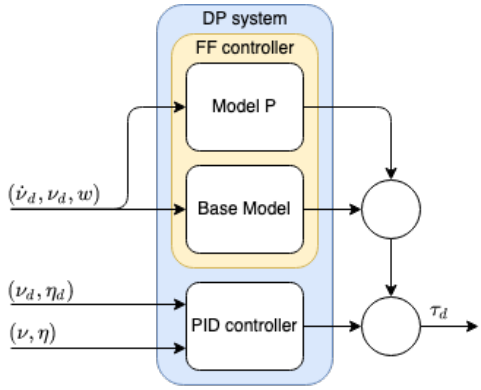

Fig. 3. A block diagram of the DP system.

$$\boldsymbol{\phi}_2 = [V_{rw}^2 cos(\gamma_{rw}), V_{rw}^2 sin(\gamma_{rw}), V_{rw}^2 sin(\gamma_{rw})\gamma_{rw}]^\top, \tag{18}$$

are a good linear approximation to the Blendermann wind model. If wind is measured the basis functions are added to the MVA. In simulations done by Aurlien (2020), $\boldsymbol{\phi}_2$ detects most of the wind contribution in the lack-of-fit residual. Similarly, we can use the basis functions

$$\boldsymbol{\phi}_3 = [V_{rc}^2 cos(\gamma_{rc}), V_{rc}^2 sin(\gamma_{rc}), V_{rc}^2 sin(\gamma_{rc})\gamma_{rc}]^\top, \tag{19}$$

where $V_{rc} \in \mathbb{R}$ is the relative current, γ_{rc} is the angle of attack of V_{rc} relative to the bow of the ship, to model the current if we add current measuremetns. The basis functions take inspiration from the Blendermann (1994) model. With these basis functions we assume uniform flow around the ship. This assumption is justified for relative small ships. All basis functions are gathered according to

$$\boldsymbol{\phi} = [\boldsymbol{\phi}_1^\top, \boldsymbol{\phi}_2^\top, \boldsymbol{\phi}_3^\top]^\top. \tag{20}$$

The advantage of describing the lack of fit residual as done in (13) is that an improved vessel model can be described as

$$\boldsymbol{F}_P(\dot{\boldsymbol{\nu}}, \boldsymbol{\nu}, \boldsymbol{\phi}) = \boldsymbol{M}\dot{\boldsymbol{\nu}} + \boldsymbol{C}\boldsymbol{\nu} + \boldsymbol{D}\boldsymbol{\nu} + \boldsymbol{\theta}_P^\top \boldsymbol{\phi}, \tag{21}$$

where P denotes the P^{th} model update. The FF control signal from (9) is now updated to

$$\boldsymbol{\tau}_{FF} = \boldsymbol{F}_P(\dot{\boldsymbol{\nu}}_d, \boldsymbol{\nu}_d, \boldsymbol{\phi}_d), \tag{22}$$

where $\boldsymbol{\phi}_d(\dot{\boldsymbol{\nu}}_d, \boldsymbol{\nu}_d, V_{rw}, \gamma_{rw}, V_{rc}, \gamma_{rc}) = [\boldsymbol{\phi}_{1_d}^\top, \boldsymbol{\phi}_2^\top, \boldsymbol{\phi}_3^\top]^\top$.

A slower model update loop is introduced by redefining the base model as

$$\boldsymbol{F}(\dot{\boldsymbol{\nu}}, \boldsymbol{\nu}, \boldsymbol{\phi}) = \frac{1}{S}\sum_{P=1}^{S} \boldsymbol{F}_P(\dot{\boldsymbol{\nu}}, \boldsymbol{\nu}, \boldsymbol{\phi}) \tag{23}$$

where S is a predefined constant for number of models to average. The slow model update will ensure that the system always is booted with a good dynamics model. Fig. 3 shows how the improved model is used as a part in the DP system. The block diagram in Fig. 4 shows how the improved model is generated by providing the lack-of-fit residual and the basis functions for the MVA. In Fig. 4, $\boldsymbol{w}_{mes} \in \mathbb{R}^{2\times 1}$ and $\boldsymbol{\alpha}_{mes} \in \mathbb{R}^{2\times 1}$ are the measured thuster rpm and angle respectively.

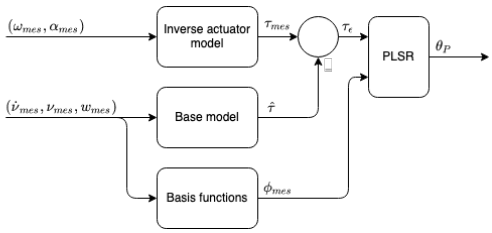

Fig. 4. A block diagram showing the generation of the improved model.

5. EXPERIMENTAL RESULTS AND PERFORMANCE EVALUATION

5.1 Experimental setup

Experiments are designed for the research vessel milliAmpère to verify the adaptive controller. The vessel has a length of 5 m, a beam of 2.8 m and weighs 1670 kg. Two azimuth thrusters, delivering 2 kW each, control the movement of the ferry. The hull of milliAmpère is symmetrical both around the x, and the y axis and is flat underneath. There lack of a keel makes milliAmpère turn quickly, but makes it quite unstable in yaw. When assuming symmetry along the x-axis the inertia matrix is given as

$$\begin{aligned}\boldsymbol{M}^* &\triangleq \boldsymbol{M}_{RB} + \boldsymbol{M}_A \\ &= \begin{bmatrix} m_{11} & 0 & 0 \\ 0 & m_{22} & m_{23} \\ 0 & m_{32} & m_{33} \end{bmatrix}\end{aligned}$$

The Coriolis and centripetal matrix is given as

$$\begin{aligned}\boldsymbol{C}^*(\boldsymbol{\nu}) &\triangleq \boldsymbol{C}_{RB}(\boldsymbol{\nu}) + \boldsymbol{C}_A(\boldsymbol{\nu}) \\ &= \begin{bmatrix} 0 & 0 & c_{13}(\boldsymbol{\nu}) \\ 0 & 0 & c_{23}(\boldsymbol{\nu}) \\ -c_{13}(\boldsymbol{\nu}) & -c_{23}(\boldsymbol{\nu}) & 0 \end{bmatrix}\end{aligned}$$

where $c_{13}(\boldsymbol{\nu}) = Y_{\dot{v}} v + \frac{1}{2}(N_{\dot{v}} + Y_{\dot{r}})$ and $c_{23}(\boldsymbol{\nu}) = -X_{\dot{u}} u$. Finally, the damping matrix is given as

$$\begin{aligned}\boldsymbol{D}^*(\boldsymbol{\nu}) &\triangleq \boldsymbol{D}_L + \boldsymbol{D}_{NL}(\boldsymbol{\nu}) \\ &= \begin{bmatrix} -d_{11}(\boldsymbol{\nu}) & 0 & 0 \\ 0 & -d_{22}(\boldsymbol{\nu}) & -d_{23}(\boldsymbol{\nu}) \\ 0 & -d_{32}(\boldsymbol{\nu}) & -d_{33}(\boldsymbol{\nu}), \end{bmatrix}\end{aligned}$$

where $d_{11}(\boldsymbol{\nu}) = X_u + X_{|u|u}|u| + X_{uuu}u^2$, $d_{22}(\boldsymbol{\nu}) = Y_v + Y_{|v|v}|v| + Y_{|r|v}|r|, d_{23}(\boldsymbol{\nu}) = Y_r + Y_{|v|r}|v| + Y_{|r|r}|r| + Y_{vvv}v^2$, $d_{32}(\boldsymbol{\nu}) = N_v + N_{|v|v}|v| + N_{|r|v}|r|$ and $d_{33}(\boldsymbol{\nu}) = N_r + N_{|v|r}|v| + N_{|r|r}|r| + N_{rrr}r^2$. The parameter values for $\boldsymbol{M}, \boldsymbol{C}(\boldsymbol{\nu})$, and $\boldsymbol{D}(\boldsymbol{\nu})$ for milliAmpère are listed in Table 1.

To compare the performance of the adaptive controller relative to a controller using an imperfect model we use a 12 corner motion test. This path is used to ensure that the adaptive controller has persistent excitation (PE).

We use a reference filter to generate the trajectory for the DP system to follow. The reference filter is given by

$$\boldsymbol{\eta}_d^{(3)} + (2\boldsymbol{\Delta} + I)\boldsymbol{\Omega}\ddot{\eta}_d + (2\boldsymbol{\Delta} + I)\boldsymbol{\Omega}^2 + \boldsymbol{\Omega}^3\boldsymbol{\eta}_d = \boldsymbol{\Omega}^3\boldsymbol{r}, \quad (24)$$

where $\boldsymbol{\Omega}, \boldsymbol{\Delta} \in \mathbb{R}^{3\times3}$ are positive definite design matrices, that determine the dynamics of the filter and $\boldsymbol{r}$ is the reference setpoint. The output of the filter is the reference signals $\boldsymbol{\eta}_d, \dot{\boldsymbol{\eta}}_d$, and $\ddot{\boldsymbol{\eta}}_d$. The reference filter receives waypoints with a frequency of 60 seconds. We use the pose from all corners of the calibration path showed in Fig. 5 as waypoints. The DP system then uses the desired values for position, velocity, and acceleration, to follow the trajectory generated by the reference filter.

Table 1. Estimated parameters for the model for milliAmpère (Pedersen, 2019).

Parameter	Value	Parameter	Value
m_{11}	2389.657	$Y_{\|v\|v}$	-116.486
m_{12}	0	Y_{vvv}	-24.313
m_{13}	0	$Y_{\|r\|v}$	-1540.383
m_{21}	0	Y_r	24.732
m_{22}	2533.911	$Y_{\|v\|r}$	572.141
m_{23}	62.386	$Y_{\|r\|r}$	-115.457
m_{31}	0	N_v	3.524
m_{32}	28.141	$N_{\|v\|v}$	-0.832
m_{33}	5068.910	$N_{\|r\|v}$	336.827
X_u	-27.632	N_r	-122.860
$X_{\|u\|u}$	-110.064	$N_{\|r\|r}$	-874.428
X_{uuu}	-13.965	N_{rrr}	0.000
Y_v	-52.947	$N_{\|v\|r}$	-121.957

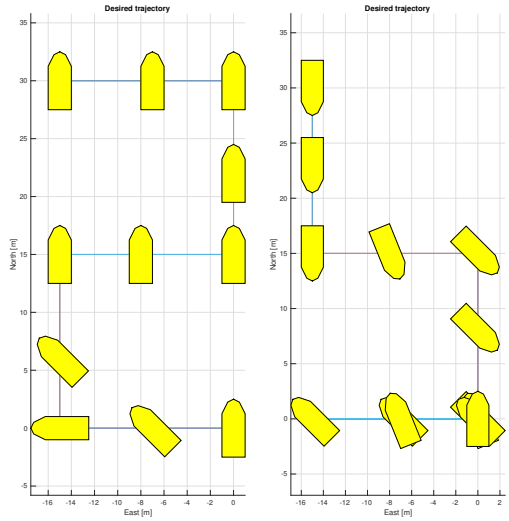

(a) Part one. (b) Part two.

Fig. 5. The calibration path used to exitate the adaptive controller.

For the experiments, we used the base model of milliAmpère with $\delta = 0.4$ as the initial model. By doing this we ensured that the adaptive system could find a new and better model, in case the current model is quite good. In the MVA, we use 12 principal components when performing the SIMPLS algorithm. The wind was quite strong the day the test was performed with winds of 6 m/s and up to 10 m/s in the gusts, according to the weather forecast. It is worth mentioning that the vessel was, to some degree, sheltered from the wind by the milo in the harbor. The adaptive system suggests a new model once

the calibration trajectory is completed, and automatically starts a new round. This means that the model used in round 3 is based on data collected in rounds 1 and 2.

5.2 Estimation of acceleration

In order to do the MVA, we need acceleration data for surge, sway, and yaw. Since the acceleration data is only used as a part of a training set, we do not need to do the estimation on-line. Since the PLS regression is unaffected by white noise, we can also allow the acceleration estimate to contain white noise. Taking advantage of these relaxing requirements, we use the numerically derivative of smoothed velocity data to estimate the acceleration. Smoothing is a filtering process where we use data not only from the past but also from the future. The convolution

$$\boldsymbol{\nu}_{smoothed}(t) = \boldsymbol{\nu}(t) * \boldsymbol{g}(t) = \int_{-\infty}^{\infty} \boldsymbol{\nu}(\xi)\boldsymbol{g}(t-\xi)d\xi, \quad (25)$$

where $\boldsymbol{g}$ is a square window, describes the smoothing process. In the experiments we use a window of ± 1.0 seconds for both surge, sway, and yaw, where all component of $\boldsymbol{\nu}$ inside the window, is weighted the same. The integral of the window is 1, which in reality makes this an averaging process. We need the smoothing step because the velocity data is no longer white, due to the previous filtration in a navigation filter.

5.3 Performance metrics

To compare motion controllers for autonomous ferries Sørensen and Breivik (2015) suggest the following metrics: The integral of the square of the error (ISE) that is defined as

$$ISE = \int_0^t e^2 dt, \quad (26)$$

and penalizes large errors more than small errors, the integral of the absolute error (IAE) that is defined as

$$IAE = \int_0^t |e| dt, \quad (27)$$

and penalizes errors linearly, and the integral of the absolute error multiplied by the energy consumption (IAEW) that is defined as

$$IAEW = \int_0^t |e(t)| dt \int_0^t P(t) dt, \quad (28)$$

and scales the precision with the power usage. Additionally we use the integral of the energy consumption (IEC), defined as

$$IEC = \int_0^t P(t) dt. \quad (29)$$

5.4 Experimental results

Fig. 6 shows how the adaptive model improves the performance every round. The results show that the use of the adaptive model in the FF increases the precision and reduces the energy usage. To quantify the results, we find that the IAE, ISE, IAEW, and IEC from round 1 to round 3 are improved by 46%, 75%, 57%, and 20% respectively.

Fig. 7 shows how the model reconstructs the estimated actuator force $\boldsymbol{\tau}_{mes}$, based on velocity and acceleration

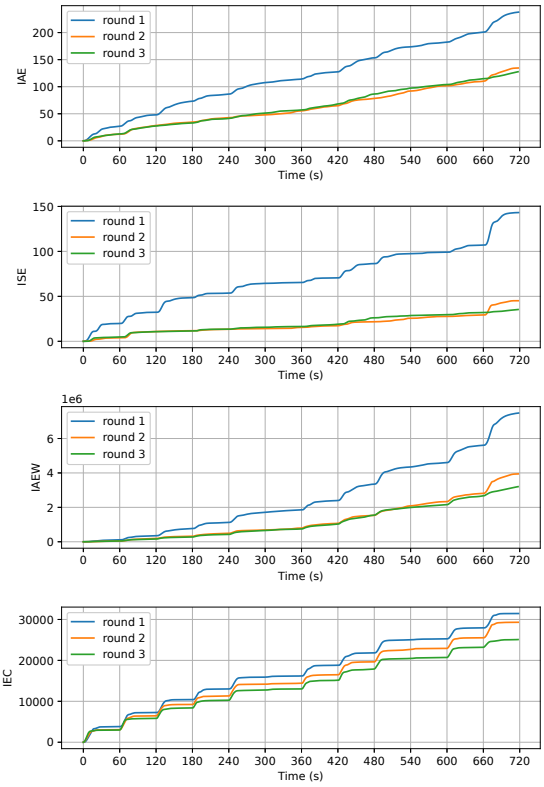

Fig. 6. Performance of the adaptive system in experiments. The model is updated every round based on the data from previous rounds.

data. Here, $\hat{\boldsymbol{\tau}}$ is estimated using the current base model of milliAmpère with $\delta = 1$, while $\hat{\boldsymbol{\tau}}_{new}$ is estimated with the adaptive model found after completing round 2. We use the mean squared error (MSE) to compare the model fit which shows that the model error gets improved by 84%, 87%, and 68% for surge, sway, and yaw respectively.

Considering the experimental results, we see that the adaptive system manages to adaptively find a better model of the hydrodynamics. However, there are still deviations between the measured and estimated force applied. The most likely explanation for this is that wind gusts have pushed the vessel off its trajectory so that when the vessel applies a counterforce the vessel stays relatively still. In Fig. 7 we see that all deviations fit a natural compensating force to wind disturbances from the NW direction, which was the actual wind direction. At $t = 405$ to $t = 420$ the vessels heading is $\psi = 180$ and tries to keep its pose. Once the wind gust comes from the NW direction, we observe that the models detect the force and that the thrusters try to cancel out the wind impact by applying a force in negative surge and positive sway, which with the current heading is a force in the NE direction. The models then detect the net force that takes the vessel back to its desired pose.

Currents can also be a component of deviations between

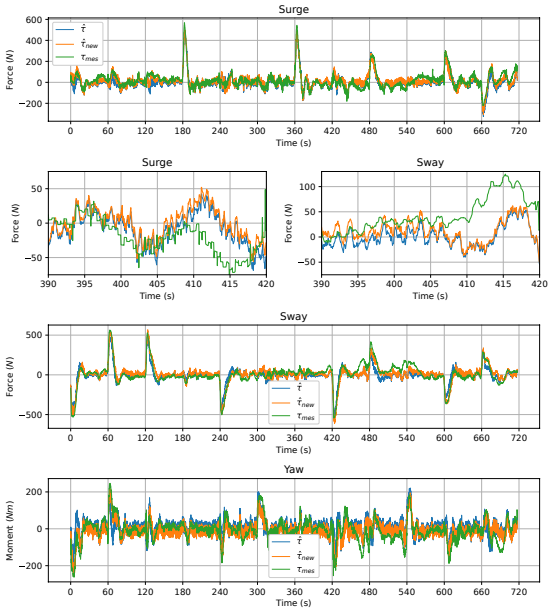

Fig. 7. Model fit for base model and improved model.

the measured and expected force. When currents are present, the ground movement and the relative water movement will no longer be the same.
Since the adaptive system lacks wind and current measurements, we can not expect the model to understand these components. It is therefore a good sign that we observe that the adaptive system does not over-fit the lack-of-fit residual and at the same time finds an improved model of what the system can model.

6. CONCLUSION

We have presented the design of an adaptive control system using position and acceleration data to fit a 3-DOF vessel model with MVA. Experimental results show that the adaptive system manages to increase the motion control precision and lowering the energy usage when the system is initiated with an imprecise model. The adaptive system also proves to be robust against wind impact. The adaptive model obtained in the experiments out-performs the current model of milliAmpère found by Pedersen (2019). Additionally, we have designed the adaptive control system so that is flexible for further model improvements by adding measurements from wind and current.

For further work, we need to test how the adaptive system works under normal operation. A concern is that normal operations will not fully exitate the adaptive system and therefore suggest imprecise or even wrong model improvements that could lead to worse performance.
We also need research on when it is strategic to update the model. On the one extreme, you want to have as much data as possible before making a model suggestion, while on the other hand, updating the model often will account for disturbances such as passenger load. Another factor that needs to be considered is that if too small data sets are used to detect passenger load, we could potentially over-fit static disturbances. A worst-case scenario would be if the data set only contain surge movement with $\gamma_{rc} = 0\ rad$. The model generated would then not be able to filter out the current impact in the MVA.

ACKNOWLEDGEMENTS

This work was supported by the NTNU Digital transformation project Autoferry and the Research Council of Norway through the Centres of Excellence funding scheme, project no. 223254.

REFERENCES

Aurlien, A. (2020). Multivariate modeling and adaptive control of autonomous ferries. Project report, Norwegian University of Science and Technology.

Blendermann, W. (1994). Parameter identification of wind loads on ships. *Journal of Wind Engineering and Industrial Aerodynamics*, 51(3), 339–351.

Cairns, R. (2020). Norway pioneered electric ferries. Now it's making them self-driving. URL `https://edition.cnn.com/travel/article/norway-self-driving-ferries-zeabuz-spc-intl/index.html`.

Fossen, T.I. (2011). *Handbook of marine craft hydrodynamics and motion control*. John Wiley & Sons.

Gale, S., Rahmati, H., Gravdahl, J.T., and Martens, H. (2017). Improvement of a robotic manipulator model based on multivariate residual modeling. *Frontiers in Robotics and AI*, 4, 28.

Group, K. (2015). World's first professorship in big data cybernetics. URL `https://www.kongsberg.com/newsandmedia/news-archive/2015/worlds-first-professorship-in-big-data-cybernetics`.

Jervan, M. (2020). *Improvement of an Autonomous Passenger Ferry Model Based on Multivariate Residual Modeling*. Master's thesis, Norwegian University of Science and Technology.

Knutsen, M. (2020). Plans for an autonomous world first. URL `https://maritimecleantech.no/2020/06/02/plans-for-an-autonomous-world-first/`.

Martens, H. (2020). Big data cybernetics. URL `http://folk.ntnu.no/martens/?BigDataCybernetics`.

Pedersen, A.A. (2019). *Optimization based system identification for the milliAmpere ferry*. Master's thesis, Norwegian University of Science and Technology.

Sørensen, M.E.N. and Breivik, M. (2015). Comparing nonlinear adaptive motion controllers for marine surface vessels. *IFAC-PapersOnLine*, 48(16), 291–298.

Stensvold, T. (2016). Verdens første førerløse passasjerferge kan gå over en kanal i Trondheim. URL `https://www.tu.no/artikler/verdens-forste-forerlose-passasjerferge-kan-ga-over-en-kanal-i-trondheim/363790`.

Stensvold, T. (2017). Verdens første autonome skip i drift skal erstatte 40.000 vogntogturer i året. URL `https://www.tu.no/artikler/verdens-forste-autonome-skip-i-drift-skal-erstatte-40-000-vogntogturer-i-aret/382717`.

Yara (2020). Yara Birkeland press kit — Yara International. URL `https://www.yara.com/news-and-media/press-kits/yara-birkeland-press-kit/`.

Zanona, M. (2017). Driverless car investments top $80 billion. URL `https://thehill.com/policy/transportation/355696-driverless-car-investments-top-80-billion`.

Zeabuz (2021). miliamepere. URL `https://zeabuz.com/miliampere/`.

Andreas Aurlien

Multivariate Modeling and Adaptive Control of Autonomous Ferries

NTNU
Kunnskap for en bedre verden